Electrical Resistivity Tomography in Environmental Amelioration

by

Guye Stephenson Strobel

A THESIS
SUBMITTED TO THE FACULTY OF GRADUATE STUDIES
IN PARTIAL FULFILLMENT OF THE REQUIREMENTS
FOR THE DEGREE OF
DOCTOR OF PHILOSOPHY

Department of Electrical and Computer Engineering
University of Manitoba
Winnipeg, Manitoba
September 1996

ISBN 0-612-16316-4

Canada

Name _____

Dissertation Abstracts International and *Masters Abstracts International* are arranged by broad, general subject categories. Please select the one subject which most nearly describes the content of your dissertation or thesis. Enter the corresponding four-digit code in the spaces provided.

Engineering
SUBJECT TERM

0544
SUBJECT CODE

UMI

Subject Categories

THE HUMANITIES AND SOCIAL SCIENCES

COMMUNICATIONS AND THE ARTS
Architecture 0729
Art History 0377
Cinema 0900
Dance 0378
Fine Arts 0357
Information Science 0723
Journalism 0391
Library Science 0399
Mass Communications 0708
Music 0413
Speech Communication 0459
Theater 0465

EDUCATION
General 0515
Administration 0514
Adult and Continuing 0516
Agricultural 0517
Art 0273
Bilingual and Multicultural 0282
Business 0688
Community College 0275
Curriculum and Instruction 0727
Early Childhood 0518
Elementary 0524
Finance 0277
Guidance and Counseling 0519
Health 0680
Higher 0745
History of 0520
Home Economics 0278
Industrial 0521
Language and Literature 0279
Mathematics 0280
Music 0522
Philosophy of 0998
Physical 0523
Psychology 0525
Reading 0535
Religious 0527
Sciences 0714
Secondary 0533
Social Sciences 0534
Sociology of 0340
Special 0529
Teacher Training 0530
Technology 0710
Tests and Measurements 0288
Vocational 0747

LANGUAGE, LITERATURE AND LINGUISTICS
Language
- General 0679
- Ancient 0289
- Linguistics 0290
- Modern 0291

Literature
- General 0401
- Classical 0294
- Comparative 0295
- Medieval 0297
- Modern 0298
- African 0316
- American 0591
- Asian 0305
- Canadian (English) 0352
- Canadian (French) 0355
- English 0593
- Germanic 0311
- Latin American 0312
- Middle Eastern 0315
- Romance 0313
- Slavic and East European 0314

PHILOSOPHY, RELIGION AND THEOLOGY
Philosophy 0422
Religion
- General 0318
- Biblical Studies 0321
- Clergy 0319
- History of 0320
- Philosophy of 0322

Theology 0469

SOCIAL SCIENCES
American Studies 0323
Anthropology
- Archaeology 0324
- Cultural 0326
- Physical 0327

Business Administration
- General 0310
- Accounting 0272
- Banking 0770
- Management 0454
- Marketing 0338

Canadian Studies 0385
Economics
- General 0501
- Agricultural 0503
- Commerce-Business 0505
- Finance 0508
- History 0509
- Labor 0510
- Theory 0511

Folklore 0358
Geography 0366
Gerontology 0351
History
- General 0578
- Ancient 0579
- Medieval 0581
- Modern 0582
- Black 0328
- African 0331
- Asia, Australia and Oceania 0332
- Canadian 0334
- European 0335
- Latin American 0336
- Middle Eastern 0333
- United States 0337

History of Science 0585
Law 0398
Political Science
- General 0615
- International Law and Relations 0616
- Public Administration 0617

Recreation 0814
Social Work 0452
Sociology
- General 0626
- Criminology and Penology ... 0627
- Demography 0938
- Ethnic and Racial Studies 0631
- Individual and Family Studies 0628
- Industrial and Labor Relations 0629
- Public and Social Welfare 0630
- Social Structure and Development 0700
- Theory and Methods 0344

Transportation 0709
Urban and Regional Planning 0999
Women's Studies 0453

THE SCIENCES AND ENGINEERING

BIOLOGICAL SCIENCES
Agriculture
- General 0473
- Agronomy 0285
- Animal Culture and Nutrition 0475
- Animal Pathology 0476
- Food Science and Technology 0359
- Forestry and Wildlife 0478
- Plant Culture 0479
- Plant Pathology 0480
- Plant Physiology 0817
- Range Management 0777
- Wood Technology 0746

Biology
- General 0306
- Anatomy 0287
- Biostatistics 0308
- Botany 0309
- Cell 0379
- Ecology 0329
- Entomology 0353
- Genetics 0369
- Limnology 0793
- Microbiology 0410
- Molecular 0307
- Neuroscience 0317
- Oceanography 0416
- Physiology 0433
- Radiation 0821
- Veterinary Science 0778
- Zoology 0472

Biophysics
- General 0786
- Medical 0760

EARTH SCIENCES
Biogeochemistry 0425
Geochemistry 0996
Geodesy 0370
Geology 0372
Geophysics 0373
Hydrology 0388
Mineralogy 0411
Paleobotany 0345
Paleoecology 0426
Paleontology 0418
Paleozoology 0985
Palynology 0427
Physical Geography 0368
Physical Oceanography 0415

HEALTH AND ENVIRONMENTAL SCIENCES
Environmental Sciences 0768
Health Sciences
- General 0566
- Audiology 0300
- Chemotherapy 0992
- Dentistry 0567
- Education 0350
- Hospital Management 0769
- Human Development 0758
- Immunology 0982
- Medicine and Surgery 0564
- Mental Health 0347
- Nursing 0569
- Nutrition 0570
- Obstetrics and Gynecology .. 0380
- Occupational Health and Therapy 0354
- Ophthalmology 0381
- Pathology 0571
- Pharmacology 0419
- Pharmacy 0572
- Physical Therapy 0382
- Public Health 0573
- Radiology 0574
- Recreation 0575
- Speech Pathology 0460
- Toxicology 0383

Home Economics 0386

PHYSICAL SCIENCES
Pure Sciences
Chemistry
- General 0485
- Agricultural 0749
- Analytical 0486
- Biochemistry 0487
- Inorganic 0488
- Nuclear 0738
- Organic 0490
- Pharmaceutical 0491
- Physical 0494
- Polymer 0495
- Radiation 0754

Mathematics 0405
Physics
- General 0605
- Acoustics 0986
- Astronomy and Astrophysics 0606
- Atmospheric Science 0608
- Atomic 0748
- Electronics and Electricity 0607
- Elementary Particles and High Energy 0798
- Fluid and Plasma 0759
- Molecular 0609
- Nuclear 0610
- Optics 0752
- Radiation 0756
- Solid State 0611

Statistics 0463

Applied Sciences
Applied Mechanics 0346
Computer Science 0984
Engineering
- General 0537
- Aerospace 0538
- Agricultural 0539
- Automotive 0540
- Biomedical 0541
- Chemical 0542
- Civil 0543
- Electronics and Electrical 0544
- Heat and Thermodynamics 0348
- Hydraulic 0545
- Industrial 0546
- Marine 0547
- Materials Science 0794
- Mechanical 0548
- Metallurgy 0743
- Mining 0551
- Nuclear 0552
- Packaging 0549
- Petroleum 0765
- Sanitary and Municipal 0554
- System Science 0790

Geotechnology 0428
Operations Research 0796
Plastics Technology 0795
Textile Technology 0994

PSYCHOLOGY
General 0621
Behavioral 0384
Clinical 0622
Developmental 0620
Experimental 0623
Industrial 0624
Personality 0625
Physiological 0989
Psychobiology 0349
Psychometrics 0632
Social 0451

THE UNIVERSITY OF MANITOBA

FACULTY OF GRADUATE STUDIES

COPYRIGHT PERMISSION

ELECTRICAL RESISTIVITY TOMOGRAPHY IN ENVIRONMENTAL AMELIORATION

BY

GUYE STEPHENSON STROBEL

A Thesis/Practicum submitted to the Faculty of Graduate Studies of the University of Manitoba in partial fulfillment of the requirements for the degree of

DOCTOR OF PHILOSOPHY

to the memory of jean and archie stewart
theresa and joe strobel
this dissertation is dedicated in admiration

significant life challenges, nobly met
in due course, may my time have been
a glimmering reflection of such achievement

and to karen, stephenson, and kieran strobel
this thesis is dedicated with humility

the challenge, always before us

non sine palma pulveris

Abstract

This is a dissertation on electrical resistivity tomography methods for ameliorating environmental systems; particularly, historic radioactive waste disposal facilities. It supports the thesis that the remote sensing features of these methods are of high value in such applications because sensors can be conveniently placed and need not significantly modify the subject under study. In contrast, invasive methods frequently damage confinement barriers and increase the likelihood of contamination—often chemical and radioactive in nature. Further, intruding instruments affect material properties, thereby distorting natural responses and complicating their study and evaluation. This research showed these methods respond to contrasts in resistivity between waste and host materials, varying resistivity within waste, and differences in moisture levels.

The data of this research was processed with the algorithm of Wexler, a double-constraint, iterative approach to solving the nonlinear electrical resistivity tomography problem. To overcome the slow rate of convergence of this algorithm, a general multistep approach was developed where the response of the model variables are fitted individually by iteration number using an equation suited to the process. The result is used to compute the limit as the iteration number goes to infinity. This led to improved updates, and fewer iterations to converge by as much as two orders of magnitude.

Surveys were performed with data-acquisition electronics and software, and processing software, developed as part of this study. Groundwater in a clay-packed borehole was monitored *in situ* at the Underground Research Laboratory for quantitative results that were verified using independent measurements. Admittance was imaged in the rock wall of the borehole where it showed an anomaly corresponding to a parallel borehole.

A field study focused on imaging in three dimensions with measurements made only from surface. Images of metal barrels buried in sand with different orientations were successfully produced, and a survey conducted at a conventional landfill facility discerned trench boundaries and individual targets. A survey, performed at an operational low-level facility, discovered trenches and individual targets.

In summary, this dissertation research applied electrical resistivity tomography methods for characterizing and ameliorating environmental systems. The data inversion algorithm was improved and a complete and comprehensive system was developed—encompassing data-acquisition and data-processing. The system was extensively applied in laboratory and field surveys and supported the thesis that the remote sensing features of these methods are of high value when ameliorating environmental systems.

Acknowledgements

The number of individuals providing aid and support with scholarly and material contributions is too large to detail. Technically skilled people in AECL made significant and appreciated contributions—helped build and use systems and gave advice on scientific investigation and documentation. Supervisors made funds available and supported course work and research effort over the years.

Some of the research was jointly funded by AECL and Ontario Hydro under the auspices of the CANDU [1] Owners Group. This was done as part of the Canadian Nuclear Fuel Waste Management Program.

I would like to thank the members of my thesis committee: Professor Al Wexler; Dr Nash Soonawala; Mr Monte Raber; and Professor Richard Gordon who provided technical expertise, superior judgement, and insight that made the pursuit of this degree an advanced exercise in self-development and self-discipline. And Professor Doug LaBrecque, for serving as the external examiner of this work.

To my family, thank you, for all the support and your own personal sacrifices.

[1] CANDU (CANadian Deuterium Uranium) reactor fuel is a registered trademark of AECL Research.

Contents

List of Figures

List of Tables

Chapter 1

Introduction

1.1 Historical Background

Much progress has been made in the study of electrical resistivity tomography (ERT) methods for geophysical applications since the seminal paper of Dey and Morrison, 1979 [24]. The work that followed, particularly that of Dines and Lytle, [26] helped to establish a program in ERT methods at Lawrence Livermore National Laboratory (LLNL). This is a national laboratory, active in the American nuclear research program. Technical developments progressed throughout the 1980s during which the problems of inverting ERT data constantly challenged the research. This is still the main obstacle to the emergence of the method as a widely accepted method.

It was recent political and not technological breakthroughs that led to greater interest in this and similar technologies. With the breakup of the Soviet Union late in the 1980's, the Cold War between the United States and the Soviet Union no longer threatened to heat up. As a result, the huge nuclear arms production industries of these two major world powers lost their reason for existence—coming face-to-face with the prospect of elimination. The economic consequences sparked action, particularly in the many regions supported by related industries. Cold War resources were redirected into cleaning up massive environmental problems generated by over half-a-century of arms production. This was justified on the argument that past practices in radioactive waste disposal were no longer considered responsible in today's political climate. This interest in the ERT methods is still gathering

momentum as it becomes more widely appreciated; to illustrate, it is to be used as a major element in tests at the United States Department of Energy's Yucca Mountain Project [85].

While activity in ERT methods was ongoing on in the United States, field work was being performed in Canada. At the University of Manitoba, funding by the Canadian Department of Defense supported work applying the ERT method in detecting unexploded ordnance in Canadian artillery ranges and the method was also applied at a Manitoba landfill to characterize subterranean pollution plumes. The research for this dissertation began early in 1990, to meet the need of Atomic Energy of Canada Limited for measuring moisture in a soil-material barrier as part of tests for the Canadian Nuclear Fuel Waste Management Program (NFWMP). The ERT method appeared to answer this need and part of the research work reported here is on development and successful application of the method in this program. Atomic Energy of Canada Limited also manages Canada's low-level waste and this provided another application in this dissertation research.

This dissertation research is at an apex. The remediation needs of the Canadian and American nuclear industry have converged with developments made by earth scientists who have been working in ERT methods for more then a decade. In this study, the performance of the inversion algorithm for ERT data has been improved and a role in the remediation of contaminated systems has been established. Major effort has been made in developing two separate data-acquisition systems, two distinct implementations of the data inversion algorithm, and two distinct applications of the ERT method.

1.2 Purpose and Novel Contributions of this Research

This dissertation research advances the ERT method for remediation of low-level radioactive and nuclear fuel waste disposal facilities. The advances encompass all aspects of the technology and include data acquisition and data processing—software and hardware. They were applied in the laboratory and in the field in two and three dimensions. These applications were surface surveys to: 1) characterize low-level radioactive waste disposal facilities and

Table 1.1: Purpose of dissertation research.

·Study and improve data processing in two and three dimensions using synthetic data. The approach developed can be applied to any iterative inversion of nonlinear systems.
·Design and build a data-acquisition system suitable for environmental applications.
·Apply the data acquisition and data processing to monitor moisture in a soil-type barrier (buffer) developed for the Canadian concept for the disposal of nuclear fuel waste.
·Apply the data acquisition and data processing system for surface measurements to characterize low-level radioactive waste management facilities.

2) study moisture movement in an engineered barrier system (buffer) within the Canadian concept for the disposal of nuclear fuel waste [1-3, 22, 23]. The result was verified using independent measurements. The moisture analysis was quantitative.

One of the primary purposes of the work was to accelerate the rate of convergence of the data processing for image inversion. This was achieved with data generated from synthetic models and from real measurements. The resulting approach proved to have general application to finding roots in any nonlinear system when applying an iterative method. Table 1.1 summarizes the objectives of this study.

This dissertation makes the following novel contributions to the use of ERT methods:

- Chapter 3: The work of others was expanded to accelerate convergence and included a peak-detection filter [39, 65]. This work illustrated the lack of stability and slow convergence properties of the algorithm used for data processing in this study.

- Chapter 4: A novel multistep method was developed for accelerating iterative processing to convergence. The approach, applicable to iterative processing in general, improved the unmodified algorithm by two orders of magnitude when inverting field

data.

- Chapter 5: A ERT methods data acquisition system suitable for use in environmental applications was developed and applied in a full-scale test in a soil material (buffer) at the Underground Research Laboratory as part of Canada's Nuclear Fuel Waste Management Program. The study produced a qualitative analysis for the moisture distributions in the buffer. This aspect of the research: 1) examined the electrical properties of buffer; 2) modelled the electrical response; and 3) derived the calibration relationship between the moisture and conductance.

- Chapter 6: The ERT method was applied in a field survey of a low-level radioactive waste management area to locate trench boundaries and individual targets.

- Chapter 7: Conclusions were drawn from the result of this dissertation research. Other applications for ERT methods are discussed. For example, the preliminary result of Section7.3 demonstrated the method for monitoring moisture in granite.

- Appendix A: The mathematical basis for the inversion of ERT data was developed, expanding on previous work.

- Appendix B: A mathematical approach as developed for fitting non-coincidental stochastic data using a general form for a calibration curve. The approach was used for *in situ* calibration of ERT data with independent moisture measurements. This is a general approach with broader applicability.

In addition, Chapter 2 gives background on the data inversion algorithm used for this dissertation.

1.3 The Technological Basis

The ERT methods image the distribution of admittance within a body using current and voltage measurements. Poisson's equation is solved for the potential field to fit the data:

$$-\nabla \cdot \kappa \nabla \phi = f \tag{1.1}$$

where $\kappa \equiv$ conductivity, $\phi \equiv$ electrical potential, and $f \equiv$ impressed current source distribution. The resultant system of equations is solvable with a variational approach since solutions of Dirichlet's variational problems satisfy Poisson's equation [7]. As prescribed by the divergence theorem, Equation 1.1 with boundary conditions uniquely determines the field throughout the body.

When applying the ERT method, measurements are made at various points in and around the target while exciting it using an externally applied electric field. Points of current application and voltage measurements are referred to as ports, and multiple excitations are applied along projection angles [108]. Figure 1.1 is a schematic of the application of ERT methods.

The ERT methods are computational intensive, multi-dimensional applications of traditional four-probe arrays by which conductivity distributions are recovered [96]. The result at every point is dependent on the measurements at all electrodes: in contrast with classical resistivity measurements where data sets are independent and assumptions require that the target region be laterally homogeneous [97]. As well, ERT methods give greater definition and so smaller targets are more readily imaged [96].

The size of the ERT inversion problem depends on the number of electrodes used and the number of degrees of freedom in the model. There are three variables to consider: 1) the size of the survey; 2) the specified detail in the images; and 3) the number of measurements taken. Each electrode can serve as the anode or the cathode of the current loop, or as an electrode for a voltage reading. In a single measurement sequence, two electrodes form the current loop while the voltage is measured at the remaining electrodes.

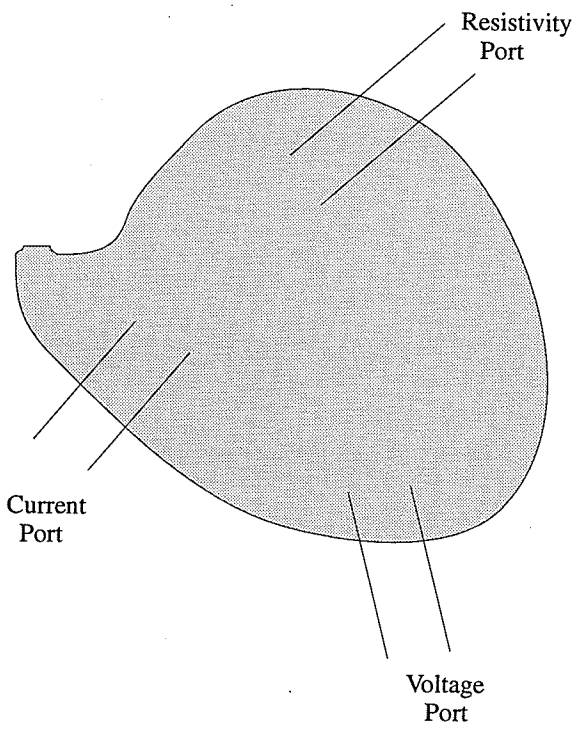

Figure 1.1: Electrical resistivity tomography measurements. Voltage measurements are made in and around the object while exciting with an external field. Different excitation sites are used for different sets of measurements.

In a set of single measurement sequences intended to produce one image, electrodes serve in any combination of these roles. In theory, the number of sequences allows sufficient measurements to achieve a desired resolution in the final image: it was advancements in computers that made reasonable resolutions practical.

1.4 Established Environmental Applications

The ERT method can be used to characterize environmental systems. This is useful in determining physical parameters in a system intended as a disposal facility for nuclear fuel waste [79, 95] and for conventional waste sites [96]. The following is a list of five such applications with a general statement on the commercial viability of the ERT method as the sixth item:

- **Imaging Plumes in a Landfill:** The method has been successfully applied in a surface survey in three dimensions at a sanitary landfill located in a flood plain alluvium [96]. The image extended 36m down from surface over a 84m × 84m grid. Laboratory studies were conducted as part of the effort to compare characteristics of ERT methods with conventional resistivity methods. The higher quality favoured the ERT method mainly because it does not average over length at depth in proportion to the electrode separation (as discussed above).

- **Hydrological Properties of Tuff:** Laboratory work using the ERT method has characterized the hydrological properties of volcanic tuff on a scale of centimetres. It provided a qualitative measure of the permeability from direct measurements, and it included a scanning electron microscopy study of specimen in thin section. The objective was to study the properties of tuff for restricting water movement through a nuclear fuel waste vault design. The samples were repeatedly dehydrated and saturated under pressure. The result showed that the hydration phase was not the reverse of the drying phase. This was attributed to several phenomenon including fracture healing due to high temperature deposition of silica during hydration [16, 59].

- **Grout Penetration in Fractures:** The ERT method has been applied to measure grout penetration in rock fractures in a study conducted at the Underground Research Laboratory (URL), near Lac du Bonnet, Manitoba [76]. To determine the performance of grout in sealing the natural fractures in a nuclear fuel waste vault system, grout was monitored in two dimensions as it displaced the ground water. Changes in electromagnetic attenuation rate were detected and mapped to position the grout within the fracture zone [71].

- **Sparging:** The ERT method was used in support of sparging activities by monitoring the progress of an injected air/steam front [70, 72, 101]. Sparging strips contaminants such as volatile organic compounds from saturated and unsaturated soil

horizons. The application was successful even near metal-cased wells [72]. The study reported in [101] compare high-frequency tomography, in the megahertz range, with the low-frequency ERT method. The report proposed the ERT method be used for hydrocarbon prospecting.

- **Cross-hole Tomography:** Field tests have been conducted in two dimensions to study the performance of reconstruction algorithms with cross-borehole electrical resistivity tomography [17]. Monitoring was done while water was introduced in the soil of a hydraulically complex region to infer the size and shape of the water plume [19]. It was able to match the result to the geology of the test region obtained from borehole tests.

- **Commercial Prospects of ERT Methods:** There are commercial prospects for the ERT method in environmental applications. The version of the technology developed at Lawrence Livermore Laboratories, is being transferred to a private sector company RIMTech.[1,2] Tests by RIMTech were proposed for site remediation work in the United States during 1995 (W.D. Daily, personal communication) and it is now a part of a regular research and development program. The ERT method is being applied for monitoring leaks around single shelled storage tanks. Out of 149 such tanks, between 60 and 70 are leaking. Tests were originally performed in two dimensions and later in three dimensions with good results (A. Rameriz, personal communication). The ERT method is superior to two other options considered—tank level monitoring and point sensor measurements in the surrounding soil. The presence of "bergs" in the chemical "soup" make tank level monitoring ineffective and the highly heterogeneous material causes channeling of the waste flow, causing it to be missed by point sensors.

[1] Denver CO.

[2] The author understands the technology has been transferred elsewhere for business reasons.

Table 1.2 summarizes some of the environmental characterization studies of ERT methods in the past.

1.5 Prospective Environmental Applications

The ERT method is a typical geophysical method, often faced with practical problems of large scale and poor target access. The contamination due to the nuclear industry has generated a demand for geophysical methods in remediation. There are many such prospective applications such as for characterization and in support of amelioration activities such as soil stripping and sparging. Because of its remote sensing features, the ERT method is well matched to the challenges presented in this field.

The ERT method is also under consideration as a new medical procedure because of it's non-invasive nature and because it is not necessary to use a potentially damaging source of energy such as is done in X-ray tomography [10, 11, 61]. Although promising, this application is outside the scope of this study and not considered further in this dissertation other then in passing remarks.

1.5.1 Radioactive Waste Management

There is considerable interest in characterizing radioactive waste sites due to society's increased concern for the environment [101]. This interest has led to considerable effort to characterize and remediate historic sites in the United States and Canada.

Cold War nuclear arms production of the past half-century has been the largest source for the accumulation of radioactive and chemical waste. Within the United States, the inventory has been constantly growing from the output of metallurgical industries such as those established in Hanford, Washington. Amounts in excess of 190 000m^3 of solid waste and 760×10^9l of liquid and toxic chemicals waste have been stored, dumped, or poured into the ground or into retaining systems at Handford. This has been ongoing from 1944 until production of plutonium ceased in 1986. A major source of the problems at Handford are

nine plutonium-producing reactors and nine reprocessing facilities containing 430 000 tonnes of radioactive waste consisting mainly of contaminated reactor components. The cost of the cleanup at Hanford is estimated at up to $200b, even though standards for acceptability have not been fully developed [35]. Although Hanford is the most significant site since it comprises over 60% of the most highly radioactive waste, there are thirteen other major waste sites in the United States.

The chemistry of the pollutants has not been characterized because much of the waste was mixed at random. Contaminants include plutonium, uranium, and radon in mill tailings, uranium and thorium ores, and various transuranic elements. At many of these sites, waste has leaked from disposal facilities and contaminates up to 25% of the local ground water. The soil conditions at the various sites range from desert [35] to fully water saturated soils [99] with manmade structures often present.

The strategy for cleanup and treatment of contaminated sites must consider the media under treatment, the contaminants present, and the future use of the site. The cleanup objectives range from isolating the site to prevent unsafe radiological doses to humans to returning the site to unrestricted use. Approaches under consideration include cleanup or removal of contamination by plowing, scraping, hosing, grinding, sieving, flushing, vacuuming, and scrubbing, or stabilization of the contamination through vegetation, windrows, covering, lining, grouting or chemical immobilization [6], thermal destruction, air stripping of ground water, and soil vapor extraction [32]. The cleanup activities themselves will greatly increase the emissions and have an impact on workers and surrounding communities—impacts that have only begun to be studied [32].

Important remediation activities in the United States have been categorized in a National Priority List (NPL) focusing on those sites posing a health risk even when left undisturbed [32]. This list is divided into four major projects; the Nevada (weapons) Test Site (NTS), the Uranium Mill Tailings Remedial Action Project (UMTRAP), the Formally Utilized Sites Remedial Action Project (FUSRAP), and the Surplus Facilities Management

Program (SFMP). Table 1.3 is a summary of those programs in radioactive waste management in the United States and an expanded discussion follows:

- **The Nevada (weapons) Test Site (NTS):** The NTS involves the Nevada site and proposes to remediate the pollutants generated from releases of radioactivity during weapons testing. Contaminants were usually airborne and distribution resulted as a function of surface characteristics and meteorological parameters. Decontamination by removal of surface soils has been tried but the process destroys local vegetation needed to stabilize the top soil to control further dispersion of contaminants. Oil can be applied as an interim measure while new vegetation establishes itself.

- **The Uranium Mill Tailings Remedial Action Project (UMTRAP):** The UMTRAP Program was established in 1978 to remediate twenty-four inactive uranium processing sites. These are sites contaminated with tailings containing radionuclides, toxic elements, and chemicals. The contaminants have been left as slurry material in open ponds that have evolved into raised piles. Strategies under consideration would stabilize the waste in place, stabilize it in a more favourable on-site location, or remove it entirely. Stabilization can be accomplished with covers of earth, rock, asphalt, vegetation, or combinations thereof. Wind screens minimize the destructive effect of wind erosion on covers and conditioning chemicals immobilize the contaminated material.

- **The Formally Utilized Sites Remedial Action Project (FUSRAP):** The FUSRAP covers a number of sites used by the Army Corp of Engineers for uranium and thorium research. These sites are located across the United States and many need no remediation because contamination is well below acceptable standards. Others are to be stabilized using concrete encasements, in place burial, or outright removal of the material. The work in this program is expected to be complete by the year 2000.

- **The Surplus Facilities Management Program (SFMP):** The SFMP was established in 1978 to manage the cleanup of government owned facilities used for the

nuclear energy programs that have since been discontinued. More than one-hundred sites have been identified containing over 2000 distinct contaminated locations (Hanford is one) [14]. The sites are to be cleaned by scraping and removal, then stabilizing the soils using bio-barriers such as a combination herbicide and plastic sheeting. In decommissioning contaminated burial grounds, the waste is to be rendered inert and the residues immobilized [35]. Discharge of waste directly into the soil was common at these sites.

Where containment structures exist, failure of these structures may have led to further discharge into the soil [68]. Structures in the SFMP are to be stored, entombed, or dismantled. The performance of some structures have been evaluated; for example, at Maxey Flats, Kentucky, tracer tests showed groundwater movement from a waste trench [99].

There is good potential for the ERT method to serve to remediate radioactive contaminated sites. It could characterize subsurface geological structures to define extent, location, orientation, material, and moisture level in the contaminants. Groundwater and pollution plumes could be located while water table levels and sources of contamination and barriers could be located and tested. The ERT method can monitor remediation activities: characterize hydrological processes affecting contaminant transport; select appropriate alternatives; and demonstrate regulatory compliance. Since it is a remote-sensing method, application need not significantly disturb the subject and this eliminates or reduces the need for drilling and thus, destructive modification of any confinement system. Data acquisition is quick and simple and sensors are robust and low in cost. The ERT method gives true three-dimensional analysis, and can be applied under a wide range of conditions.

1.5.2 For Detection of Buried Ordnance

The Defence Research Establishment, Suffield, Alberta, has been investigating technologies to detect buried ordnance. The detection of ordnance detection is complicated by

overburden that acts as an energy absorbing shield.

Hidden explosives can be divided into three major categories: 1) unexploded ordnance such as buried artillery shells and aerial bombs; 2) sea and land mines; and 3) improvised explosive devices, such as terrorist bombs. Detection methods are distinguished by whether they detect explosives directly or indirectly [64]. Of the options available, or showing promise, a combination four has been selected for field testing (J.E. McFee, personal communication): 1) nuclear magnetic resonance; 2) metal detection; 3) electromagnetic inductive devices; and 4) trace gas analysis. Combining methods decrease the false alarm rate, but there is an attendant increase in cost and in the complexity of the multiple sensor system.

Table 1.4 summarizes technologies being considered and currently used for the detection of buried ordnance along with a comparison of relative features and benefits. The description of the approaches are expanded in the discussion following:

- Electromagnetic induction (EMI) detectors use an inductive loop to excite the metallic material in the target and one or more secondary loops to measure the resultant eddy currents [20, 21]. Electromagnetic induction works well to detect a buried target, but is limited when delineating features such as size, shape, and location.

- Nuclear magnetic resonance (NMR) is used to detect explosives directly from the radiofrequency resonance absorption spectrum, i.e., the magnetic moments of nuclei or electrons that absorb energy at characteristic frequencies [47]. Nuclear magnetic resonance can be tuned to nitrogen or hydrogen in explosive materials but the method itself is expensive and generally hard to put into practice. The method has detected explosives in letter bombs where it is simple to apply since volumes are small and targets better localized.

- Magnetometers can be used to detect changes in the earth's local magnetic field due to the presence of metal [63]. Although newer and more advanced explosive devices

do not always have metal components, the older style devices have metal and they comprise the vast majority of all such devices. Another problem with magnetometers is most of the metallic material in targeted areas have significant amounts of shrapnel that confuse the detectors.

- Trace gas analysis can be used for vapour detection. There are three viable trace gas techniques: mass spectrometry; ion mobility spectrometry; and laser/optical techniques. Trace gas analysis is difficult to implement in a field setting because the target must be confined for a time to allow sufficient quantities of gas to accumulate. Generally, 500g of TNT can be detected when double wrapped in polyethylene after one hour in a confined room [64]. To detect a hermetically sealed case through overburden, an order of magnitude increase in sensitivity is needed. Systems of sufficient sensitivity are commercially available.

The ERT method shows potential for detecting buried objects including plastic materials. Figure 1.2 shows one concept of how the ERT method could be applied. This is a tracking vehicle with an ERT electrode grid fixed on a platform that can be lowered during measurement. Excessive computing time and crude results are drawbacks of the ERT method in this application—at this point in the dissertation [64]. However, this dissertation will show that the first of these problems can be overcome to make the method more viable.

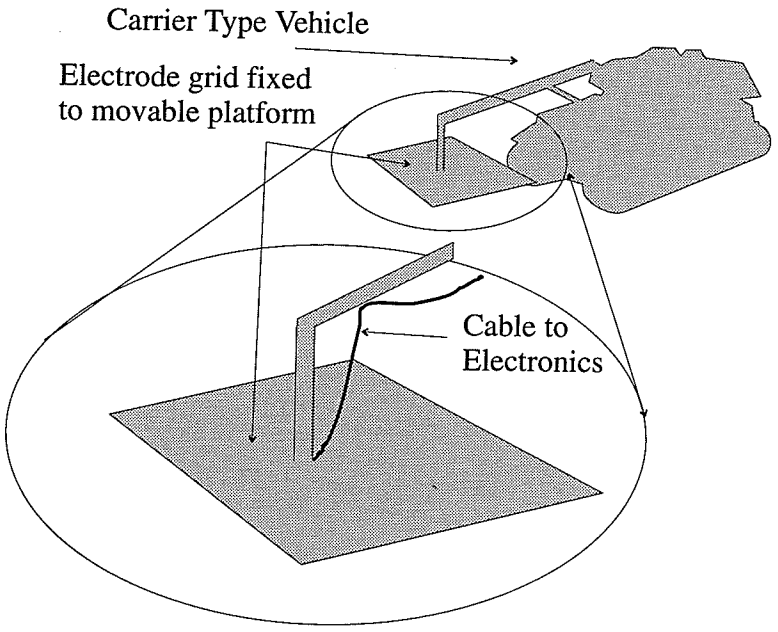

Figure 1.2: Concept for detecting buried ordnance.

Table 1.2: Use in environmental characterization. There have been many successful studies to apply the ERT method for environmental remediation.

Publication	Application	Scale of Problem	Electrodes	Data Processing
Tamburi et al. 1987	Measure water plumes in landfill site	84m × 84m × 36m	64	$3-D$ Wexler[96]
Daily et al. 1987	Measure hydration cycles in tuff	10cm × 8cm	20	$2-D$[16] backprojection
Rameriz and Daily 1990	Measure grout penetration in rock fracture	10m × 10m	16	$2-D$[71] backprojection
Daily et al. 1992	Measure water injection	20m × 15m	16	$2-D$ [100]
Westinghouse Report 1993	Measure air sparging	30m × 20m	20	Not reported
Schima et al. 1993	Sparging in groundwater	30m × 30m	48	$2-D$ [34]
Rameriz et al. 1995	Measure steam sparging	32m × 18m	16	$2-D$ [100]
Daily et al. 1995	Measure release and sparging	10m × 5m	55	$3-D$ [18]
LaBrecque et al. 1995	Measure contamination and sparging	scale - $7m$	105	$3-D$ [55]
Zhang et al. 1995	Measure leaking ponds	scale - km	25	$3-D$ [60, 109]
Ellis and Oldenburg 1994	Geophysical prospecting	scale - km	121	$3-D$ [33]

Table 1.3: American radioactive waste management programs.

Program	Waste Type	Scale of Problem	Approach	Use of ERT Methods
NTS	Airborne contamination	M's to 100Km's	Removal or stabilization	Monitor stripping activities, chemical immobilization, soil vapour extraction, characterize environmental parameters, and verify regulatory compliance
UMTRAP	Liquid and	M's to Km's	As above	As above
FUSRAP	solid, air	M's to Km's	As above	As above
SFMP	and ground–water borne Leaking Tanks	M's to Km's	As above	As above

Table 1.4: Ordnance detection.

Method	Principle	Limitation
Metal detector	Sensitive to effect of metal on Earth's magnetic field	Requires metal components Point reading
NMR	Tuned to Larmer frequency of common bomb materials	Difficult to apply in field Point reading
Trace Gas Analysis	Detects vapours of explosive materials	Needs specific conditions Point reading
EM Induction	Measures response field to applied EM signal	Sensitive only to metals
ERT Methods	Detects conductivity variations Can be applied to plastics	Processing is slow Depth-related problems

Chapter 2

Inverting Electrical Resistivity Tomography Data

2.1 Overview

Chapter 2 discusses background, features, and processes for inverting ERT data, with emphasis on the algorithm used throughout this dissertation. It is based on the standard approach of minimizing the difference between the forward and inverse problems as defined by an objective function. The result, when this process has converged on the minimum of the objective function, is the best fit model to the data.

The use of multi-dimensional ERT methods for environmental applications was first proposed over fifteen years ago [24]. In the original development of the ERT method, it was recognized that a gradient optimization scheme would adjust the model of a subterranean conductivity distribution until it matched the measurements [26]. However, the resultant system of equations was dense and to solve the system of equations was beyond the capability of the available computing technology of that time. Recent methods use sparse matrices to substantially reduce resource requirements during the inversion process.

Starting early in the formulation of the theory, different types of data processing techniques have been developed. For example, Yorkey et al., [108] described the perturbation method, equipotential lines method, and double constraint methods. The perturbation method was first proposed in [50] but later modified in [107]. More recently, a modified

perturbation method was presented that computed the percentage change in voltage measurements due to changes in resistivity [52, 53]. Another code, "OCCAM", has been used extensively in environmental applications in two and three dimensions [54, 55].

The equipotential lines method [5] calculates the differential voltage measurements for a homogeneous resistivity distribution and the equipotential paths ending on the voltage-measuring electrodes. The resistivity distribution is corrected using an average of the product of the resistivity between equipotential lines and the ratios of the measured-to-calculated voltages.

The double constraint method was first proposed in [105]. The forward model is computed for the known current sources to compute the current density throughout the mesh. The inverse problem computes the voltage gradients throughout the subject, constrained to match the observed voltages. From this result, corrections to the resistivity distributions are computed.

2.2 The Algorithm of Wexler

The data processing algorithm used in this dissertation research was the algorithm of Wexler [7], first presented to the Optical Society of America, Hecla Island, Manitoba, 1985 [105]. It has been further developed and expanded in Appendix A, in [65, 79, 102], and in patent applications [103, 104]. Similar methods have been published since [42, 51, 108] and these particular approaches have since been called the double-constraint method [7].

The approach starts by defining the residual, or objective function, as

$$R = \Sigma_X \int\int\int_v (\underline{J} + \kappa\nabla\phi) \cdot (\underline{J} + \kappa\nabla\phi)\partial v. \tag{2.1}$$

In words, Equation 2.1 states that the error is the difference between forward and inverse problems. Equation 2.1 is expanded, then differentiated with respect to each degree of freedom κ_i, and then solved to generate a value for the update

$$\kappa_i = \Sigma_X \int\int\int_{v_i} \underline{J} \cdot \nabla\phi\partial v / \Sigma_X \int\int\int_{v_i} \nabla\phi \cdot \nabla\phi\partial v. \tag{2.2}$$

During inversion, admittance is determined from the field equations and the updated distribution is calculated based upon differences between the computed field values and the measured values [17]. Measurements are taken on the boundary.[1] Starting with an initial admittance, the system is solved for the current distribution for the forward problem and the voltage distribution for the inverse problem. The updated admittance is computed from the result. This is repeated until a threshold is reached, based on the minimum of the residual [102, 105].

The algorithm proceeds from Equation 1.1:

STEP–I A homogeneous body with constant conductivity is defined as the initial resistivity. Equation 1.1 is solved for the forward problem, given the Neumann boundary conditions

$$\kappa(s)\partial\phi/\partial n|_s = h(s) \tag{2.3}$$

where $h(s)$ is the current density at the boundary. Equation 2.3 may be solved using a finite-element method to determine the potential distribution while the current (J) is determined using (Ohm's law)

$$J = -\kappa(s)\nabla\phi. \tag{2.4}$$

Solving Equation 2.3 by finite elements generates a system of equations of the form

$$S\Phi = b \tag{2.5}$$

where S is the stiffness matrix, b is the column matrix of the sources, and Φ is the column matrix of the nodal voltages, or the model of the electric field. The column matrix b, contains the boundary current distribution. The stiffness

[1] In this dissertation, boundary is an abstract mathematical concept and refers to the nodes where conditions are known: voltage for dirichlet boundary conditions, and current for neumann boundary conditions. This differs from the conventional view where the boundary has a physical analog, i.e., the interface between distinct regions.

matrix S, is assembled from the Gauss points in the finite-element mesh and the voltage Φ, is the unknown electrical potential vector.

STEP–II The processing ends if the model b, from the forward and inverse problem, are within a predetermined tolerance of each other.

STEP–III Equation 1.1 is solved for the potential distribution using Dirichlet boundary conditions

$$\phi(s) = g(s) \tag{2.6}$$

where $g(s)$ gives the known voltages. The electrical potential vector, constructed from unknown values and field measurements, constrains the model by reducing the system or, as was done in this implementation, by multiplying the diagonal value of the stiffness matrix and the corresponding right hand side element by a relatively large value [48].

STEP–IV A new value of κ is calculated to minimize the residual in Equation 2.1 and the update admittance computed from Equation 2.2 using $\underline{J}$ as determined from STEP–I. The ϕ vector is determined from STEP–III.

STEP–V The process is repeated from STEP–I using the result from STEP–IV for the κ. Figure 2.1 illustrates the data-processing algorithm in a flow-chart.

2.3 Other Inversion Algorithms

Other algorithms have been developed for the inversion of ERT data and two function minimization schemes [7] are reviewed to illustrate. Ellis and Oldenburg [33] define an objective function for the inversion as

$$S[m] = S_D[m] + S_M[m] \tag{2.7}$$

where

$$S_D[m] = \Sigma_X((d_i^{obs} - d_i^{cal}[m])/\delta d_i^{obs})^2$$

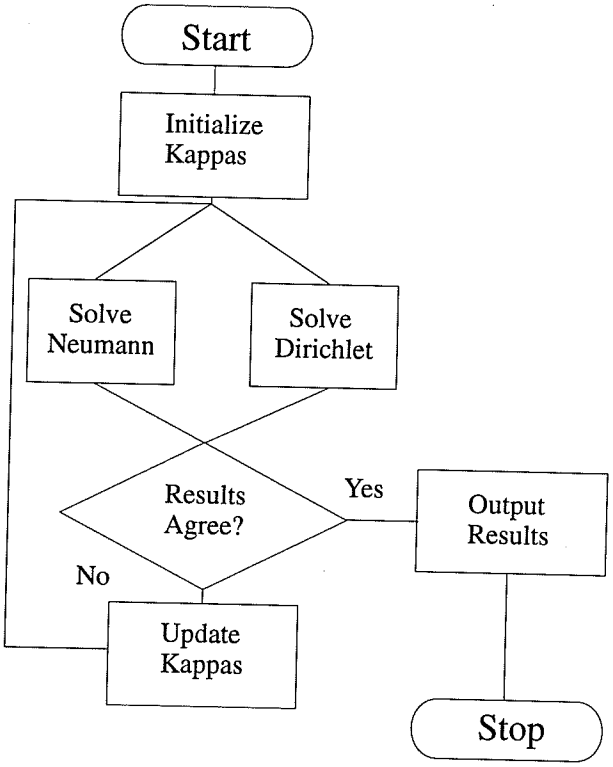

Figure 2.1: Data processing flowchart.

and

$$S_M[m] = \mu \int_V (Wm(x))^2 \partial x$$

are defined in the model space $m \in M$. The S_D is the data misfit term, the S_M term is the model character, and W is a model constraint condition. The integral is taken over the volume of the target. Where the Laplace operator is used for W, S_M becomes a measure of the smoothness of the fit to the data. Although the inversion of ERT data is normally an illconditioned problem, Equation 2.7 is well-posed.

It was shown [33] that the change of S_D in the model space, i.e., δS_D with respect to

m can be written as

$$\delta S_D[m]/\delta m_i = 2\int_V g[m](\underline{x})\nabla(\Phi_i(\underline{x})d^{cal}(\underline{x}))\partial x^3 \tag{2.8}$$

where

$$d_i^{cal}[m] = \int_V \delta(\underline{x}_i^{obs} - \underline{x})u(m)(\underline{x})\partial x^3 \tag{2.9}$$

$$g[m](\underline{x}) = \Sigma G[m](\underline{x};\underline{x}_i)(d_i^{obs} - d_i^{cal})/(\delta d_i^{obs})^2 \tag{2.10}$$

and G is the Green's function. The change in the data misfit term is shown to be

$$\delta S_M[m]/\delta m_i = 2\int_V \Phi_i(\underline{x})((1-\epsilon)\nabla^2 - \epsilon)((1-\epsilon)\nabla^2 - \epsilon)m(\underline{x}))\partial x^3. \tag{2.11}$$

The parameter ϵ controls the smoothness.

The goal is to minimize this objective function. Equation 2.7 is minimized using the conjugate gradient method. In synthetic tests and field measurements, the method was found to be reliable and efficient. The approach, it was concluded, would be useful in mineral exploration [33].

With the ERT inversion code "OCCAM", [55] a similar approach was developed using an objective function of the form

$$\Phi(\underline{P}) = \chi^2(\underline{P}) + \alpha\underline{P}^T\underline{R}\underline{P} \tag{2.12}$$

where $\underline{P}$ is the model parameter, $\underline{R}$ is the solution roughness, and α is the stabilizing parameter. In this implementation, the χ^2 term provides the measure of the data misfit and the solution is the model for which α is minimized. The χ^2 is a measure of the quality of the fit to the measured data and the second term serves to smooth the model to make the system well-posed. The value of χ is computed as

$$\chi^2(\underline{P}) = [\underline{D} - \underline{F}(\underline{P})]^T\underline{W}[\underline{D} - \underline{F}(\underline{P})] \tag{2.13}$$

where $\underline{D}$ is the vector of known values, $\underline{F}$ is the forward solution, and $\underline{W}$ is a data weighting vector based on the quality of the field data.

The system is inverted iteratively using changes in the parameter space computed as

$$\delta \underline{P}_k = -1(\underline{A}_k^T \underline{W} \underline{A}_k + \alpha \underline{R})(\underline{W} \delta \underline{D}_k - \alpha \underline{R} \underline{P}_k). \tag{2.14}$$

The $\underline{A}_k$ is the sensitivity matrix and is computed as

$$a_{i,j} = \partial F_i(\underline{P}_k)/\partial p_j \tag{2.15}$$

In this notation, p_j is the j^{th} element of P_k and F is the forward solution. The conjugate-gradient method is used to solve for the new parameter vector for each update.

2.4 Algorithm Performance and the Error Function

With the ERT method, as with many other inverse modelling methods, it is the error function that is minimized to derive an expression for the updated admittance. For synthetic data, the model is known exactly and the error is the least-squares difference between the known and the computed values,

$$\mathcal{E}^2 = (1/N^2)\Sigma_X(\kappa_i^{actual} - \kappa_i^{computed})^2. \tag{2.16}$$

In Equation 2.16, N is the number of unknowns and the sum is taken over all unknowns. Where the model is not known, as for real data, the best fit is when processing converges on a result and no longer shows significant changes with each update, i.e.,

$$\mathcal{E}^2 = (1/N^2)\Sigma_X(\kappa_{i+1} - \kappa_i)^2 = 0. \tag{2.17}$$

In this study, the quality of synthetic data is measured in this manner. An error function will not give an estimate of the accuracy in the result for real data since there is no true image available for the computation. As such, it is a measure of the value of further processing; i.e., does further processing change the result? To rely on such an error function can be misleading since the true quality of the image may deteriorate while this error function continues to improve. Figure 2.2 are examples of how Equations 2.16 and 2.17 behave.

The quality of the image is not the only issue to consider. The speed of convergence and the amount of computing resources is important, as well as the stability of the system. Many ERT processing algorithms are ill-conditioned and sensitive to precision errors during the computations. For example, the Newton-Raphson method, where it is the boundary residual that is minimized [107, 108] is sensitive to precision error. The most significant calculations are matrix inversions performed during the model inversion and, for the algorithm of Wexler, two matrix inversions are performed for each excitation pair, at each iteration. Substantial improvements in performance can be achieved by improving the matrix solver routine. This study implemented several different solver schemes used during inversions including standard Gaussian [38], frontal [31, 45, 77, 78], Jacobi [36, 38, 69], conjugate gradient [69], and Gauss-Seidel [36, 38, 69]. The last three are iterative matrix solvers using some starting point for the process. Iterative methods can be particularly effective in these sorts of applications since the system is solved repeatedly and previous solutions make excellent starting points for the next step. However, due to the topology of the stiffness matrix, matrix inversion by iterative methods is not guaranteed to converge and so these methods were not considered beyond a few preliminary tests. As well, because of the extensive experience with the frontal solver routine MA32, available commercially[2], all results in this dissertation were generated using the MA32 routines.

2.5 Determinacy

With the ERT algorithm used here, any dataset can be inverted no matter how sparse. However, the mathematics has something to say about the determinacy of the system and the level of confidence in the result. The determinacy is dependent on the number of unknowns in the system, the measurement strategy, and the number of linearly independent measurements. During the inversion process, the number of unknowns (U) is the number of nodes in the finite element mesh at which values are solved. Different excitation strategies

[2]Harwell UK.

can be employed where measurements from excitation electrodes are used "*always*" for every excitation (M_a), "*sometimes*" when an electrode is not used for as the excitation electrode (M_s), and "*never*" if excitation electrodes are not used in any voltage measurements (M_n) [65]. The *sometimes* pattern is the ideal approach in practice since it uses all possible combinations for the calculations other than those affected by the contact resistance at the excitation electrodes.

Where there are E electrodes in a problem, there are $E!/2$ unique possible excitation pairs (P), i.e.,

$$P = (E)(E-1)/2$$

The result has been divided by 2 to consider when the same two electrodes are used as anode and cathode, but with roles reversed. This leaves a total number of $(E-2)$ unique measurements.

The determinacy (D) is the ratio of the number of independent measurements to the number of unknowns. The maximum determinacy (D_{max}) of the *sometimes* problem is the ratio of the number of linearly independent measurements possible to the number of unknowns in the problem, i.e.,

$$D_{max} = P \times (E-2)/N = (E)(E-1)(E-2)/2N.$$

If this number is less than 1, the system is under-determined; if equal 1 it is fully-determined; otherwise, it is over-determined. On a discrete mesh, any system that is fully- or over-determined can be recovered exactly. In a continuum, the more determined a system is, the fewer iterations to converge and the greater the confidence in the result [65].

In applying the ERT method, the number of excitations is maximized while considering practical limitations. In all cases presented here, the pattern included an even balance of short-, medium-, and long-spacing excitations with as even a coverage of the target as was possible. The actual excitation patterns used for both synthetic and field data is included as Appendix C.

2.6 Discussion

In ERT data inversion, resistivity is determined from the Poisson equation and is considered the best model when the difference between the forward and the inverse problem has been minimized. The algorithm of Wexler is one method used for inverting ERT data and is the method used in this research. The inversion is nonlinear and is solved iteratively by starting with an initial conductance, then solving the current distribution for the forward problem and the voltage distribution for the inverse problem. The result is used to calculate the updated conductance at each step.

Several points on detail such as notation are made here to aid the reader in this discussion.

1. Data processing for the ERT method was developed using synthetic images where both conductance and distance are normalized. In these cases, units of scale have not been included in the figures.

2. The ERT relevant electrical properties of materials are the conductance, admittance, resistance, and reactance. Terminology for ERT has evolved from classical resistivity methods and that includes the term "resistivity" itself. Resistivity considers the volume in which the current flows, to normalize the measurement to be independent of electrode separation. Most electrical terms have been used at different points in this discussion. The conductance is the physical property generally computed here and is the inverse of the resistance.

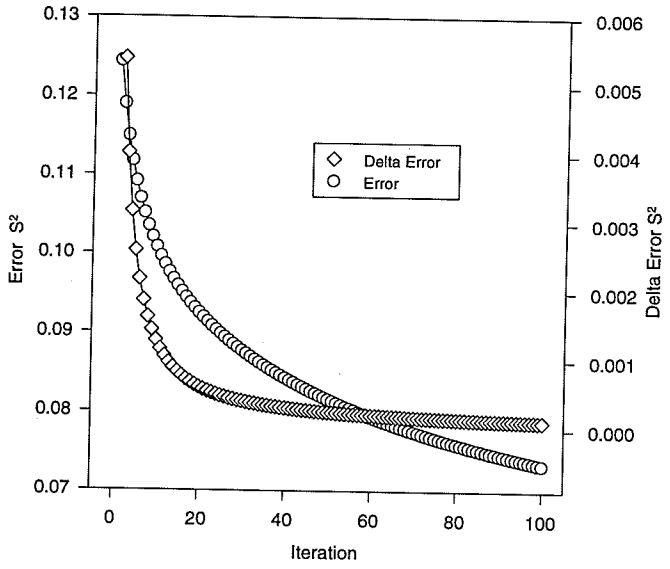

Figure 2.2: Error versus iteration. The "delta" error is a measure of how much the image is changing with iteration and represents an acceleration.

Chapter 3

The Issue of Slow Convergence

3.1 Overview

As discussed in Chapter 2, this dissertation uses the algorithm of Wexler for inverting ERT data. One characteristic of this algorithm is that it is slow to converge. Recent work has accelerated the convergence of this algorithm and Chapter 3 demonstrates the limited success of several approaches. Three approaches were considered for this discussion: a modified perturbation method, an adaptive filter method[1], and a peak-detection filter. Together, they set the stage for the improvements developed in Chapter 4.

There have been many studies conducted using synthetically generated data. They have considered performance in terms of mesh geometry, convergence characteristics, resource requirements, matrix densities, and location of anomalies. Tests have considered the effect of noise and measurement error, such as inaccurate positioning of the electrodes and electrode motion due to subject movement during monitoring [65]. Studies using real data are less common with few done in three dimensions. The tests performed here deal directly with the issue of speed of convergence and, incidentally, with the quality of the result.

3.2 Slow Convergence

The algorithm of Wexler is slow to converge: often requiring thousands of iterations. To overcome this problem, three approaches were implemented that applied corrections for a

[1]This is the termonology used in this dissertation for lack of a better one

better estimate for the update. They were peak-detection filtering, an adaptive filter, and a modified perturbation method.

- **Peak-Detection Filter:** In peak-detection filtering, a criterion ($\kappa_{criteria}$) is set where admittance exceeding it are processed in a modified manner. The new update is

$$\kappa_{i+1} = \begin{cases} \kappa_i & \kappa_i \leq \kappa_{criteria} \\ \kappa_i + \triangle_{maximum} & \kappa_i > \kappa_{criteria} \end{cases} \tag{3.1}$$

  This filter emphasizes contrasts, amplifying those exceeding the criteria while holding the others constant. Implicit in this approach is a need for careful control when selecting the $\kappa_{criteria}$ since it does not discriminate between real contrasts, artifacts, or noise. A further consideration is that if no anomalous features are present, this filter can introduce artifacts where none would otherwise exist. Other criteria can be introduced such as when to apply the filter.

  Results, with and without peak-detection filtering, are shown in Figure 3.1 with the error shown in Figure 3.2. Figure 3.3 shows the same peak, recovered with peak-detection filtering on a finer grid where the density of the elements has been increased.

  Because of the processing criteria, peak-detection filtering requires *a priori* knowledge of the subject under study. These criteria can be tuned using this information and to make the method effective with a minimal amount of processing. Peak-detection filtering works well when anomalous features are to be detected, but is not suitable for subtle contrasts.

- **Adaptive Filter:** A characteristic behaviour of the algorithm is that each degree of freedom oscillates about the solution, with decreasing amplitude, as processing advances. Figure 3.4 illustrates this behaviour. To correct for this, the update was modified using the trend from the previous two conductances. The modified update

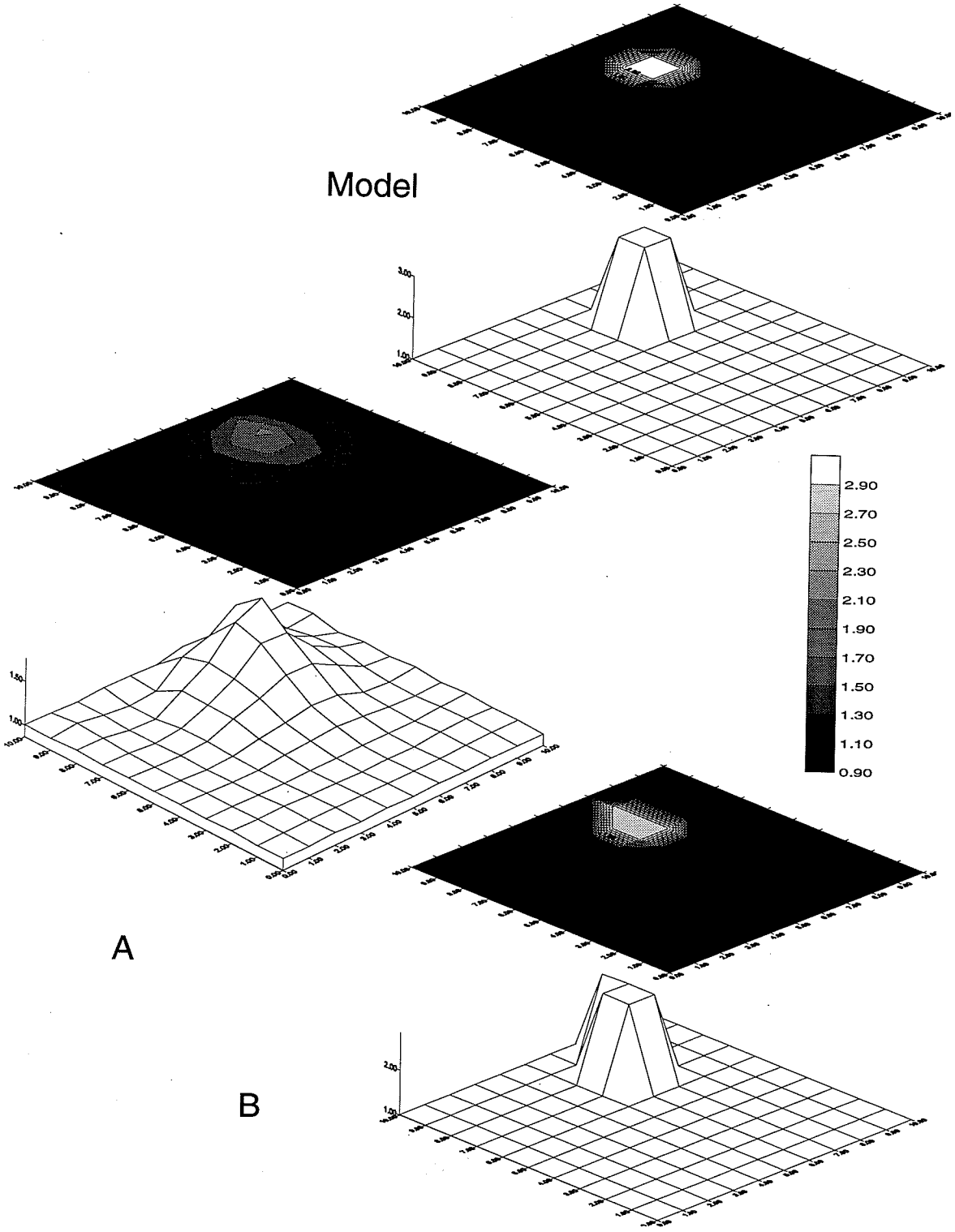

Figure 3.1: Processing with peak-detection filtering. There were 121 unknowns, 18 excitation pairs, 20 electrodes, and an initial impedance of 1 was used. The processing was executed for 200 iterations without peak-detection filtering (Figure 3.1A) and three iterations with peak-detection filtering (Figure 3.1B).

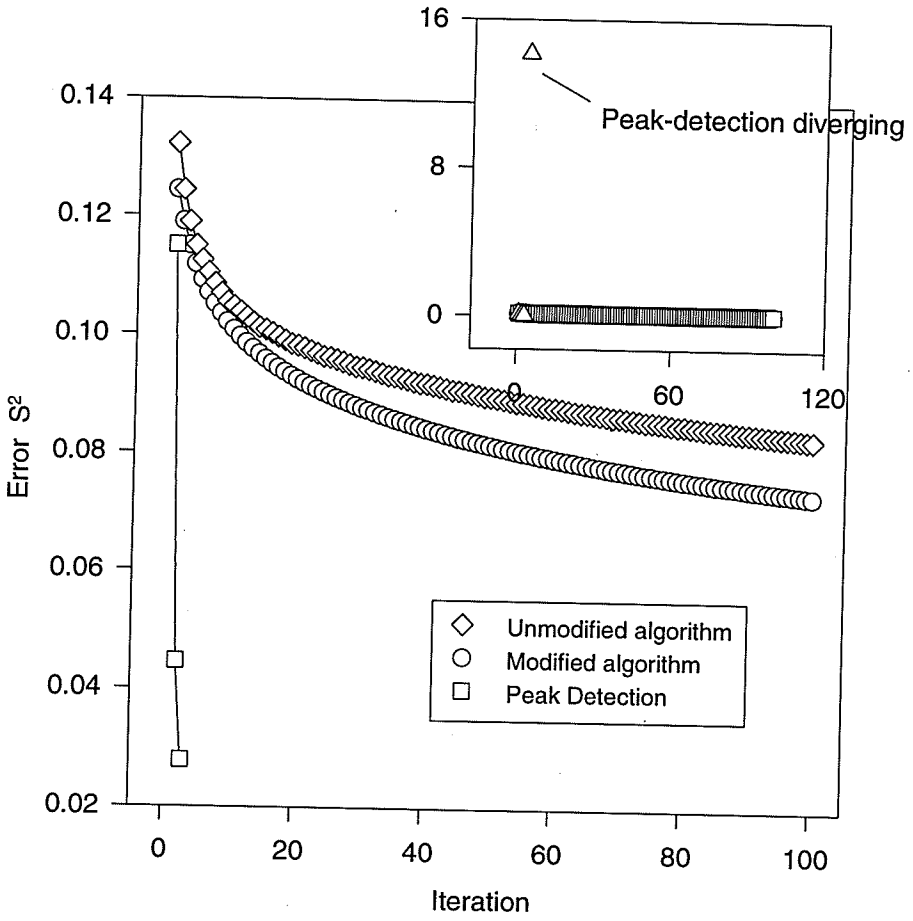

Figure 3.2: Error with peak-detection filtering. Dramatic results are possible with peak-detection filtering by adjusting the filter parameters such as the threshold and when the processing is stopped. Processing was stopped at the third iteration. As illustrated by the inset, it rapidly diverged immediately there after.

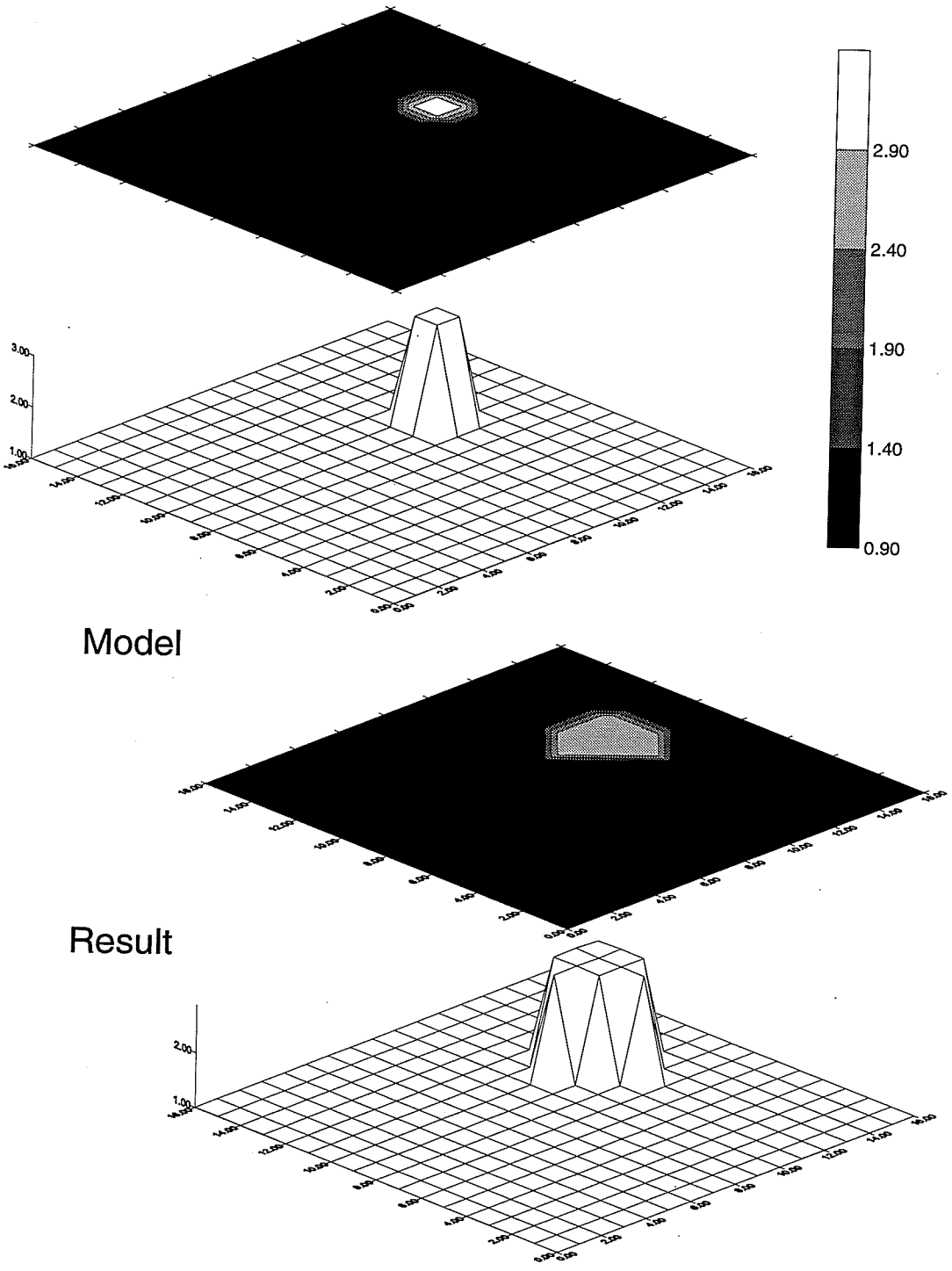

Figure 3.3: Peak-detection filtering on a fine grid. For this result, there were 289 unknowns, 18 excitation pairs, 20 electrodes, and an initial conductance of 1 was used. The processing was executed for three iterations.

was

$$\kappa_{i+1} = \begin{cases} \kappa_i & |\triangle_i| < |\triangle_{i-1}| \\ & \text{(and set } \triangle_i = \triangle_{i-1}) \\ \kappa_i + \triangle_i & \text{otherwise–the normal update} \end{cases} \tag{3.2}$$

Figure 3.5 shows the result when this modification was used.

- **Perturbation:** A further modification introduced a perturbation factor ω where

$$\kappa_i = \kappa_{i-1} + \omega \triangle_{i-1} . \tag{3.3}$$

Applied to all pixels, this accelerates processing when $\triangle$ is > 1 and dampens it when $\triangle$ is < 1. This is similar to the modified perturbation method outlined in [53] and is based on [65]. The perturbation can be applied to all degrees of freedom and then again in regions where the admittance distribution indicated a peak, as part of the peak-detection filter [65]:

$$\kappa_i = \kappa_{i-1} + \omega^2 \triangle_{maximum} . \tag{3.4}$$

Figure 3.5 shows the response considering ω in the range from 0.5 to 5.0. The case where $\omega = 10$—and those with ω larger—immediately diverged. It should also be noted that the modification gave a poorer result at an intermediate step: when $\omega = 2.0$.

When peak-detection filtering and the perturbation method are used together, modifications are being applied to accelerate to the solution and to accentuate peaks. Simultaneously tuning these unrelated processes is difficult and any implementation should allow independent control of both parameters.

3.3 Discussion

The enhancements discussed, peak-detection filtering, adaptive filter, and the perturbation approach, offer certain advantages over the unmodified algorithm. They cut down on the

Table 3.1: Auto-computing the Initial Image. A 11×11 mesh, with an object of amplitude three in a background of one, and Equation 3.5, was used to automatically compute an intial image.

Object Size (Pixels)	Computed Value (Normalized)	Object Size (Pixels)	Computed Value (Normalized)
Actual	1.000	4	1.1085
1	1.105	5	1.109
2	1.106	6	1.111
3	1.107	9	1.114

number of iterations needed for convergence and, under certain conditions, they increase confidence in the solution. These methods require *a priori* information of the target for parameters in the update and they can cause the system to become unstable when care is not taken.

Peak-detection filtering, discussed extensively in the literature [39], is suited for high contrasts. This can be useful for distinctive targets but it is of no value for applications in general. The issue of slow convergence remains a significant one at this point in the dissertation and, having raised this issue, the discussion leads into the improvements presented in Chapter 4.

Near the completion of the research of this dissertation, the background conductance was computed from the measurements using the formula

$$\kappa = 2 \times (s \times I)/(V_{anode} - V_{cathode}) \tag{3.5}$$

where s is the separation between the excitation electrodes. This formula consistently generated a value, depending on the image being inverted, that was within approximately 10% of the actual background. Table 3.1 shows the values computed for a two-dimensional 11×11 problem. The resistivity will be dependent on geometry, the position of the excitation electrodes, and the resistivity distribution: the computation is an approximation.

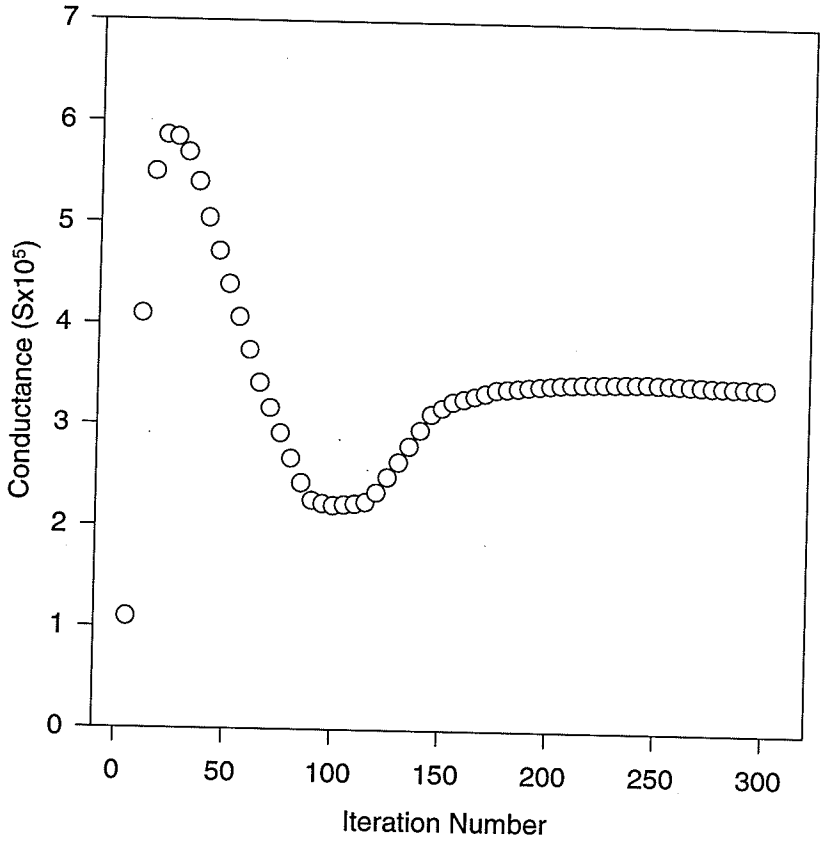

Figure 3.4: Characteristic oscillation. The values of a single degree of freedom are plotted against iteration.

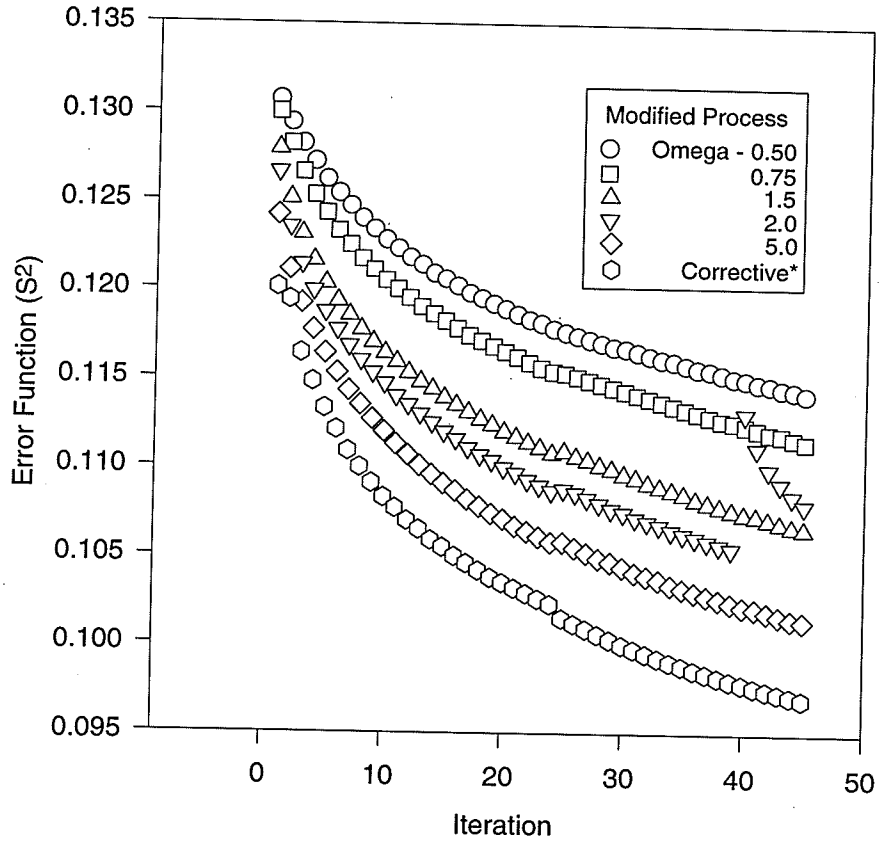

Figure 3.5: Perturbation and adaptive filter methods. The resolution gain using the model of Figure 3.3 is limited and where $\omega = 2$, the processing does not approach the limit smoothly. There were 121 unknowns, 18 excitation pairs, 20 electrodes, and an initial impedance of 1 was used.

Chapter 4

Acceleration to Convergence

4.1 Overview

Enhancements to make the algorithm of Wexler faster, such as those presented in Chapter 3, are useful in a limited number of circumstances. Their performance is object dependent and so they have limited application. To address this shortcoming, a general, object independent multistep approach is developed in Chapter 4. It significantly improved on the performance of the algorithm of Wexler, as demonstrated by tests with two- and three-dimensional synthetic data. When the method was applied with three-dimensional field data, it led to an improvement of approximately two orders of magnitude.

The arguement of this chapter starts with a mathematical statement of the general problem: that of solving for the roots of a nonlinear system. This type of problem is often solved using an iterative method that can be accelerated using any one of a number of multistep approaches.

The novel, multistep approach of this dissertation is presented for the general problem. The approach is to compute the limit as the number of iterations goes to infinity to give an improved estimate of the update. The approach is illustrated with the Jacobi method, an often used, iterative method for inverting a set of nonlinear equations. The method is then applied to the algorithm of Wexler where it is demonstrated with two- and three-dimensional data: both synthetic and real. Filtering is also considered and benchmark comparisons tabulated.

4.2 Mathematical Statement of the Problem

The problem of solving the roots of a nonlinear system is a numerical problem formulated as

$$\underline{f}(\underline{\zeta}) = \underline{0}, f : \mathcal{D}\epsilon\Re^n \rightarrow \underline{0}^n, \tag{4.1}$$

or, equivalently

$$\underline{g}(\underline{\zeta}) = \underline{\zeta}, g : \mathcal{D}\epsilon\Re^n \rightarrow \mathcal{R}\epsilon\Re^n. \tag{4.2}$$

The objective function of the algorithm of Wexler is defined by Equation 2.2 where the variable $\underline{\zeta}$ of Equation 4.2 corresponds to the admittance. Admittance is implicit in the right-hand side of Equation 2.2 and explicit in the left-hand side, thereby directly taking the form shown in Equation 4.2.

4.3 Multistep Methods to Improve Convergence

An important characteristic of an iterative method is the number of steps for convergence, i.e., the speed to converge. In general, a multistep method will speed convergence by improving the update at a step using an n^{th} order fit to the trend displayed by previous updates. This is repeated as the process advances for improvements from each application.

4.3.1 The Multistep Approach

Multistep approaches are well developed in the literature (Milne's and Adam's methods [38] are examples). In general, they use polynomial representations for the fitting function. In theory, the accuracy of the prediction can be improved by increasing the order of the polynomial. However, this is limited by two factors: 1) the order is limited by the number of previous updates available; and 2) the higher-order terms of the fit is subject to significant computational errors due to roundoff. This is a limitation when considering the algorithm of Wexler because high-order terms contribute significantly to the fit early in the processing as displayed in Figure 3.4.

4.3.2 A Novel Multistep Approach

Computing the roots to Equation 4.2 using an iterative approach forms a sequence

$$\{\underline{\zeta}_0, \underline{\zeta}_1, ..., \underline{\zeta}_i, ...\}.$$

Each series element is a computation at a step in the process and is generated from the previous step using an estimate of the error $\underline{\triangle}_i$, and $\underline{\zeta}_{i+1} = \underline{\zeta}_i + \underline{\triangle}_i$. The roots, where they exist, are

$$\lim_{i \to \infty} \underline{\zeta}_i. \tag{4.3}$$

Equation 4.3 can be recast as $\underline{\zeta}_i \rightarrow \underline{\Gamma}^k$ where k is an index over the degrees of freedom in the solution vector and the elements of the vector $\underline{\Gamma}^k$ are Γ^k_i. The result is a set of n sequences, $\underline{\Gamma}^k = \{(\Gamma^k_0, \Gamma^k_1, ..., \Gamma^k_j, ..., \Gamma^k_q)\}$, where each sequence has length equal to the number of iterations computed: q in this case.

By hypothesis, there exists a process-dependent function $\Phi^k(i)$ that fits the set of points $\{\Gamma^k_i\}$ and is constrained such that $A^k \leq \lim_{i \to \infty} \Phi^k(i) \leq B^k$ for all k and with $A^k = B^k$ in the limit. This is the characteristic equation of the iterative method and it has the general form

$$\Phi^k(i) = \sum_{j=1}^{m} \alpha^k_j f_j(i). \tag{4.4}$$

This characteristic equation can be defined using a set of functions f_j that are characteristic of the iterative proces and a set of $k \times m$ parameters α_j in the fit. The fit is parameterized using the iteration number i.

The $\underline{\alpha}$ is a parameter implicit by the definition of the characteristic equation. Each set $\underline{\alpha}$ is unique for each degree of freedom: determined by fitting the characteristic equation to values from past updates of each degree of freedom. As $q \rightarrow \infty$, both formulations must compute the limit of an infinite sequence. However, where $\zeta^k_i(\underline{\zeta})$ has n degrees of freedom, each $\Phi^k(i)$ has a single degree of freedom and for this reason is simpler to extrapolate to the limit once the sequence $\{\Gamma^k\}$ is known.

Table 4.1: The approach simplified. In this illustration, the model has n degrees of freedom and the processing was performed for q iterations. The model vector corresponds to each column and is updated at each step of the inversion process. The approach here is to separate each variable in the model along rows, then extrapolate independently for all the limits ζ_i^{∞}

Degree of freedom	Iteration 0	1	2	3	4	5	6	...	q	...	∞
0	ζ_0^0	ζ_0^1	ζ_0^2	ζ_0^3	ζ_0^4	ζ_0^5	ζ_0^6	$\cdots$	ζ_0^q	$\cdots$	ζ_0^{∞}
1	ζ_1^0	ζ_1^1	ζ_1^2	ζ_1^3	ζ_1^4	ζ_1^5	ζ_1^6	$\cdots$	ζ_1^q	$\cdots$	ζ_1^{∞}
2	ζ_2^0	ζ_2^1	ζ_2^2	ζ_2^3	ζ_2^4	ζ_2^5	ζ_2^6	$\cdots$	ζ_2^q	$\cdots$	ζ_2^{∞}
3	ζ_3^0	ζ_3^1	ζ_3^2	ζ_3^3	ζ_3^4	ζ_3^5	ζ_3^6	$\cdots$	ζ_3^q	$\cdots$	ζ_3^{∞}
4	ζ_4^0	ζ_4^1	ζ_4^2	ζ_4^3	ζ_4^4	ζ_4^5	ζ_4^6	$\cdots$	ζ_4^q	$\cdots$	ζ_4^{∞}
5	ζ_5^0	ζ_5^1	ζ_5^2	ζ_5^3	ζ_5^4	ζ_5^5	ζ_5^6	$\cdots$	ζ_5^q	$\cdots$	ζ_5^{∞}
6	ζ_6^0	ζ_6^1	ζ_6^2	ζ_6^3	ζ_6^4	ζ_6^5	ζ_6^6	$\cdots$	ζ_6^q	$\cdots$	ζ_6^{∞}
7	ζ_7^0	ζ_7^1	ζ_7^2	ζ_7^3	ζ_7^4	ζ_7^5	ζ_7^6	$\cdots$	ζ_7^q	$\cdots$	ζ_7^{∞}
8	ζ_8^0	ζ_8^1	ζ_8^2	ζ_8^3	ζ_8^4	ζ_8^5	ζ_8^6	$\cdots$	ζ_8^q	$\cdots$	ζ_8^{∞}
$\vdots$	$\vdots$	$\vdots$	$\vdots$	$\vdots$	$\vdots$	$\vdots$	$\vdots$	$\cdots$	$\vdots$	$\cdots$	$\vdots$
i	ζ_i^0	ζ_i^1	ζ_i^2	ζ_i^3	ζ_i^4	ζ_i^5	ζ_i^6	$\cdots$	ζ_i^q	$\cdots$	ζ_i^{∞}
$\vdots$	$\vdots$	$\vdots$	$\vdots$	$\vdots$	$\vdots$	$\vdots$	$\vdots$	$\cdots$	$\vdots$	$\cdots$	$\vdots$
n	ζ_n^0	ζ_n^1	ζ_n^2	ζ_n^3	ζ_n^4	ζ_n^5	ζ_n^6	$\cdots$	ζ_n^q	$\cdots$	ζ_n^{∞}

This approach can be described in simplified terms. Normally the model is advanced n degrees of freedom at a time. The update is difficult to accurately predict because there are n variables in the computation. The approach taken here was to take each degree of freedom and update it independently of the others by making use of the characteristic equation. Table 4.1 illustrates the approach in these terms.

4.3.2.1 Improving the Update

To improve the estimate of ζ for the update, it is necessary to calculate the limit for each $\Phi^k(i)$ (Equation 4.4) as the number of iteration goes to infinity, for each degree of freedom

(k). Once the form of the characteristic equation is known, this starts with determining the set $\{\alpha_j^k\}$ to fit this equation to the response. There are many numerical approaches to do this but the approach used here was to minimize the χ^2 fit for each $\Phi^k(i)$. Once the sets of $\{\alpha_j^k\}$s are determined, each limit is computed directly from Equation 4.4.

The χ^2 value was minimized using three approaches highly suited for computer processing [8]: 1) the grid-search least-squares method; 2) the gradient-search least-squares method; and 3) the least-squares fitting by linearization method. Each generates an independent result. However, in this implementation, they were used together to improve on the accuracy of one end result. The grid-search least-squares method gave an initial result that best ensured convergence in the region of the global minimum of the χ^2 function. This result is used as the starting point for the gradient-search least-squares method which relies on the division of differences and becomes less accurate as the method approaches a minimum [8]. This result was used as the starting point in a final step for least-squares fitting by linearization. In this approach, the function is expanded using a Taylor expansion [58]. When expanding using a Taylor expansion, the error is greater when the initial admittance is far from the minimum because the series is truncated at the n^{th} term which uses the difference in the n^{th} order. The error is an $n+1$ power of this difference. Linearization performs best in the area of a local minimum since the expanded function represents the equation as a perturbation computed from displacements around a known value.

4.3.2.2 The Novel Multistep Approach Illustrated

A 3^{rd} order system of equations is used to illustrate the Jacobi method for inverting a system of equations in an iterative approach [38].[1] Table 4.2 shows the progression of each of the three degrees of freedom as processing advances during each iteration. The data from variable x_1 was used with TableCurve[2] [75] to return the characteristic equation of the

[1] The explicit statement for the system of equations is not needed by the method.
[2] Jandel Scientific, Corte Madera CA

Table 4.2: Jacobi and the multistep method.

Degree of Freedom	Iteration 0	1	2	3	4	5 Jacobi/multi	6	7
x_1	0	1.000	1.095	0.995	0.993	1.002/1.000	1.001	1.000
x_2	0	0.571	1.095	1.026	0.990	0.998/1.000	1.001	1.000
x_3	0	1.333	1.048	0.969	1.000	1.004/1.210	1.001	1.000

method. TableCurve is a personal-computer based software product that fits a set of data using a user selected set from a possible 3304 linear and nonlinear functions using comman numerical methods [8, 75]. The user can also enter an arbitrary function. The functions are ranked according to the χ^2 value of the fit. The equation was selected as the characteristic equation based on the least-squares fit (r^2) to the data [75]

$$y = a + b/lnx + c/(lnx)^2 + d/(lnx)^3 + e/(lnx)^4 \tag{4.5}$$

The multistep method was applied at iteration five by fitting Equation 4.5 using values at each iteration up to and including the fifth iteration. Table 4.2 shows that in two cases, the multistep method improves on the next estimate while in the third, the estimate was poorer. Besides illustrating the method in an application of a common iterative method, it shows that the approach relies on a good fit to the data to determine the limit and this requires sufficient data. In the Jacobi method, the solution is quickly reached and so the multistep approach is not as appropriate.

4.4 Algorithm of Wexler Modified with the Novel Multistep Approach

The response of the algorithm of Wexler is illustrated in the synthetic result of Figure 4.1 where three degrees of freedom have been shown. Each is a node in the finite element mesh

used in solving the field equations. They are representive of the responses in a region of background, a contrasting high, and a contrasting low.

To obtain the characteristic equation for the algorithm of Wexler, the response over the course of the processing was fit using the software package TableCurve [75]. This selected the equation

$$a_0 + a_1/sqrt(x) + a_2/(x)^{3/2} + a_3 log(x)/x^2 \tag{4.6}$$

as the best fitted to the data. This meets the necessary condition of having a finite value in the limit as the iteration number goes to ∞.

4.4.1 Tests with Synthetic Data

To test the performance of the algorithm of Wexler modified in this manner, data were generated with synthetic models and then recovered. Standardize testing of quality for imaging was first developed to consider the size and contrast of objects in the image and resolution from background and noise [73]. More recently, computerized tomographic performance phantoms have been formulated as industry-wide standards. For this study, tests were modified from standard tests to be used with other nonstandard tests. Modifications were used because, as was observed early in the test and as is consistent with observations of others [25], ERT methods do not perform well with complex images. This effect is illustrated in Figure 4.2 where there are five significant objects, of subtle, contrasting variations, dominating the conductance distribution. Figure 4.3 is another case where linear features of different widths and orientations have been used. Certain calculations can give an estimate of the resolution of a method, such as the modulation transfer function [30]. However, for the purpose of this dissertation, Equations 2.16 and 2.17 were used to provide a measure of the quality of the result.

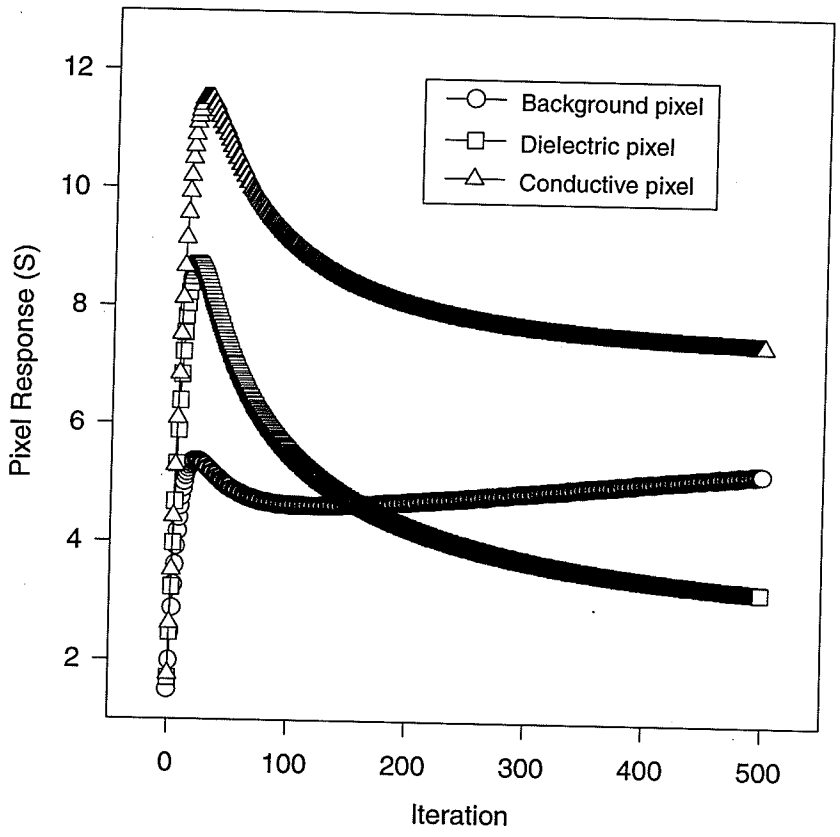

Figure 4.1: Response of degrees of freedom. In terms of the recovered admittance, each degree of freedom is a pixel value and a value at a node on the finite element mesh.

4.4.1.1 Two-dimensional Test Results

In this section, results from tests run with data generated from synthetic models in two dimensions are presented.

A Square Object: A test was performed using an object with a conductance of twice background. The object was a square of dimension five on a 17×17 grid. The result is shown in Figure 4.4 with the error response in Figure 4.5. The modified update was applied at iteration thirty and the process converged within the next three iterations based on the least-squares value computed by Equation 2.16. The result in this case shows the processing continuing at an accelerated level to convergence for several steps after the modified update strategy had been applied.

A Simple Spike: A simple spike with contrast of twice background was recovered from a homogeneous initial conductance at the background level. Figure 4.6 shows the result and compares it with the model. Figure 4.7 shows the error. The modified update can lead to a poorer intermediate error before subsequent improvements demonstrate the benefit of the method.

Two Objects of High and Low Contrasts: Two objects, with contrasts of twice background and half background, respectively, were recovered using a homogeneous initial conductance equal to background. Figure 4.8 compares the result with the original model.

A Small Object on a Fine Grid: Figure 4.9 shows a small object with a contrast of twice background, recovered on a fine grid. The three-unit wide target was recovered using a mesh fifty-one units wide. The processing ran for thirty iterations with the modified update strategy applied at iterations fifteen and thirty. A homogeneous initial conductance at background level was used.

Two Objects on a Fine Grid: Two small objects with contrast of twice background, were recovered in a homogeneous background. Figure 4.10 displays the result. Each target was three units wide and was recovered using a mesh fifty-one units wide. The edge-to-edge

separation of the targets was six units. The processing ran for thirty iterations with the modified update strategy applied at fifteen and thirty. A homogeneous initial conductance, equal to the background, was used.

Multiple Objects of Varying Contrasts: A test was applied in which four objects of varying contrasts were recovered [66]. Contrasts were twice, three-times, four-times and five-times background. Figure 4.11 displays the resuls. The processing ran for thirty iterations with the modified update applied at iterations fifteen and thirty. Background was used for the initial conductance. Figure 4.12 shows the error response for the processing in Figure 4.11.

Different Characterisitic Equation: To understand the effect the particular characteristic equation has on the result, a different equation was tested. A equation that did not fit the data as well as Equation 4.6, based upon the χ^2 value as returned by TableCurve [75], was selected (0.99976 versus 0.99823 for Equation 4.6). This equation had the form:

$$a_0 + a_1 exp(-0.5 log(x/a_2)^2/a_3) \tag{4.7}$$

The error response while using Equations 4.6 and 4.7 is illustrated in Figure 4.14 where a homogeneous initial conductance of one was used. Figure 4.13 shows the result for two objects with contrasts of three and a third with a contrast of nine. The result displayed is computed immediately before the modified update was applied and immediately after it was applied, at iteration forty. This result shows that the trend in the processing has been best captured in the characteristic equation.

4.4.1.2 Three-dimensional Test Results

The multistep method of this dissertation was also implemented in three dimensions. In this section, results from tests run with data generated from synthetic models in three dimensions are discussed. To illustrate the error function in three dimensions, the following cases were tested.

Simple Cube: A simple three-dimensional cube was recovered. The region of contrast was a two unit cube placed in an $8 \times 8 \times 4$ grid. Figure 4.15 shows the result and Figure 4.16 shows the error function. The target had an amplitude of twice the background and was processed for ten iterations with the modified update strategy applied every fifth iteration. Processing was halted because convergence was reached. A homogeneous initial conductance, equal to the background, was used. In a similar case a single object $5 \times 5 \times 2$ with a contrast of twice background was recovered (see Figure 4.17).

Two Objects of Different Contrasts: Figure 4.18 is an example where two objects of different contrasts were recovered. Figure 4.19 shows the error function. The targets were three and two times background, respectively, and processed for fifteen iterations with the modified update strategy applied at the fifth and tenth iterations. Processing was halted because convergence was reached. A homogeneous initial conductance, equal to the background, was used.

4.4.2 Result from Field Data

Figure 4.20 is a plot of error for field data from a survey presented later in this dissertation, as part of Chapter 6. The error for the cases with and without the multistep method are compared. The multistep process is applied at a five iterations interval. After twenty-five iterations, the image has reached its asymptotic limit: the value reached by the unmodified algorithm after 673 iterations. The field data responds better than the synthetic case when using the multistep approach. This is best explained by the high contrast between the metal target and the sand background, as was in the case of this data.

4.4.3 The Effect of Filters

A cross-median filter [37] was tested in combination with multistep processing. The modified update strategy was applied at five step intervals over sixteen iterations. Figure 4.21 shows how filtering can apparently improve the resultant conductance, although the error function indicates poorer performance. Figure 4.22 shows the error function. The first and

second applications both improved the image even though the error trends upwards between applications of the modified update strategy. The error function continues to degrade and further modifications to the update causes the result to deteriorate further.

The filtering removes local spikes but causes poorer overall performance. Figure 4.22 also shows that the multistep method, when used in combination with filtering, is adversely affected. Filtering causes the limit value to be dependent on an average computed from neighbour pixel values, thereby altering the characteristic response of the algorithm.

4.4.4 Benchmark Results

A case in two dimensions with 81 degrees of freedom, and a case with 405 degrees of freedom in three dimensions, were run on a μVAX 3100[3]. Table 4.3 compares the elapsed time for computing a single iteration. (Other results have been tabulated [65].) These results were generated using the frontal method [31, 45, 77]. The signficant increase in computation time for the three-dimensional case is due to the wider band-width of the stiffness matrix that results from the geometry of the mesh [77]. More terms are carried in the frontal matrix and this results in poorer performance. In the two-dimensional case, the band is dense and narrower. They show that the multistep method does not contribute to the processing time in any significant way while the rate of convergence is dramatically improved.

4.5 Discussion and Conclusions

The multistep method presented was successfully applied to the algorithm of Wexler with two- and three-dimensional synthetic and field data. The method is distinct from other multistep methods in that it exploits the response characteristic of the processing technique. This characteristic equation is extrapolated to the limit as the number of iterations goes to ∞ to improve the update. Without enhancement, the algorithm of Wexler often requires thousands of iterations to converge. This is a significant problem since two time-consuming matrix inversions are performed during each iteration. With only a negligible increase in

[3]Digital Equipment of Canada, Winnipeg MB.

Table 4.3: Benchmark comparisons. The times needed to process a single iteration on a μ-VAX 3100. Cases in two dimensions and three dimensions were tested. Five values were used for the modified update.

Dimension	Approach	Geometry	Degrees of freedom	Band width	Time for one iteration (seconds)
2	Wexler	9×9	81	25	0.0500
	Modified Wexler	9×9	81	25	0.0500
3	Wexler	$9 \times 9 \times 5$	405	182	55.19
	Modified Wexler	$9 \times 9 \times 5$	405	182	55.64

computational time at an iteration, the method improved the rate of acceleration by up to two orders of magnitude. In cases, the quality of the result was improved over the unmodified algorithm.

It has two advantages over multistep methods using calculations of differences. First, a general representation is a poor fit with low-orders where large accelerations are present. To achieve the high-order fit, many data points are needed. However, computation of differences limit accuracy because of roundoff error that increases with the number of points. This is not the case for this approach because additional information improves the fit (see Figure 4.14).

The multistep method does not overcome any other fundamental shortcomings of the algorithm. When the complexity in the conductance increases, the results tend to degrade as can been seen by comparisons with Figures 4.9 and 4.11. Figure 4.10 suggests the resolution of small objects appears to be about three parts in a hundred at a center-to-center separation of nine radii.

Outside of this dissertation, this improvement can have a significant impact in medical applications of ERT methods where significant advances could led to real-time monitoring.

The approach has been used for the results of Chapter 6.

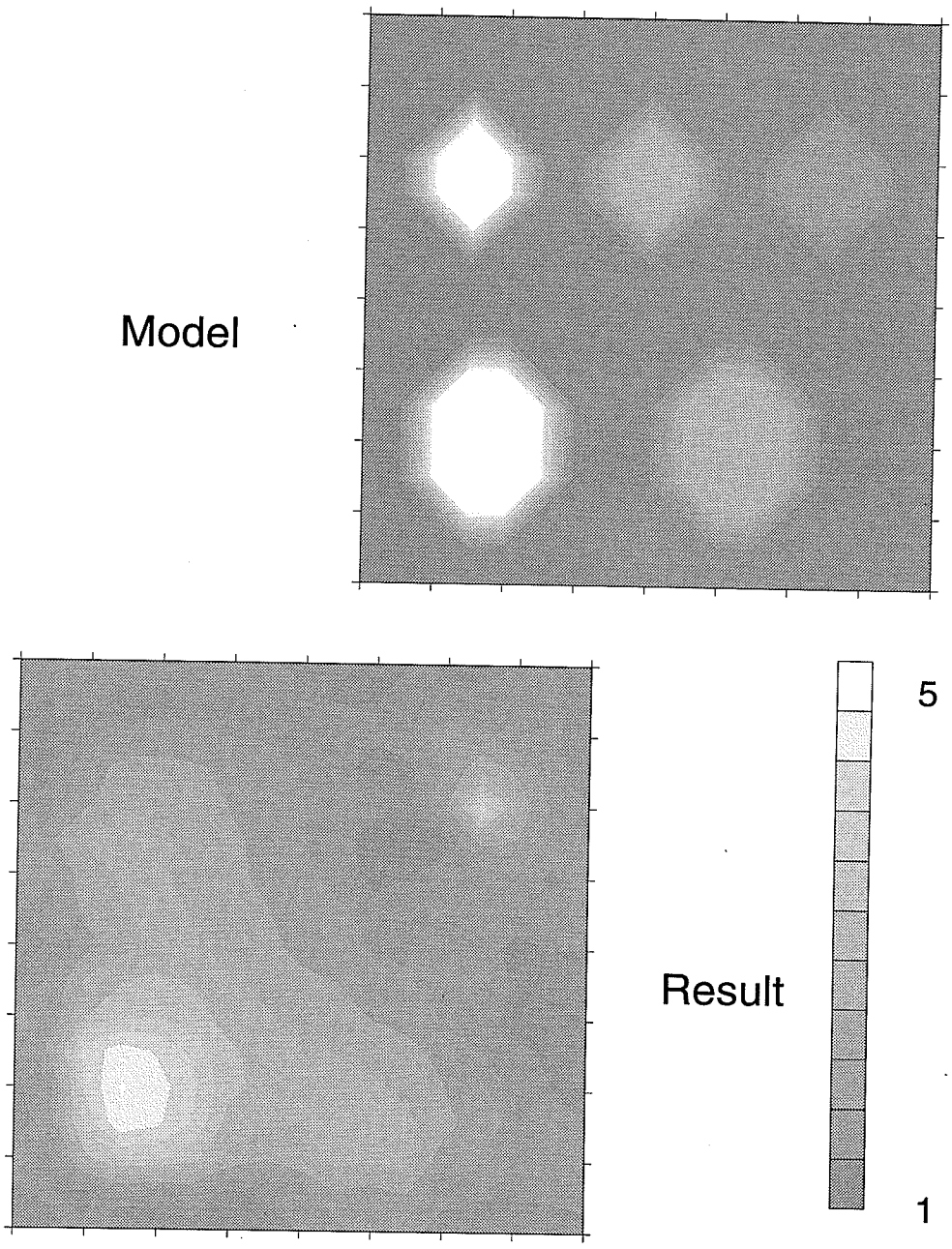

Figure 4.2: Poor resolution of complex distributions (I). A relatively complex distribution, of subtle contrast variations, is used to demonstrate the poor resolution of the ERT method in these circumstances. The processing ran for 150 iterations. The solution used a homogeneous initial conductance, equal to the background. This test is based on a standard test in [73]. Objects are not resolved in cases and the amplitudes are not properly recovered: even in correct relative proportions.

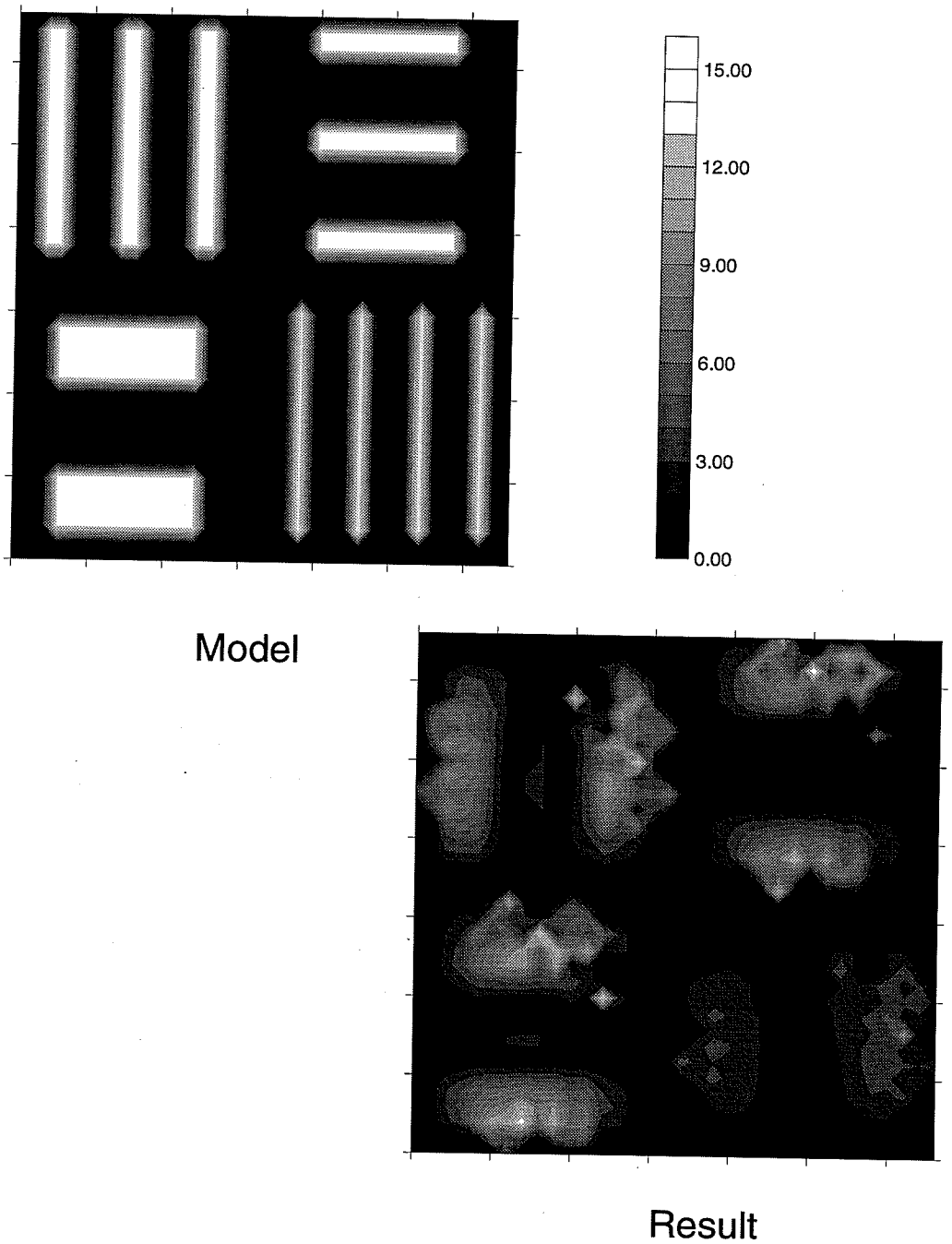

Figure 4.3: Poor resolution of complex distributions (II). A relatively complex distribution, of subtle contrast variations, is used to demonstrate the poor resolution of the ERT method in these circumstances. The processing ran for 150 iterations. The solution used a homogeneous initial conductance, equal to the background. This test is based on a standard test in [73].

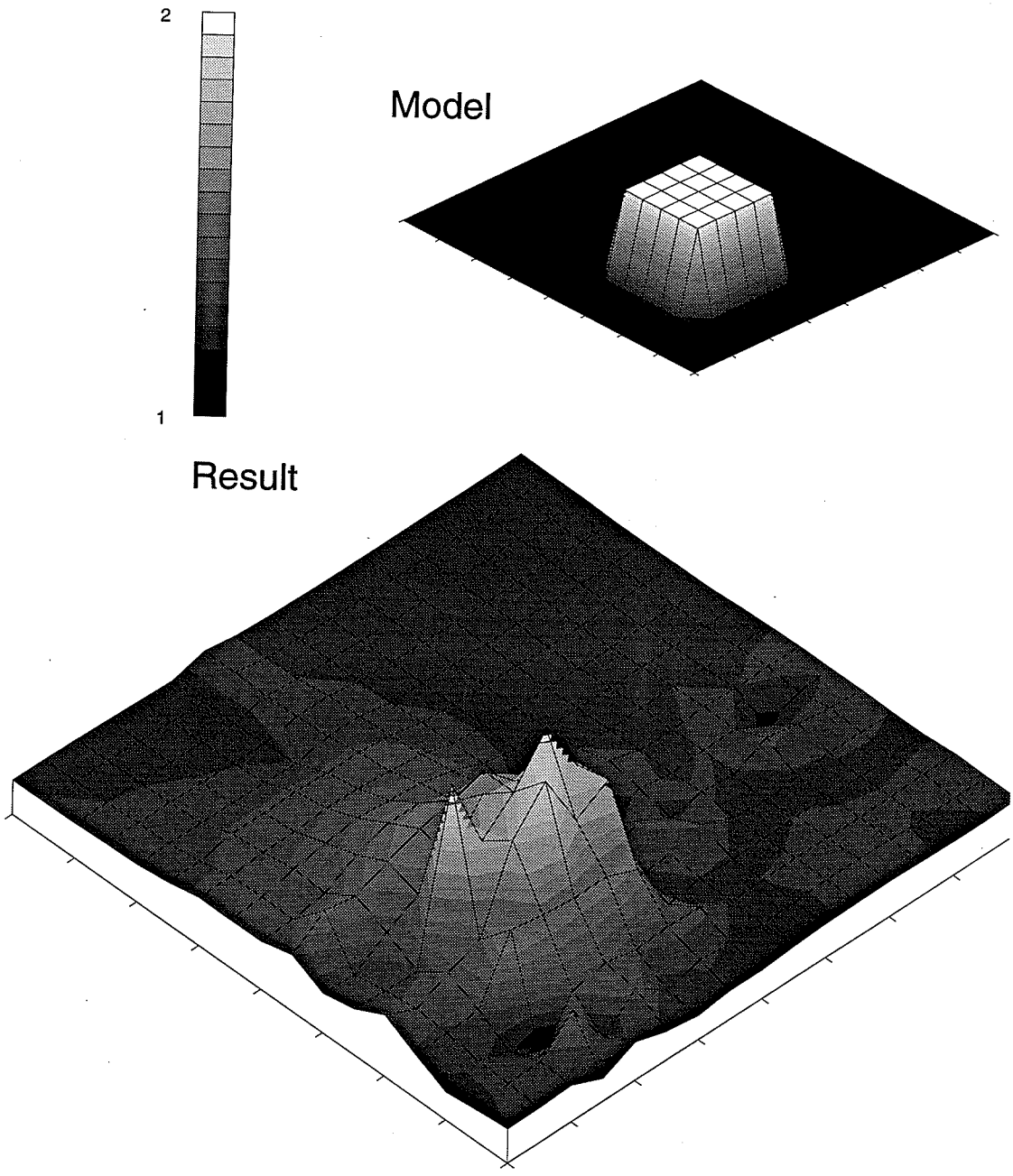

Figure 4.4: A simple case for the multistep method. A 5 x 5 square of contrast of twice background was recovered on a mesh 17 x 17. The processing was performed for thirty-five iterations with the modified update strategy applied at iteration thirty. The initial conductance was homogeneous at background level. The error response is included in Figure 4.5.

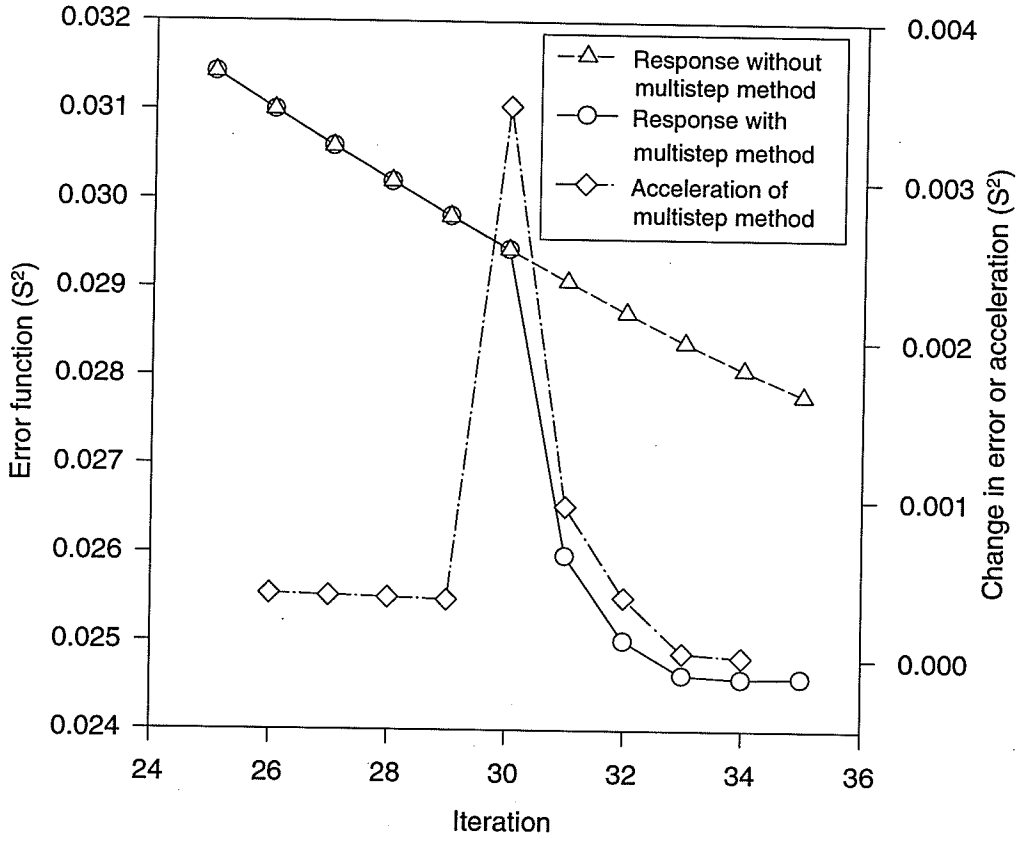

Figure 4.5: Error for the simple case. The error function during the processing of Figure 4.4.

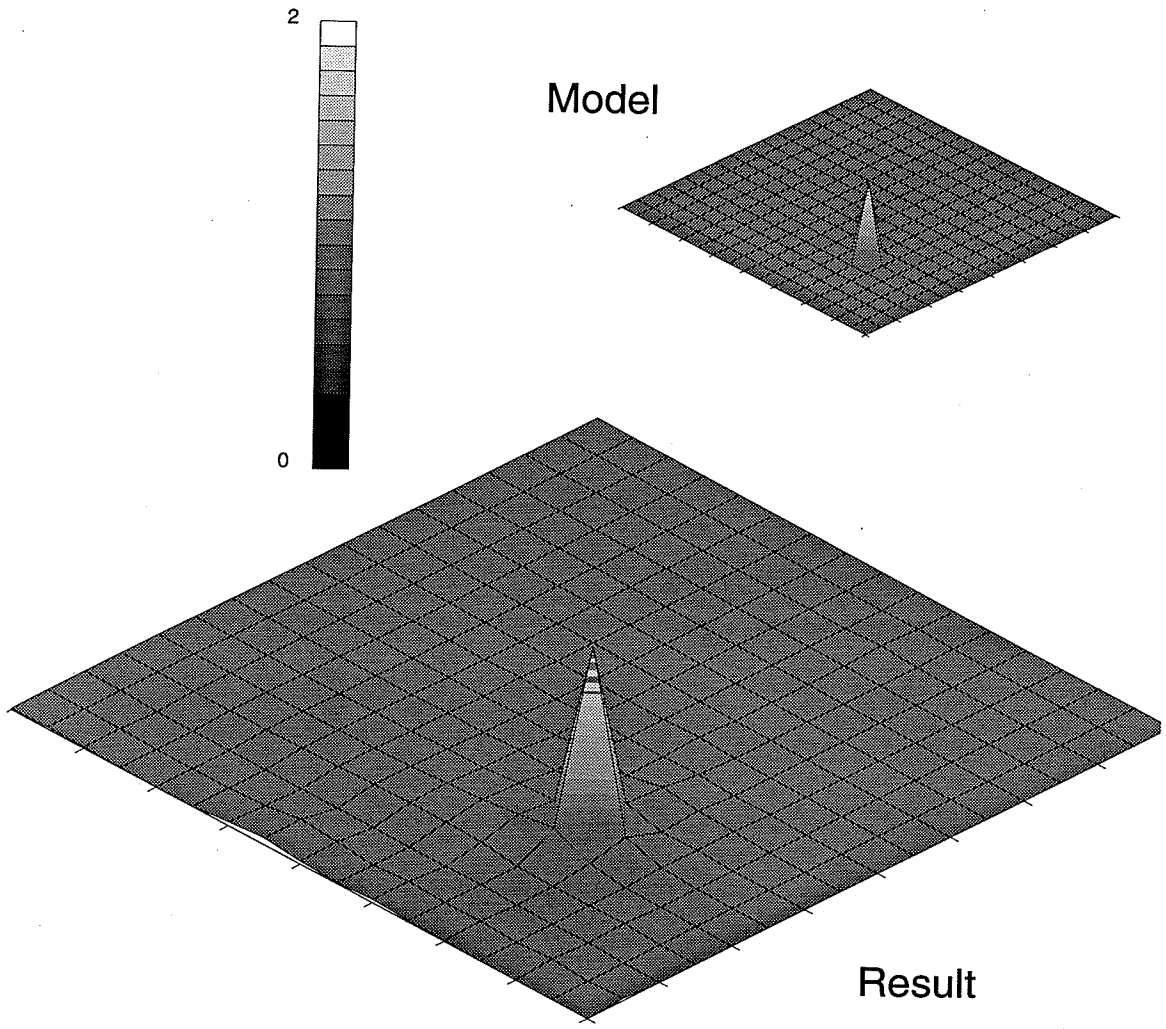

Figure 4.6: The multistep method and spike. A one-unit wide target was recovered using a mesh seventeen units wide. The target was twice background. The processing ran for fifteen iterations with the modified update strategy applied at iterations five and ten.

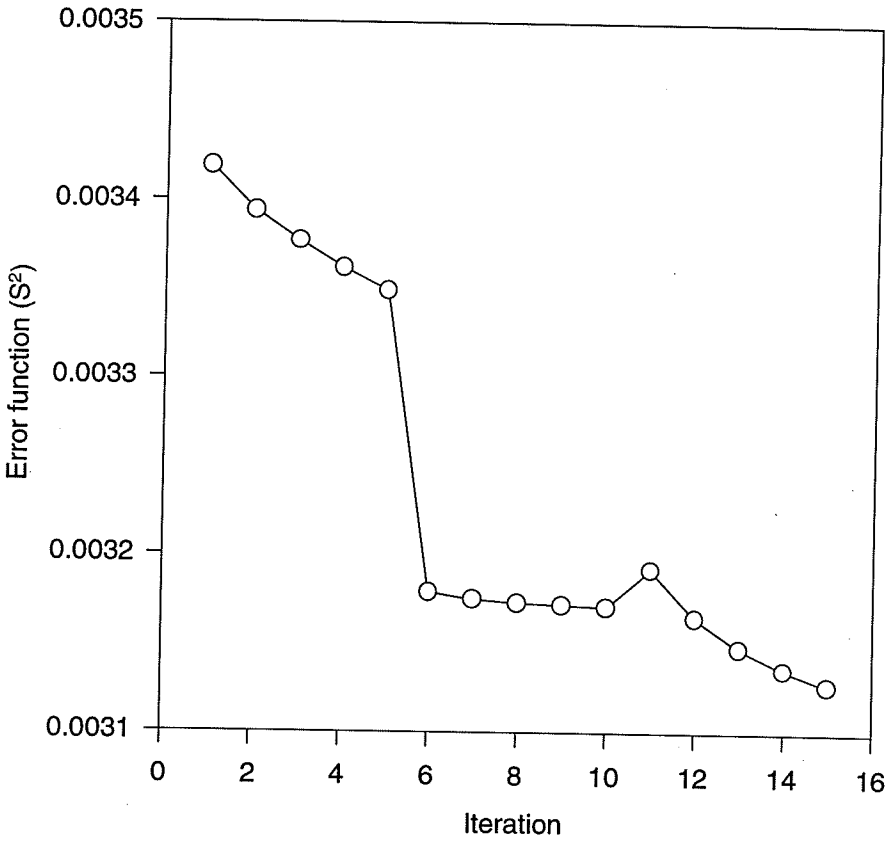

Figure 4.7: Error for the spike. The error response for Figure 4.6.

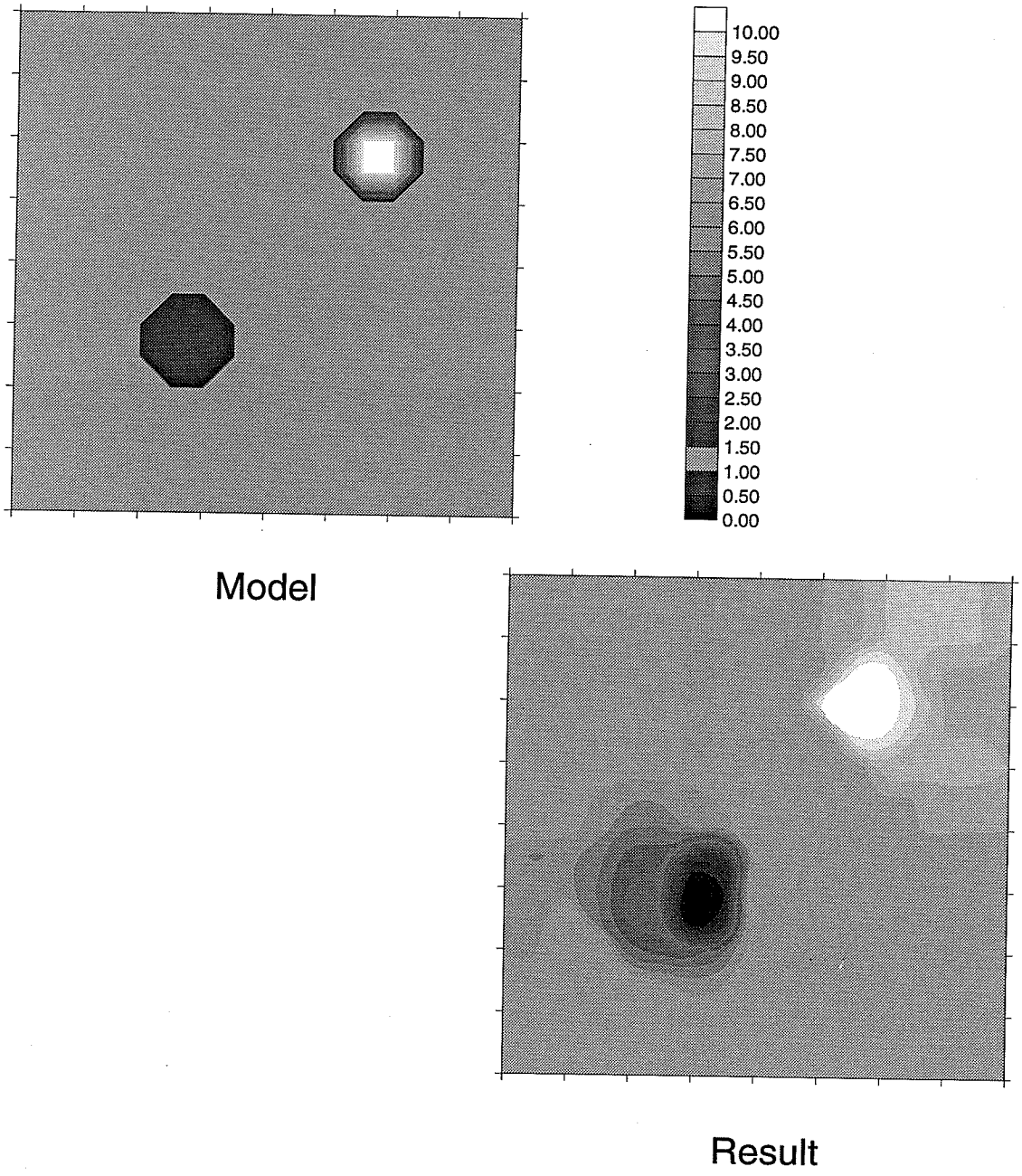

Figure 4.8: The multistep method with high and lows. Two two-unit wide targets were recovered using a mesh seventeen units wide. The target-background-target conductances were one-half–one–ten, respectively. The processing ran for thirty iterations with the modified update strategy applied at fifteen and thirty. A homogeneous initial conductance, equal to the background, was used.

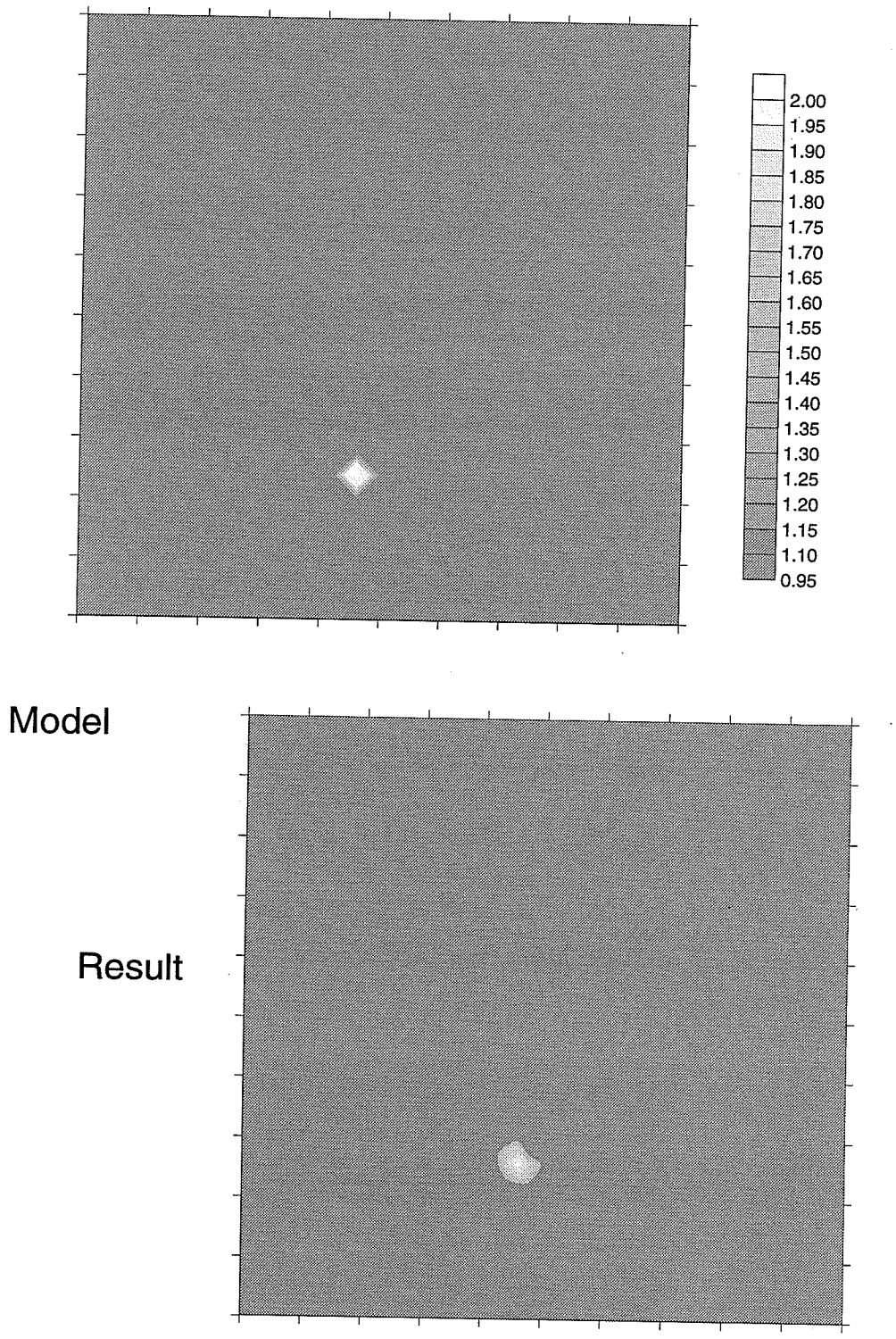

Figure 4.9: A simple object and the multistep method. A three-unit wide target was recovered using a mesh fifty-one units wide. The target was twice background. The processing ran for thirty iterations with the modified update strategy applied at fifteen and thirty. A homogeneous initial conductance, equal to the background, was used.

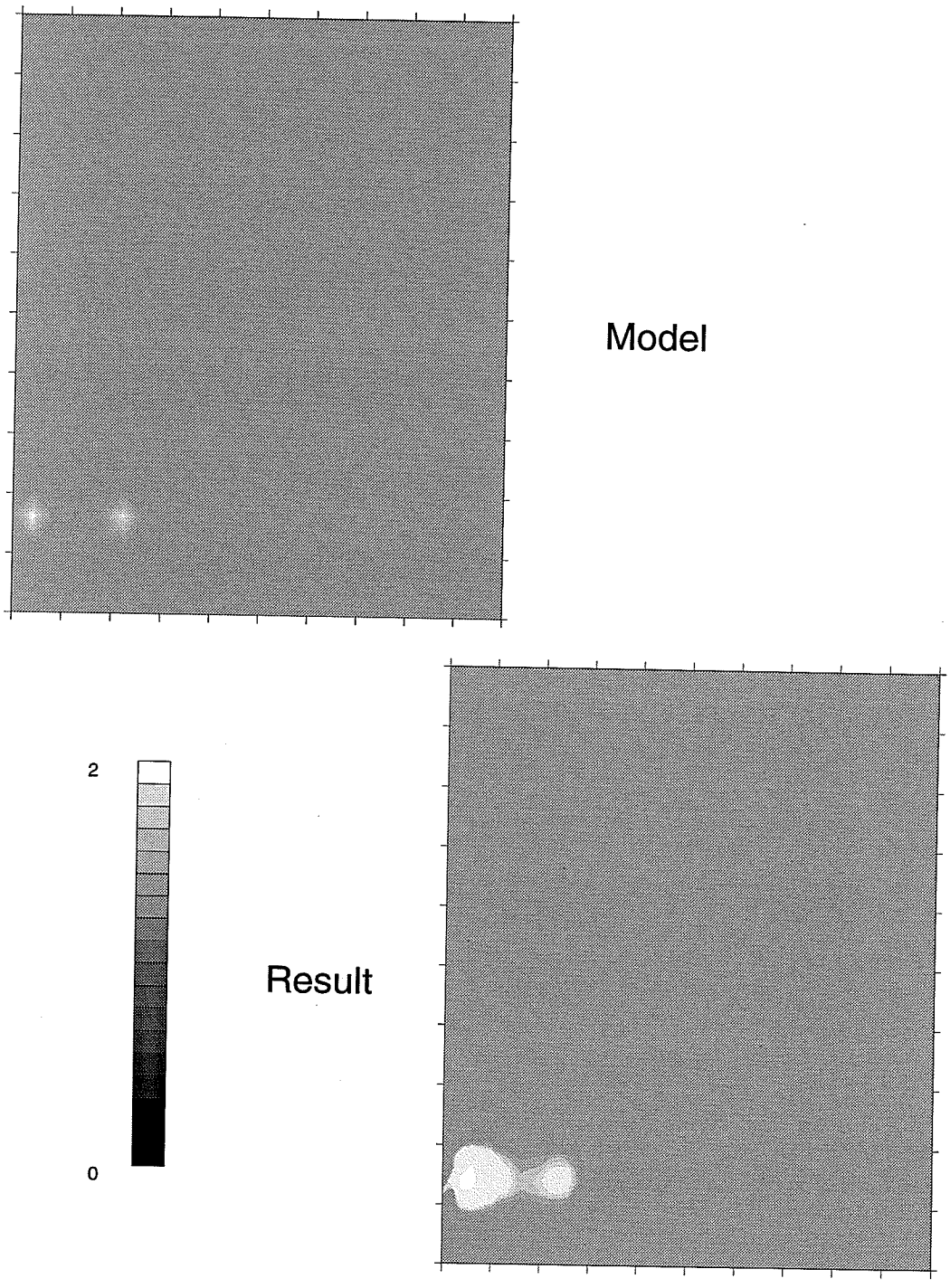

Figure 4.10: Two objects and the multistep method. Each target was three-units wide and were recovered using a mesh fifty-one units wide. The edge-to-edge separation of the targets was six units. The processing ran for thirty iterations with the modified update strategy applied at fifteen and thirty. A homogeneous initial conductance, equal to the background, was used.

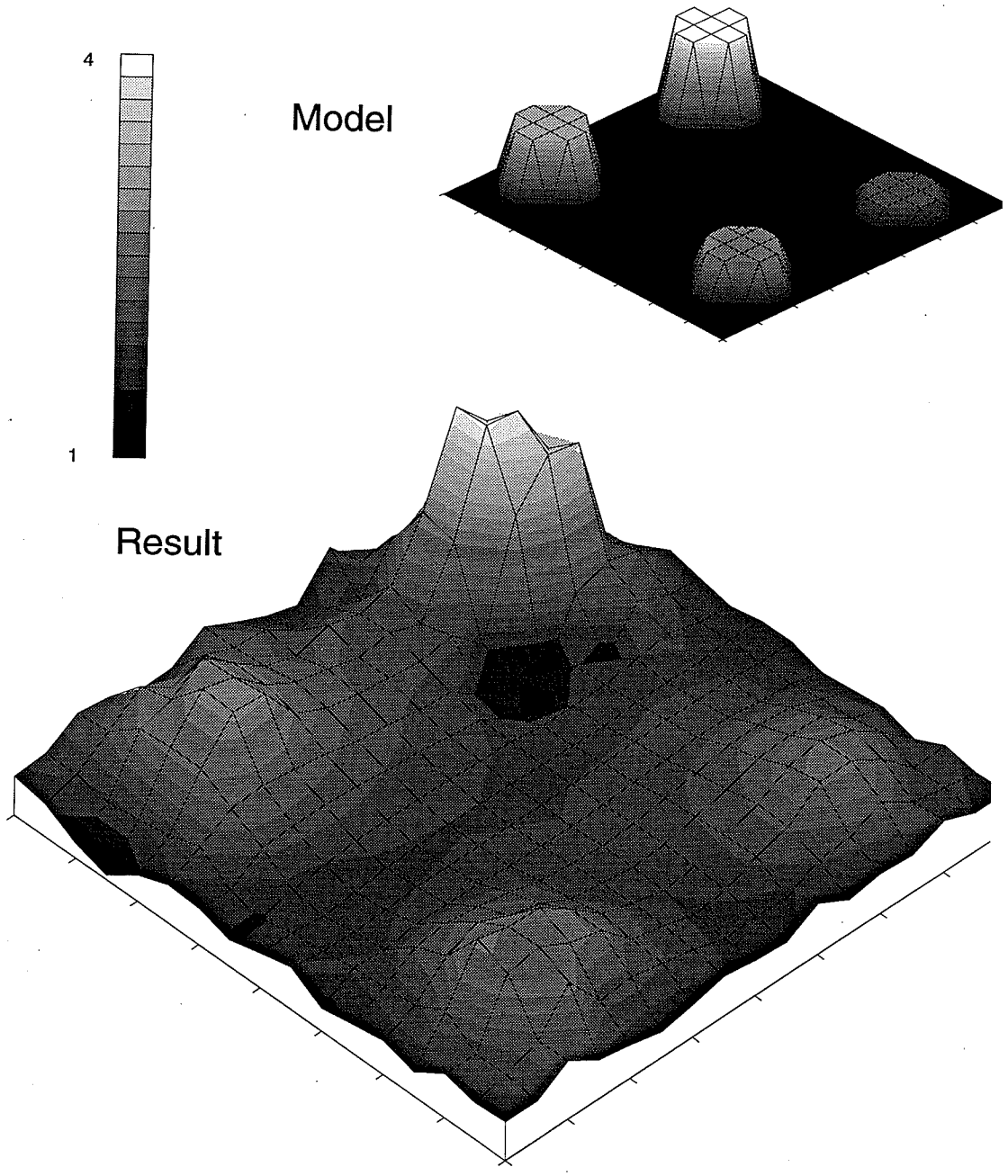

Figure 4.11: Multiple objects and varying contrasts. Contrasts of twice, three-times, four-times and five-times background were recovered. The processing ran for thirty iterations with the modified update applied at iteration fifteen. The solution used a homogeneous initial conductance, equal to the background.

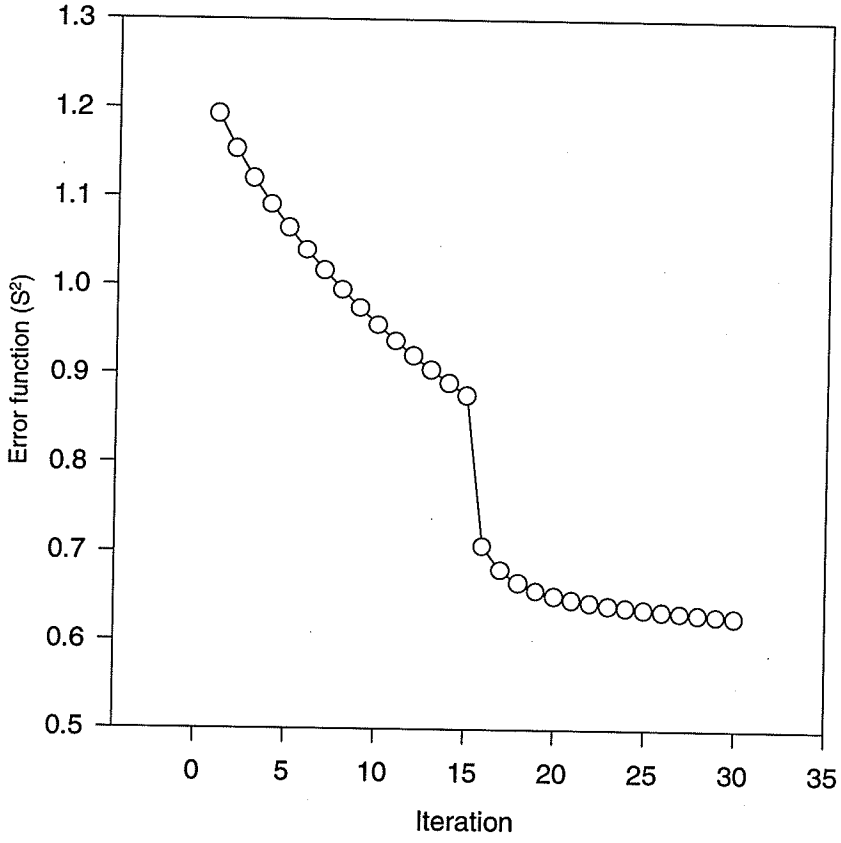

Figure 4.12: Error for multiple objects. Error for processing displayed in Figure 4.11. The processing ran for thirty iterations with the modified update applied at fifteen.

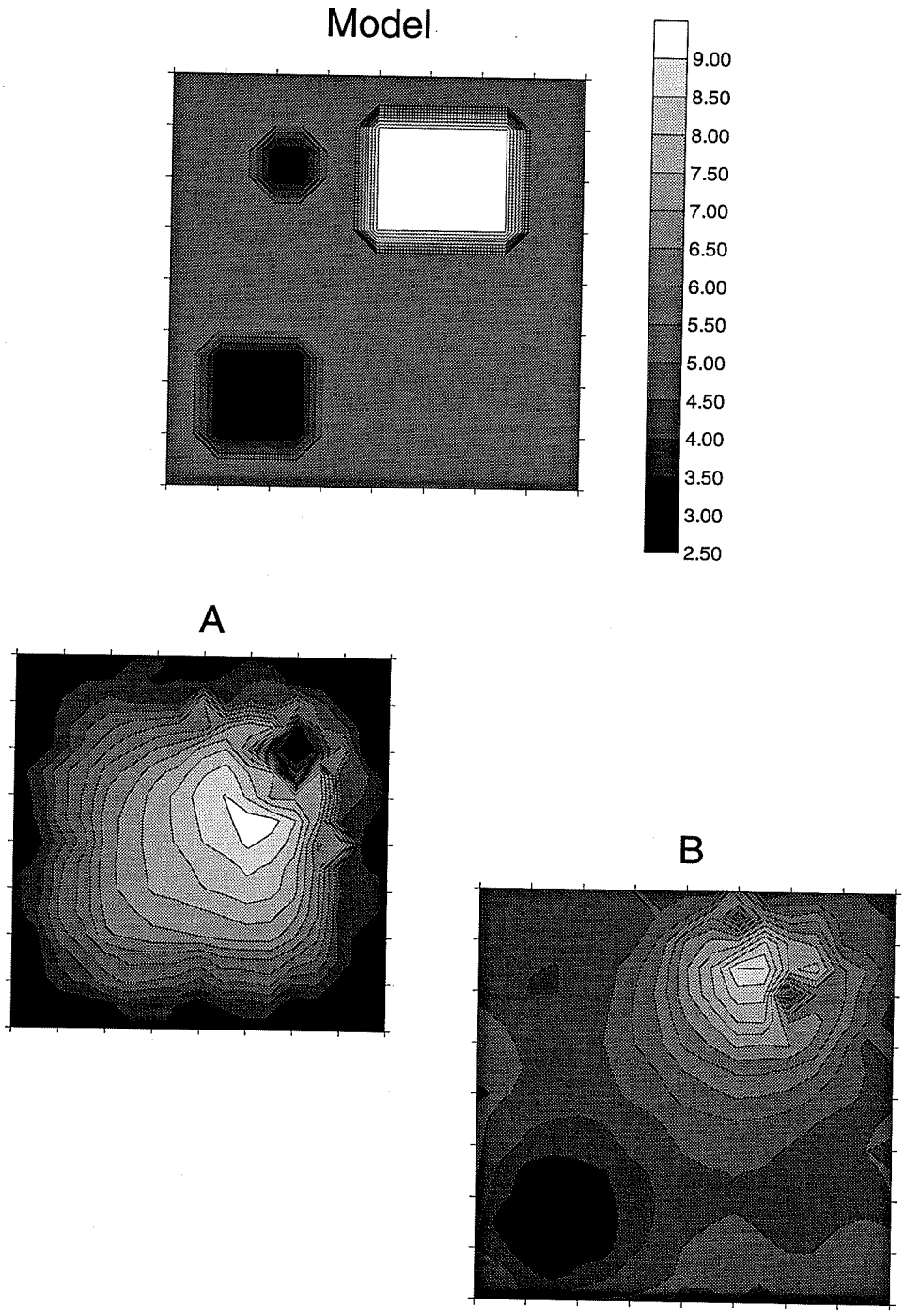

Figure 4.13: Three objects and the multistep method. Illustrated is the model used in the synthetic test and the result: immediately before the modified update strategy was applied at iteration forty Figure 4.13A, and immediately after it was applied Figure 4.13B. The error function is shown in Figure 4.14.

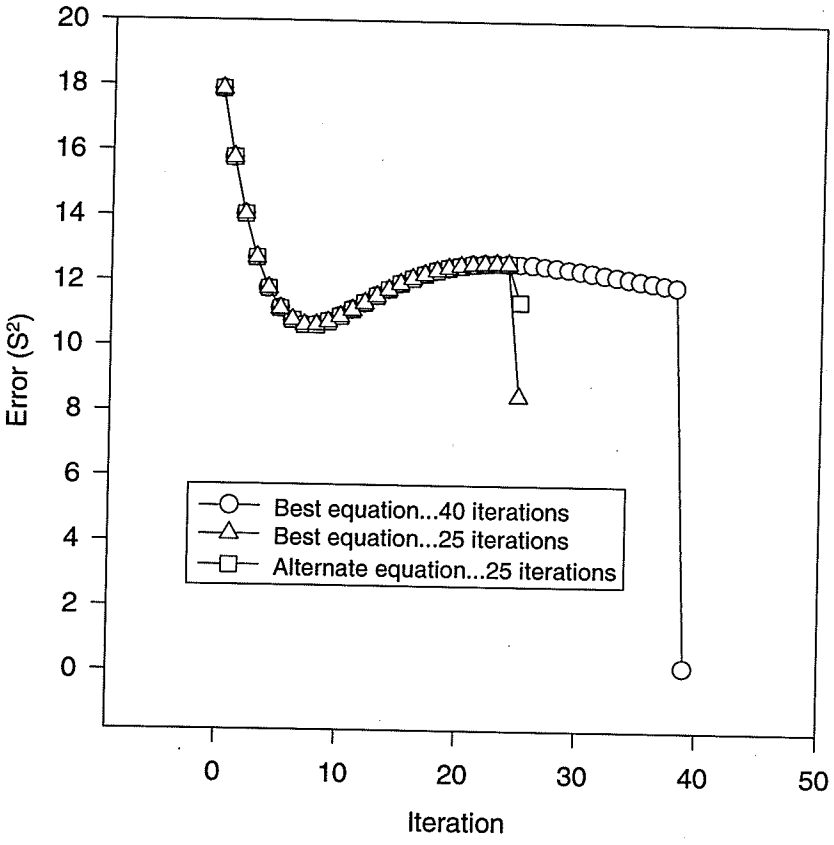

Figure 4.14: Modified update using different equations. In this figure, a homogeneous initial conductance of one was used in recovering three contrasting regions in a background of five. Different numbers of points were used to illustrate the effect on the quality of the fit. The images are shown in Figure 4.13.

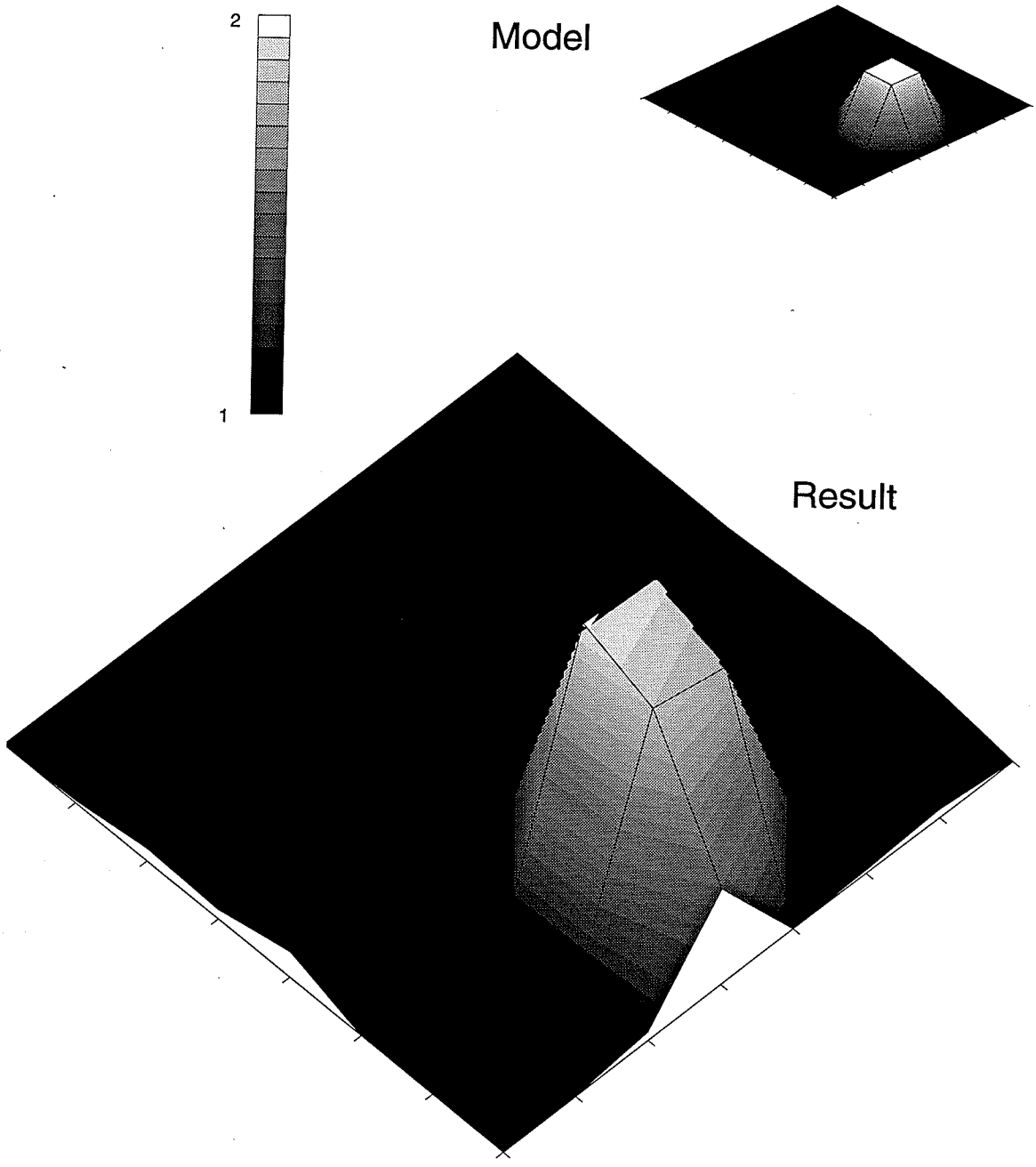

Figure 4.15: Three dimensions and the multistep method. A target in three dimensions is shown with the second horizontal section illustrated. A $2 \times 2 \times 2$ target was recovered using a mesh $8 \times 8 \times 4$. The target was twice background. The processing ran for ten iterations with the modified update strategy applied every fifth iteration. A homogeneous initial conductance, equal to the background, was used. Processing was halted because the processing converged.

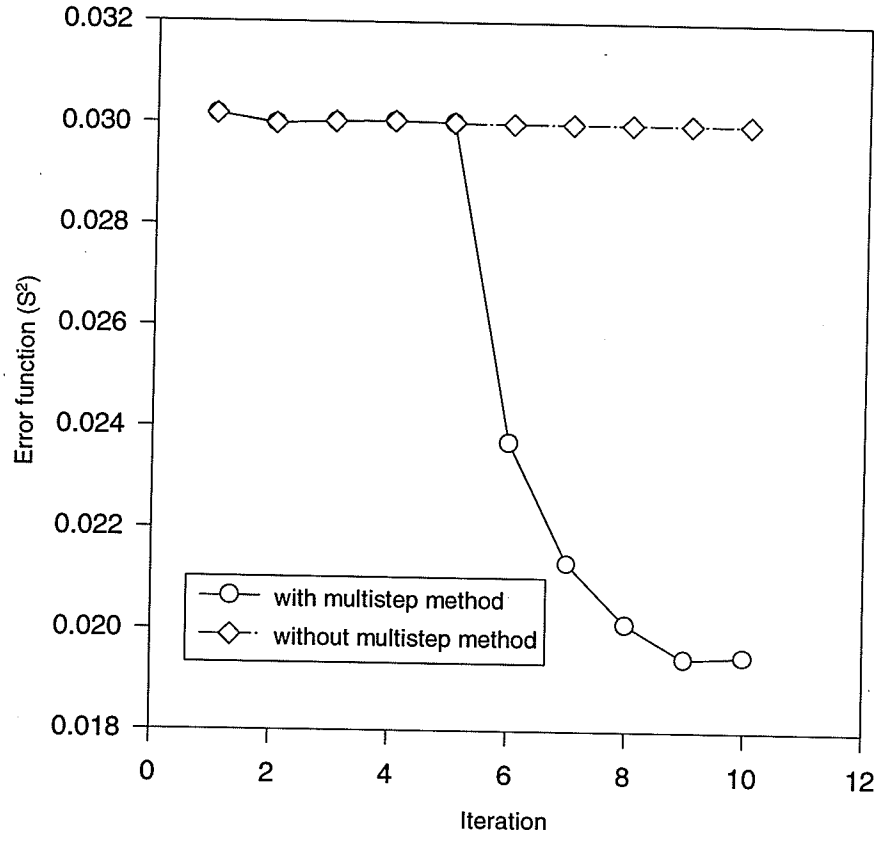

Figure 4.16: Error for three dimension. This is the response shown for the case described in Figure 4.15.

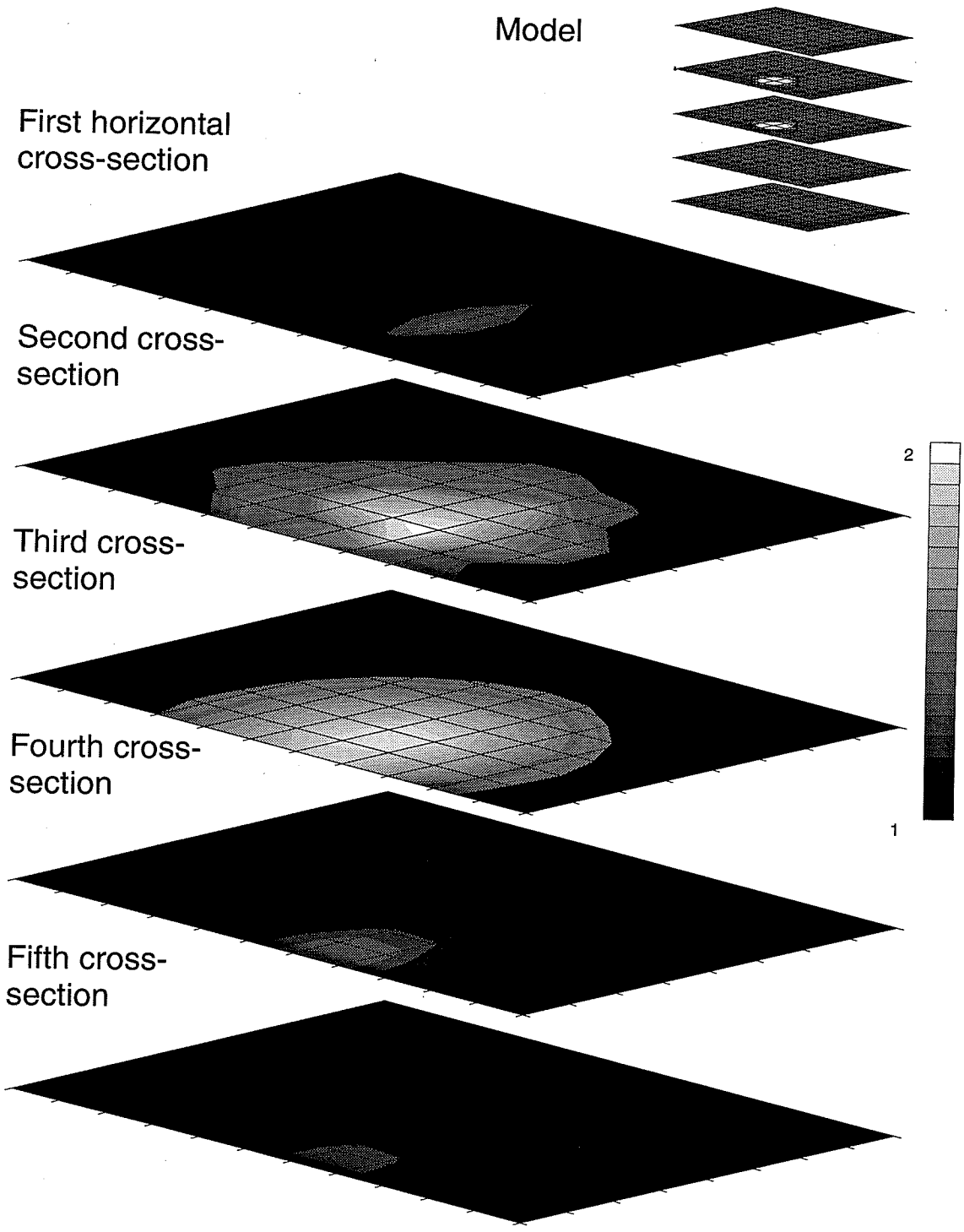

Figure 4.17: A case in three dimensions. A $5 \times 5 \times 2$ target was recovered using a mesh $9 \times 12 \times 5$. The target was twice background. The processing ran for thirty-five iterations with the modified update strategy applied at thirty-five. A homogeneous initial conductance, equal to the background, was used.

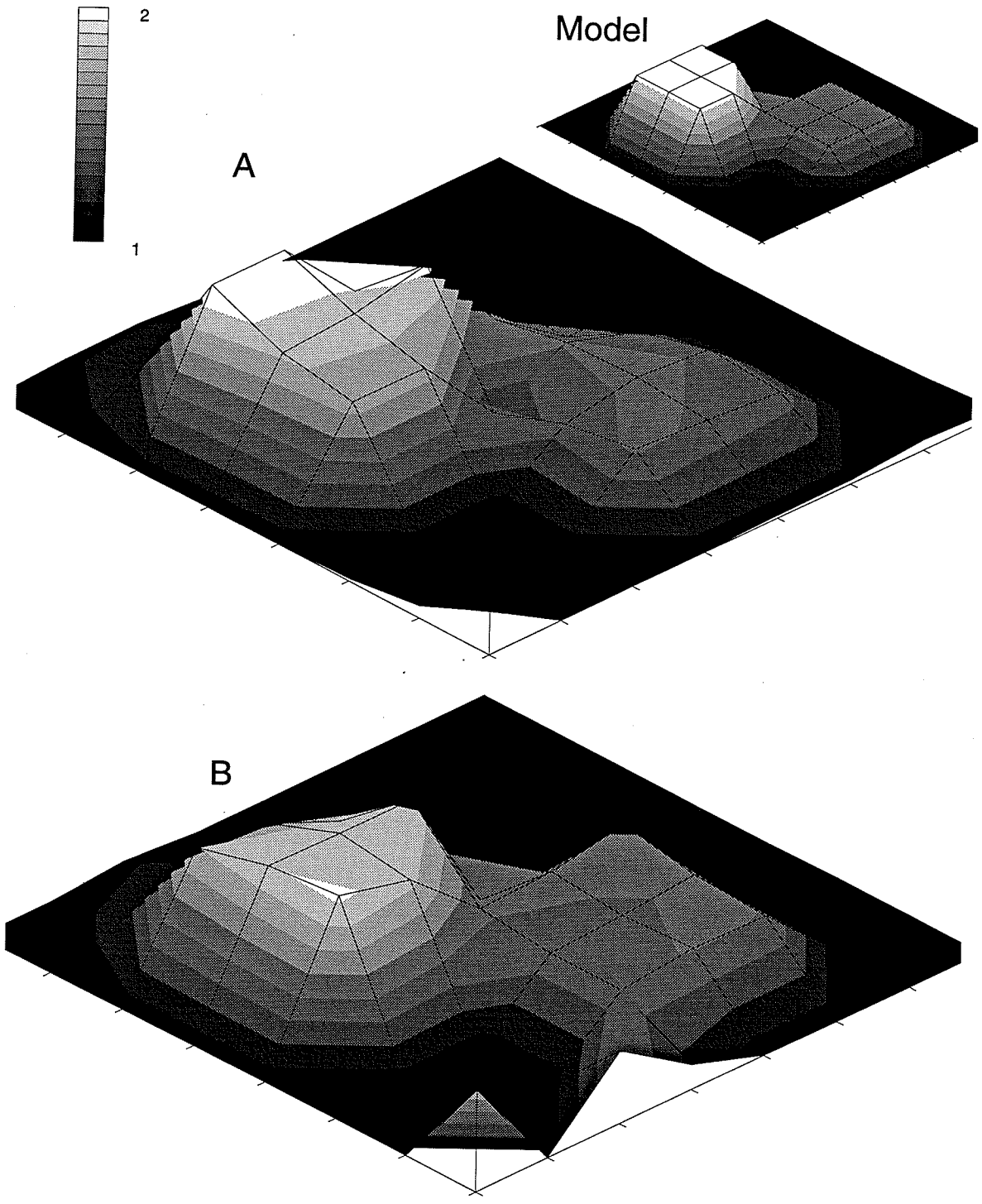

Figure 4.18: Two targets in three dimensions. Only the two horizontal cross-sections are shown. The model shows the data for the second (Figure 4.18A) and third horizontal cross-section (Figure 4.18A): the first and fourth horizontal have no significant values and are not shown. The error is shown in Figure 4.19.

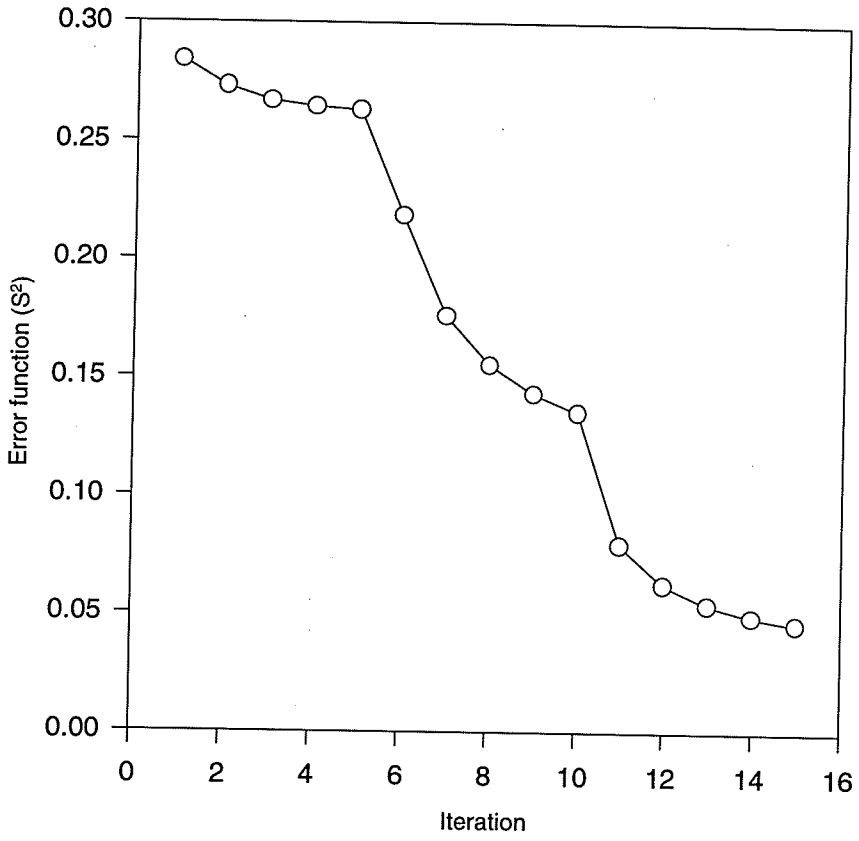

Figure 4.19: Error for two targets. This is the result for the model in Figure 4.18.

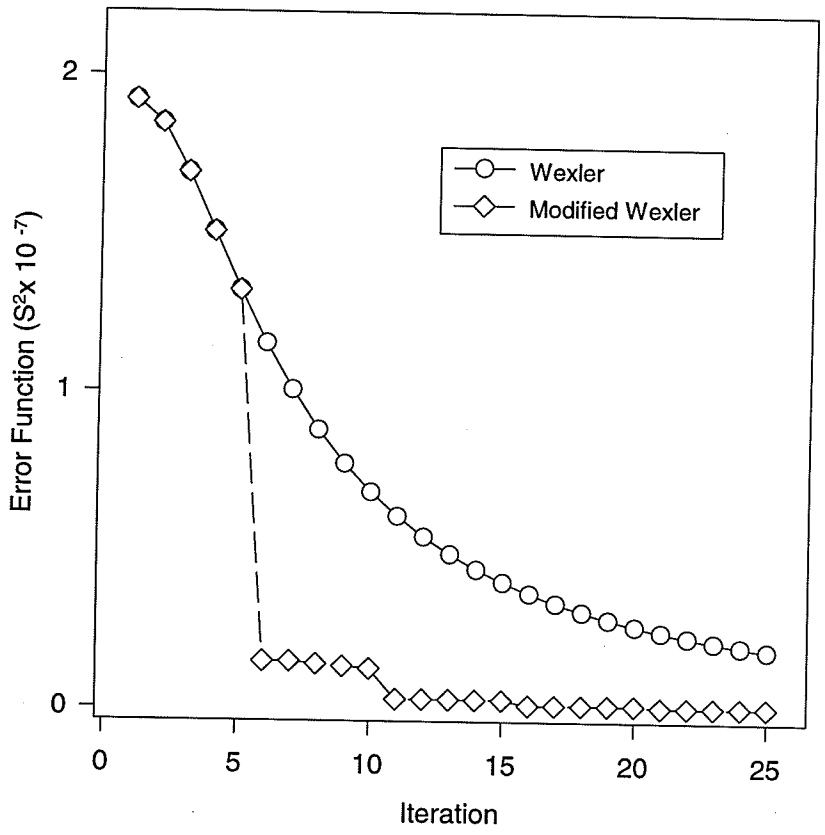

Figure 4.20: Result using field data. Data were from field measurements where a metal barrel was buried in sand and measurements were made from surface. The unmodified algorithm reached $.0073\times10^{-7}S^2$ after 673 iterations, the same error reached by the modified algorithm after 25 iterations.

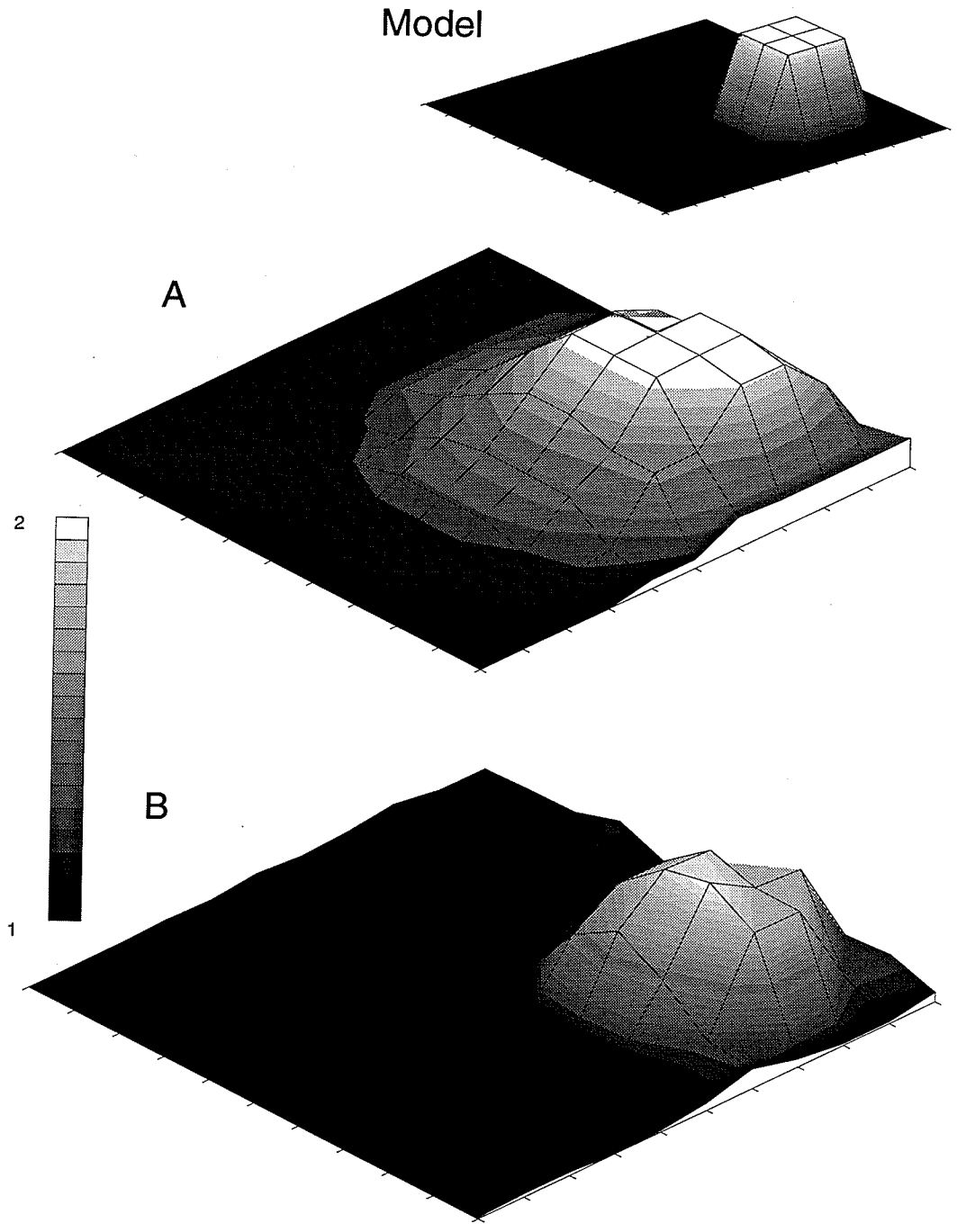

Figure 4.21: The effect of filtering. Tests were run with cross-median filtering applied at each iteration. The model is shown as the top image. Figure 4.21A shows the result with a cross-median filter applied at each iteration. Figure 4.21B shows the result when filtering was applied only on the final iteration. The error response is shown in Figure 4.22.

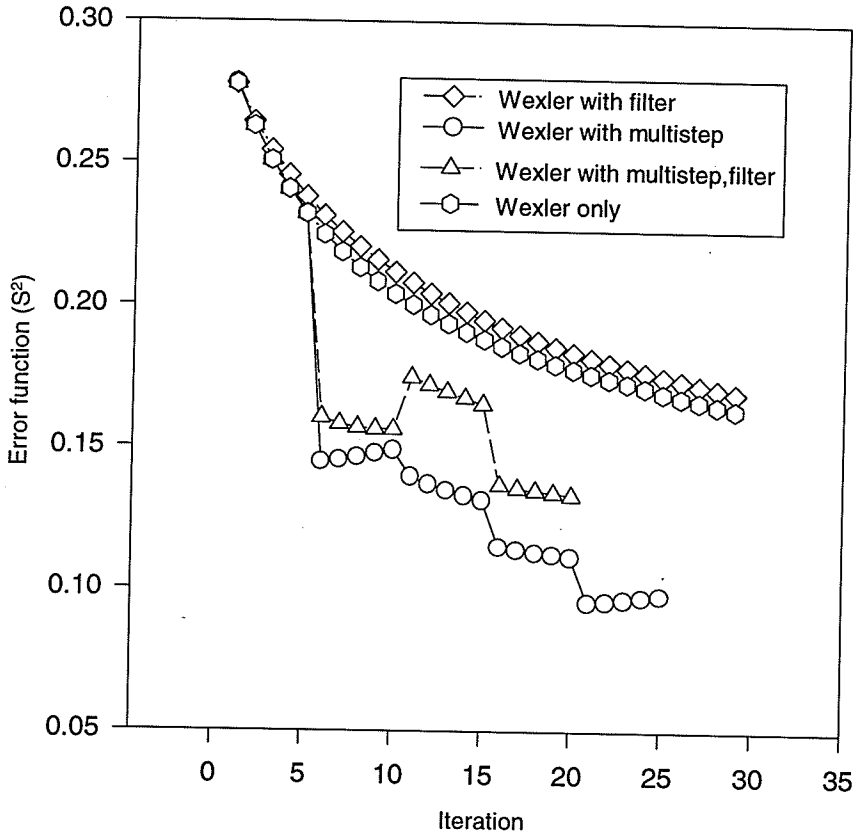

Figure 4.22: Filtering with multistep. Tests were run with cross-median filtering applied at each iteration. The same case was run using filtering with the modified update strategy applied at five step intervals. This is for the case shown in Figure 4.21.

Chapter 5

Monitoring Moisture in a Soil Material

5.1 Overview

Previous tests demonstrated that the conductance of soil materials vary with amount of moisture [81]. Based on this finding, the test described in Chapter 5 was proposed to use an ERT method to monitor moisture flow in a soil-type barrier (buffer). The apparatus was a borehole packed with buffer with the saturated rock walls serving as the source for moisture in flow into the system. Electrodes were fastened to the rock wall. The monitoring was performed under isothermal conditions as a full-scale, *in situ* test at a depth of 240m below surface at the Underground Research Laboratory (URL), near Lac du Bonnet, Manitoba [76].

The work contributed to a larger research program—the Canadian Nuclear Fuel Waste Management Program (NFWMP)—aimed at developing a methodology (the Concept) for safe disposal of nuclear fuel waste. The proposed method for disposal would be to place containers of nuclear fuel waste in buffer in underground disposal vaults in plutonic rock of the Canadian Shield (Figure 5.1). The principal concern in the deep geological burial of the waste is the effect of groundwater on the vault and the resultant corrosion, dissolution, and outward transport of waste. In the NFWMP, groundwater movement will be restricted by multiple, independent barriers. Of the different barriers proposed, buffer is to be relied on most for the long term.

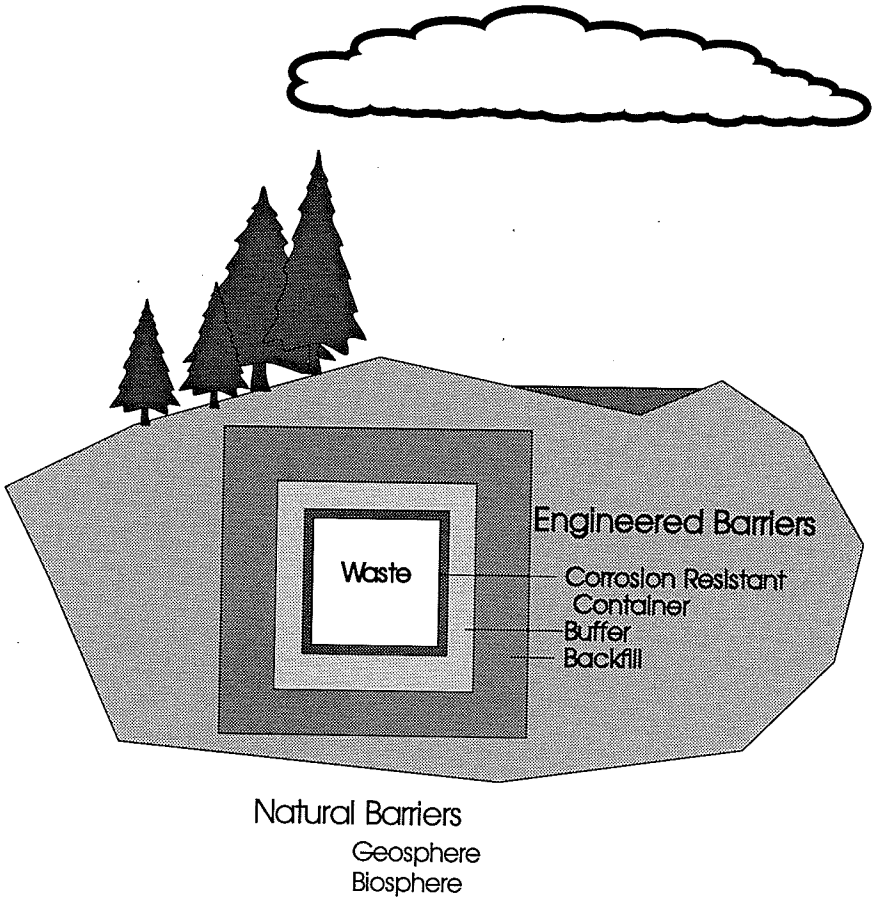

Figure 5.1: Barriers in a disposal vault. The barriers in the vault consist of both engineered and natural systems. The primary engineered barrier is the buffer material.

Considerable work was done incidental to the direct ERT component of the study. A data-acquisition system was built using a modular design that could be expanded by adding more units and excitation sources could be plugged in to adapt to different conditions. This was the system used in tests described in the chapters following. The electrical properties of buffer were studied to derive a moisture-conductance calibration curve. Independent psychrometer measurements and emplacement levels were used to derive quantitative results. It was found that internal redistribution of moisture was the most significant feature in contrast to what was expected due to in flow on the boundary.

5.1.1 Buffer Material

Buffer is composed of 50% Avonseal Bentonite (Na-) and 50% graded silica sand with a water content of 18%, devised as a standard for study in the NFWMP [28]. Bentonite is a chemically inert material composed of smectitic, sheet-like clay[1] particles of montmorillonite (> 50%) that causes it to expand when wet. Montmorillonite is a hydrated aluminosilicate mineral having weakly attached cations of Na^+ and Ca^{++}. Formation of these minerals is affected by isomorphous substitution [56], giving a net valance charge that dominates the electrical properties of the material. The reference density of the buffer is $1.67 Mg/m^3$ with a water content of 16% to 18% [106]. Many physical properties of bentonite make it an ideal material as a barrier to moisture movement. A most important property is that buffer swells when wetted giving it a self-healing nature that causes closing of desiccation fractures during rehydration. It absorbs solutes in water and this inhibits the transport of radio-nuclides [40].

5.2 Data-Acquisition System

The surveys described in this dissertation research were performed with the data-acquisition electronics and software designed as part of this study. The design makes use of previous work [83] and is more thoroughly described elsewhere [86, 87]. The measurements were taken sequentially using a high-precision meter and, though acceptable in environmental applications, the acquisition of data in this manner is slow.

5.2.1 Hardware

Figure 5.2 shows the data-acquisition hardware. The monitoring electronics consist of a set of Phillips electronic devices controlled by a personal computer manufactured and marketed by MIND Computers.[2] Communication was done with an IEEE-488 parallel bus to

[1] By definition, clay is a material composed of grains < 0.002mm.
[2] MIND Computers, Unit A 1745 Ellice Avenue, Winnipeg MB R3H 1A6, (204) 786-7747.

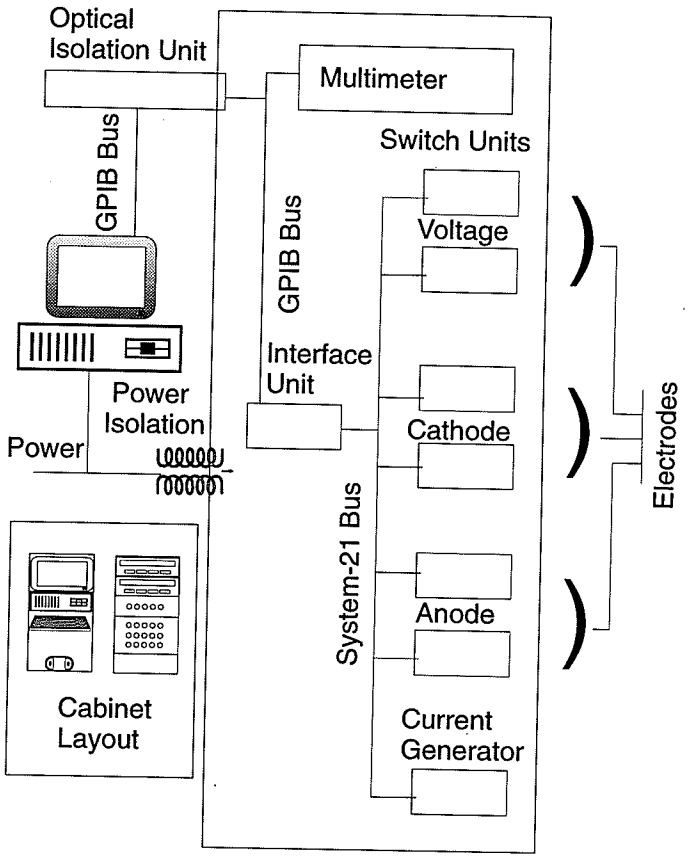

Figure 5.2: Data-acquisition hardware.

Fluke/Philips [3] proprietary System 21^{tm} units using a Philips GPIB Interface card installed on the computer. Fully functional, it could address up to 14 GPIB instruments and was hardware and software configured to select an appropriate IRQ setting, DMA channel, and base I/O address.

The units include six banks of twenty switches each, a digital-to-analog converter, and a meter. The switch-banks are paired based on their function during the monitoring: 1) were for anode electrode selection; 2) cathode electrode selection; and 3) for the measurement electrodes. Each electrode served in one of the three roles during a single measurement and most electrodes served in all roles for a complete set of measurements.

[3] Fluke Electronics Canada Inc. 101, 1144-29th Avenue N.E., Calgary AB T2E 7P1, (403) 291-5215.

All units except the meter interfaced through a master switch unit between the IEEE bus and the System 21^{tm} bus. This interface unit was a PM2101, and was a simple communication device that resided transparently on the IEEE bus. The controller sent and received data from the units on the System 21^{tm} bus by addressing through the interface unit using the GPIB address of the interface and the Philips address.

A Philips PM5139 function generator was used as the alternating-current excitation source. Tests were performed to determine the best excitation signal to stimulate a clay/sand material for *in situ* monitoring. The source had to be free from distortion, accurately measured and set, and reliably maintained [89]. The tests identified more precisely, the properties of buffer of interest to ERT methods when excited using alternating currents. In particular, frequency, waveform, and current level were identified that would provide the best result for this application of ERT monitoring. The tests better resolved specifications for the instruments, and how to automate the monitoring.

The frequencies used were $\sim$ 0.5, 15, and 100kHz. The reactivity at the 100kHz frequency level is significantly higher than at the lower frequencies. These are in the range of the frequency spectrum where the response is dominated by the absorbed water [57]. Each frequency falls into a distinct range where the reactivity remains at a constant level. A current level between 5 and 20mA is best for this application of the ERT method [81] which is well within the operational range of the generator.

5.2.2 Software

The software is comprised of both commercial and locally developed programs. The locally developed software was used for control of the data-acquisition electronics by the microcomputer (Figure 2.1). The commercial software installed on the system included the drivers for the GPIB card, the Ethernet card and the Bernoulli drive. The operating system was

Microsoft Windows for Workgroups[4] running "Desktop". The Desktop environment included a scheduler for automatic execution of the logging software [93]. It also offered the necessary environment for Labview[5] to be used as an aid for debugging. Remote access to the system was done through PC-Anywhere.[6]

Because of the remote location of the URL application, the logging computer networked to a central computer dedicated primarily to file services through a high-speed, fibre-optic link using personal-computer networking software. Data logged by the system transferred via the network to the central computer and network software allowed remote access in any direction on the network [90].

5.2.3 Data-Acquisition System Summary

Although suitable to the response expected in those applications considered here, the system was slow due to the sequential nature of the monitoring strategy. The settling time of the meter was approximately one second and this resulted in significant time to take a set of measurements, although the measurements were very accurate and repeatable. The units were intelligent and were capable of giving their state over the bus, when requested, during monitoring. As well, since the units were modular, the system could be expanded with additional plug-in modules. Figure 5.3 shows an example of a data set collected during the test.

5.3 Preliminary Test with Sand

The test described in Section 5.3 validated the ERT method for monitoring moisture in sand. The apparatus was a 21.5cm length of 10.3cm-radius PVC pipe filled with dry sand, fitted with wire electrodes and capped at both ends with plexiglass. Water was introduced in measured amounts through holes in the side while monitoring was performed.

[4]Microsoft Corporation, One Microsoft Way, Redmond WA 98052-6399.
[5]National Instruments Corporation, 6504 Bridge Point Parkway, Austin TX 78730-5039.
[6]Symantec Corporation, 10201 Torre Avenue, Cupertino CA 95014.

Table 5.1: Water added for tomography measurements. The initial mass of the apparatus was 3648.2gm.

Test	Mass water (gm)	Width wetted region (cm)	Height wetted region (cm)
1	93.4	4.0	3.5
2	219.2	12.0	5.0
3	336.2	12.0	8.0

Thirty-two, 8cm wire electrodes of 18-gauge copper wire were used. They were fastened inside the pipe parallel to the axis and holes were drilled in a line between electrode one and thirty-two. Figure 5.4 shows the apparatus used in these tests. The apparatus was filled with dry sand and an initial measurement of mass was performed. It was then partially submerged in a water-filled tank to introduce the water into the system. The amount of water taken up was controlled by the level of water in the tank and, after approximately ten-minutes, it was weighed to determine the uptake by the apparatus. Table 5.1 shows the amounts of water added for the ERT measurements at each monitoring point. After sitting out of water for another ten minutes, the ERT readings were taken. The water distribution could be viewed through the plexiglass caps in the end of the apparatus. All processing used the same twenty-five excitation electrode pairs, listed in Table 5.2.

An 2.0V signal was used as the excitation source. Two readings were made of the current then the voltage at the source inputs was measured with respect to the cabinet ground. Readings were taken at each electrode before a final current measurement was taken. All voltage measurements were computed from five readings: the first reading was discarded because of the settling time, and a mean value was computed from the remaining four. The excitation current was measured directly from the voltage drop across a known

Table 5.2: Excitation electrode pairs.

anode/cathode pairs				
00 14	16 02	04 22	24 06	08 26
28 10	12 30	04 18	20 06	00 02
04 06	08 10	12 14	16 18	20 22
24 26	28 30	00 06	08 14	16 22
24 30	04 10	12 18	20 26	28 02

resistor between the signal source and the anode.

The empirical formula due to Archie [4], describes the relationship between moisture content and resistivity for a porous material

$$\rho_e = \mu\phi^{-M}s^{-n}\rho_w \tag{5.1}$$

where ϕ = porosity, s = fraction of the pores containing water, ρ_w = resistivity of water, $n \approx 2$ and μ is a constant. Equation 5.1 can be used to derive the following relationship for moisture and resistivity:

$$\rho = a + b\exp(-M/c) \tag{5.2}$$

with a zero and, from Equation 5.1:

$$\rho_e = \xi(\tau e)^M \tag{5.3}$$

where $\xi = \mu s^{-n}\rho_w$, and $\tau e = \phi$, equating $(\tau e)^{-M}$ to $e^{-M/c}$: $c = ln^{-1}(\tau e)$. The porosity of the sand can then be determined [80]: $\phi = exp[-1/c] = .825$.

The conductance matched the water distributions, as observed through the plexiglass ends of the apparatus, considering that ERT methods average over the length of the apparatus due to the line electrodes used.

5.4 Underground Research Laboratory Survey

5.4.1 Method

An ERT method was tested in a full scale, *in situ* experiment at the URL in a borehole fitted with electrodes and packed with buffer. Monitoring electronics were developed, assembled, and used for a period of approximately two years. The data were processed using the algorithm of Wexler to produce a conductance distribution for the buffer which was converted to moisture content using the calibration curve determined from the laboratory tests.

Measurements were taken with thirty-two, 1m-long electrodes and direct and alternating-current excitations. The electrodes were constructed of galvanized cable commonly use in the manufacture of aircraft. By choosing wire electrodes, the processing was reduced from a three-dimensional problem to a two-dimensional problem, based on the assumption that the water distribution had little vertical variation. Figure 5.6 is an illustration of the apparatus.

Figure 5.7 shows the basic finite element mesh with its inner section of sixty-four elements within a central circle and an outer concentric ring of thirty-two elements. The elements in the outer section were formed by the radial lines intersecting the annulus. The electrodes in the mesh corresponded to nodes on the outer edge of the mesh. The area of each element is fairly constant over the full mesh except at the electrodes where the mesh was refined to handle the high gradients in the potential field. Numerical integration, while generating the stiffness matrix, used gauss points and the gauss quadrature method. The conductance at the nodes were used for displaying the result.

The measurements were made by selecting excitation pairs, applying 500Hz alternating current, then taking five voltage measurements at the remaining electrodes. The alternating-current stimulation was done using forty-nine excitation electrode pairs. All monitoring for direct-current response used ten excitation electrode pairs.

5.4.2 Apparatus

The *in situ* test (Figure 5.8) was conducted on the 240 Level in Room 205 in a 0.5m-radius borehole (designated URL-UG-205-01). The borehole was drilled in the floor of the drift to a depth of 5m and fitted with line electrodes (see Figure 5.9). The 240 *Level* is comprised of several rooms at a depth of 240m below surface. Buffer was packed in the lower 2m of the hole to 1.724Mg/m^3, at a moisture content of about 17.94% and constrained from above by a 1-m concrete plug. Because of the method of installation, the variation in the density and moisture content of the buffer was well known: 17.16% to 18.45% for moisture content and 1.605 to 1.804Mg/m^3 for the density [27]. The surrounding rock was fully saturated and was the source of moisture flowing into the buffer, at the rock/buffer interface. A total of twenty-four psychrometers were installed in the buffer for direct and independent measurements of moisture levels.[7]

5.5 Results

Figure 5.10 shows the results for surveys performed from 1993-December-7 to 1994-February-18. The low conductance of the rock is apparent on the circumference of the image. Next to the rock is the conductance high due inflow at the rock-buffer interface. The high noise level is interpreted as due to the conductance discontinuity at the rock-buffer interface. The moisture in flow increases over time as is expected.

Figure 5.11 shows results from between 1993-November-23 to 1994-February-18 along a profile. The processing ran for a total of 150 iterations and was selected to be representative of the data overall. The expected in flow of moisture from the walls of the borehole is apparent as indicated by an increase in moisture at the ends of the plot. The moisture levels computed at the boundary were lower than the actual moisture content because the analysis used nodes placed on the rock-buffer interface. There is a lower conductance due to the rock and the overall result is an average of the two levels.

[7]The positions of the relevant instruments are displayed in the result of Figure 5.12.

The forces internal to the system have the largest apparent influence, significantly more overall then that caused by direct moisture in flow at the boundary. Changes in moisture level of up to 2% in four months affected all regions of the system. The moisture in flow cannot be determined quantitatively because of the effect of the rock wall on the ERT result. However, there is a clear change in the moisture content around the perimeter, restricted to the outer 5cm of the borehole.

Moisture content values were calculated from ERT conductances using two different approaches to calibration. Moisture content data were derived from a least-squares fit to a general form for the calibration curve using independently determined psychrometer moisture content values. This was referred to as *in situ* calibration. Other moisture content data were derived from a calibration curve derived from laboratory measurements on samples of known moisture content. This was referred to as the laboratory calibration.

The conductance-moisture content curve derived from laboratory measurements was calibrated *in situ* to determine the parameters of the calibration curve. To ensure the laboratory resistance measurements were consistent with the point-conductance measurements of the ERT study, the measured conductance was divided by the measurement electrode separation to generate:

$$\partial R/\partial x = \triangle R/\triangle x$$

where $\partial R \equiv \partial V/I$. and where $\triangle x$ is the measured separation and the current (I) is constant. The calibration equation becomes $M = 29.72 + 2.687 \ln A$. The *in situ* calibration calculations were done using the 1993-February-6 data. The values for α and β [82] are 29.515 and 2.34, respectively. The conductance measurements were converted to moisture content using *in situ* calibrations [80]. The results are compared in Figure 5.12.

Figure 5.11 plots changes in conductance moisture data over approximately six months. The differences use 1992-December-5 data as the reference profile. The laboratory calibrations were performed at 1.67Mg/m^3, whereas the buffer was placed at $\sim$ 1.75Mg/m^3 [27].

The higher emplacement density would manifest itself in a higher apparent moisture content but this correction can be shown, as follows, to be insignificant in the range of conditions experienced. The density-resistivity relationship [81] has the same form as the moisture content-resistivity relationship [81], i.e.,

$$\rho = a' + b' exp(-D/c') \tag{5.4}$$

where $a' = 1.42 \times 10^2$, $b' = 6.74 \times 10^5$, and $c' = 1.42 \times 10^{-1}$ were computed as previously. From above

$$\delta\rho = a' + b' \exp[-D/c']\delta D.$$

and

$$\delta\rho = a + b \exp[-M/c]\delta M.$$

Hence

$$\delta M/\delta D = (b'/b)(c/c')(M/D) \exp[(M/D)(c/c')].$$

Substituting the values of a, b, c, a', b', and c' into the above using $M = 17.5\%$ and $D = 1.71\text{Mg/m}^3$:

$$\delta M/\delta D = .00052 Mg/m^3$$

For a difference of 0.8Mg/m^3, this translates into an insignificant apparent moisture content variation.

The ERT measurements, for 1993-December-27, were calibrated to psychrometer moisture values in a best-fit, least-squares manner presented in Appendix B. Where the moisture is known from a direct measurement, the difference between the computed and measured results are used as an indication of the error. A sum is taken over all known moisture values and divided by the number of points in the computation to give a general measure of the quality of the fit (σ^2). The value determined was 0.558.

The conductance from the *in situ* test show a sharp change at the outer edge. This is attributed to the high resistivity of the rock and the response of the field to the electrodes

being placed on the material discontinuity. The laboratory tests had a similar configuration, but with sand in the place of buffer and PVC as the boundary of the material. The result showed that the dry sand, with high resistivity more closely matching that of the PVC, did not display the same contrast. However, as the amount of water was increased, the same effects at the edge were observed as were found with the borehole test.

5.6 Discussion

The purpose of the research of Chapter 5 was to apply the ERT method to monitor moisture in buffer: a soil material proposed to be used as a barrier to moisture in the Canadian concept for the disposal of nuclear fuel waste. Buffer is a sand-bentonite clay material composed of 50% Bentonite and 50% graded silica sand with a moisture content of 50%.

The developments of Chapter 5 started with a presentation of the data-acquisition system used in the application of the ERT method at the URL, and in applications in Chapter 6. Preliminary tests were performed with sand where moisture was introducd into a laboratory apparatus and monitored using ERT. The results showed increasing moisture in the apparatus as additional moisture was added.

A calibration relationship was derived from measurements made on samples of buffer that was shown to be consistant with Archies emperical formula. A method for *in situ* calibration was developed and compared well with independent measurements of moisture. It appears that the moisture distribution has a greater dependence on internal forces than on the direct influence of moisture inflow at the rock–buffer interface.

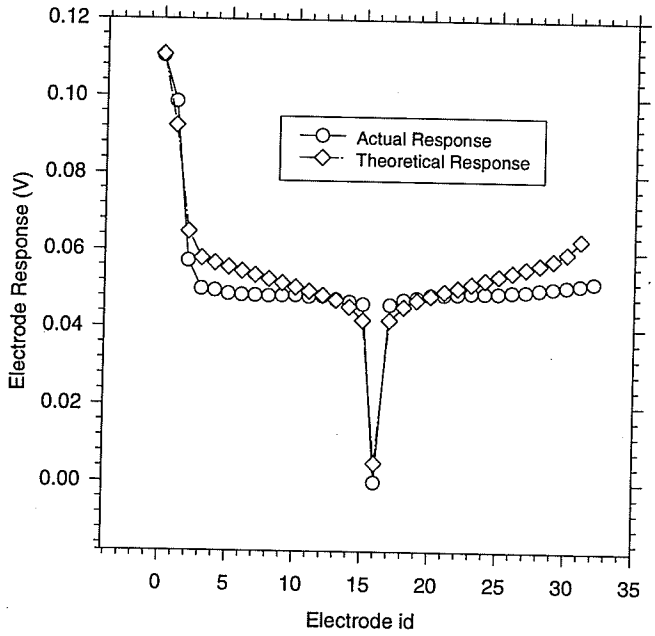

Figure 5.3: Response of electrodes. The actual and theoretical response of the electrodes is shown. The profiles are closely matched with differences due in part to the simplified assumption that the model is homogeneous.

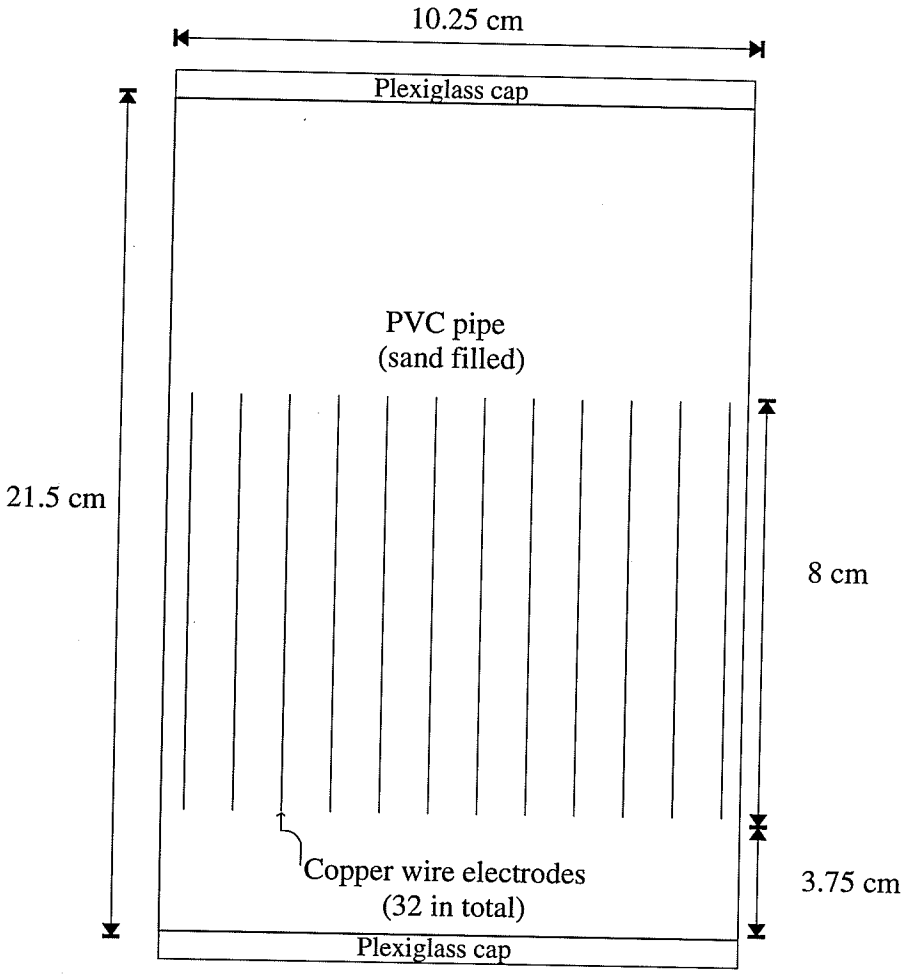

Figure 5.4: Apparatus for laboratory tests with sand.

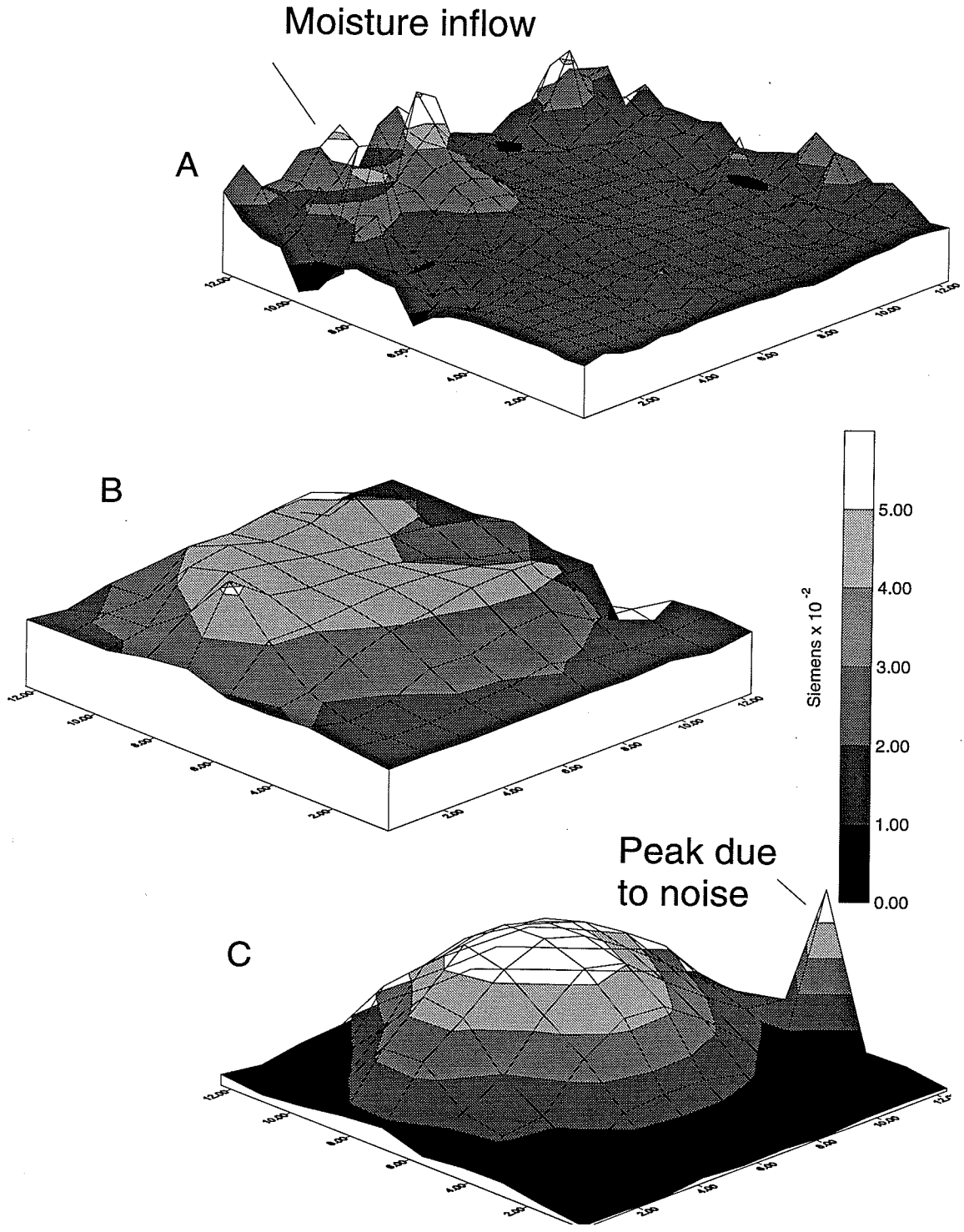

Figure 5.5: Conductivity during moisture in flow. There were 289 unknowns, 25 excitation pairs, 32 electrodes, and a initial conductance of 10^{-6} was used with processing for 150 iterations. Moisture is shown in Table 5.1, progressing from Figure 5.5A to Figure 5.5C. The single-point spike in Figure 5.5C is interpreted as noise due to processing.

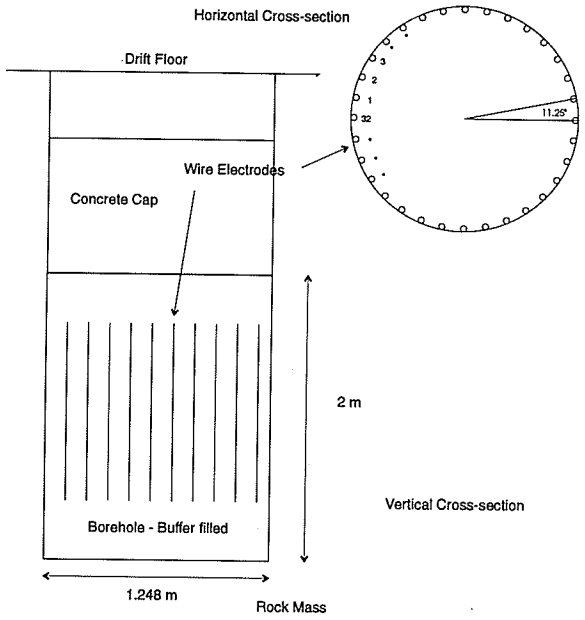

Figure 5.6: Apparatus for Underground Research Laboratory.

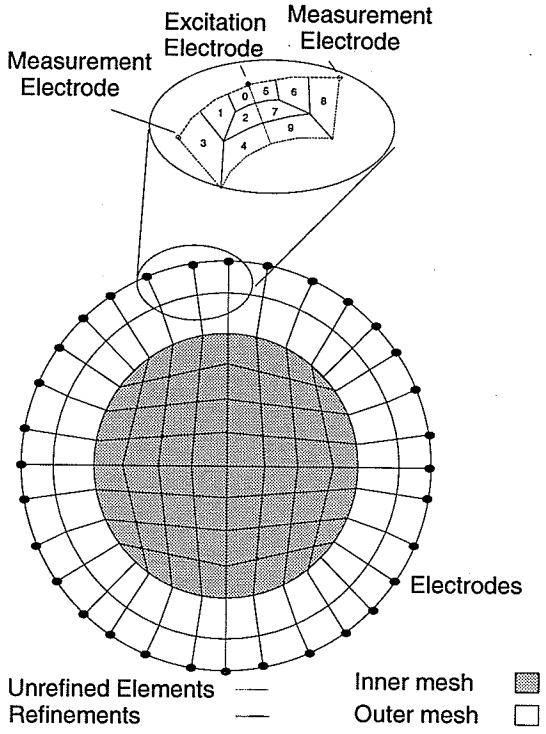

Figure 5.7: Mesh for Underground Research Laboratory.

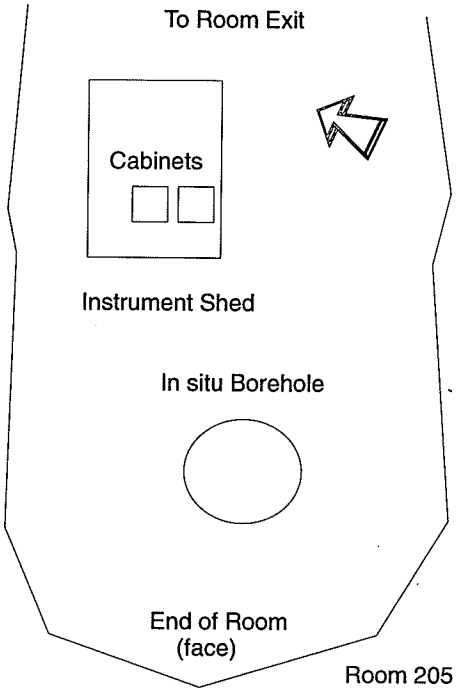

Figure 5.8: Underground Research Laboratory *in situ* test. Location of the data acquisition system and apparatus are shown.

Figure 5.9: Electrodes fitted to borehole wall.

Figure 5.10: Results from URL survey. The surveys were performed from 1993-December-7 to 1994-February-18.

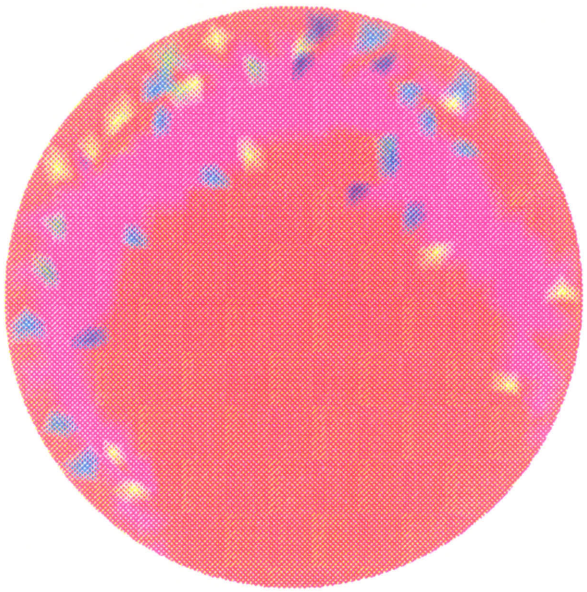

December 7

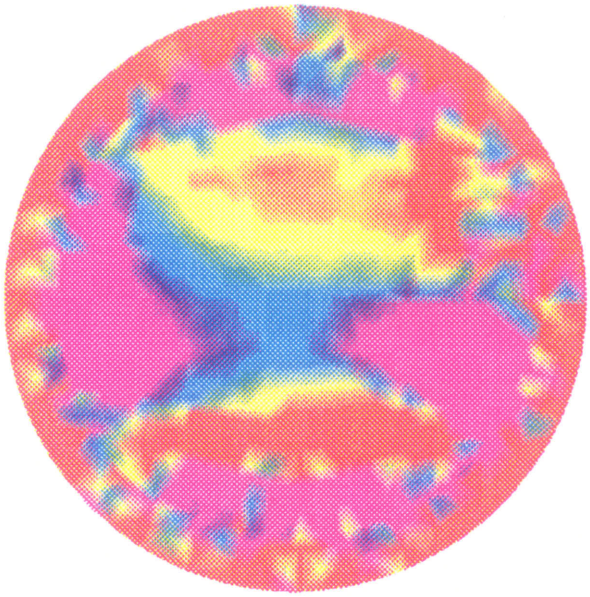

December 16

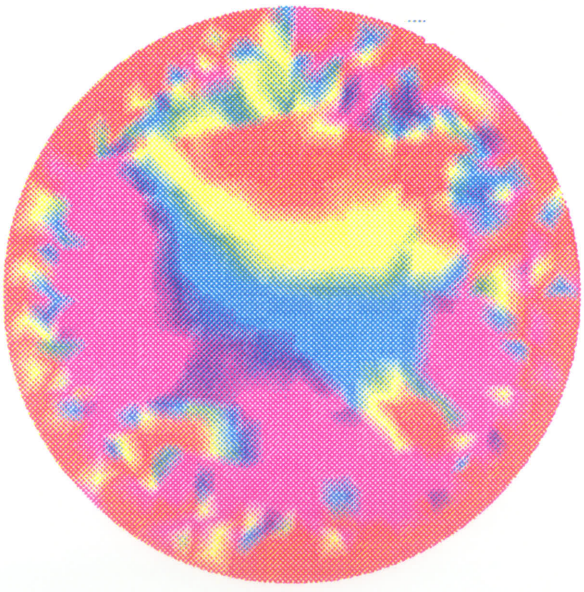

December 27

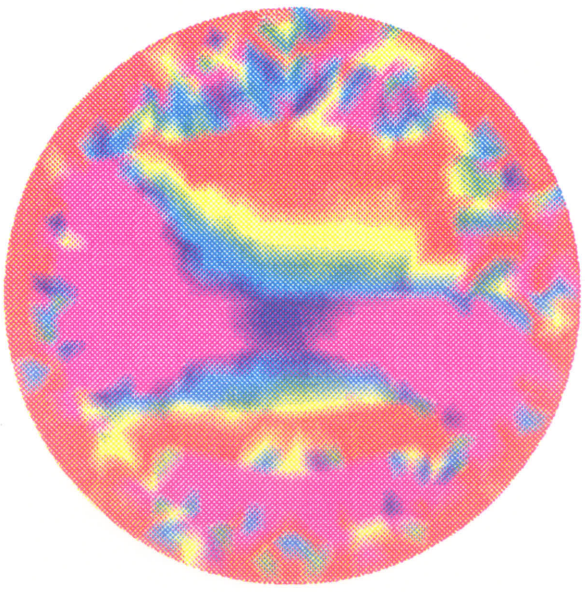

December 29

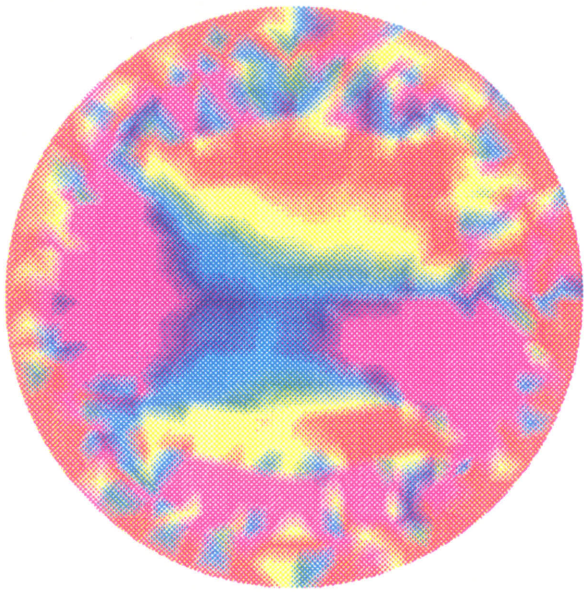

December 31

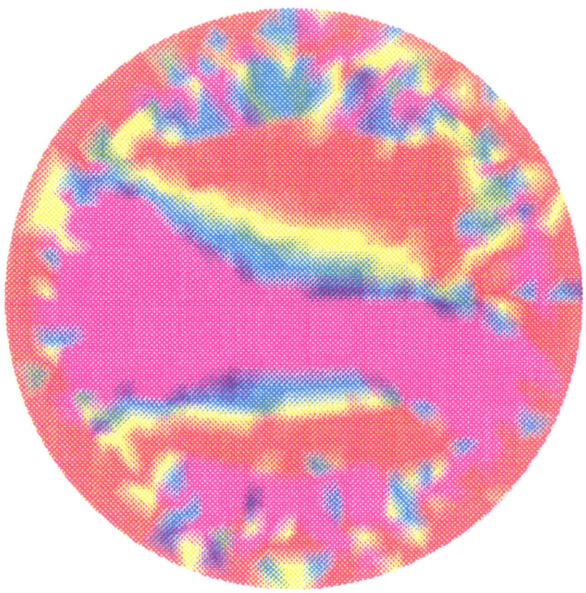

January 2

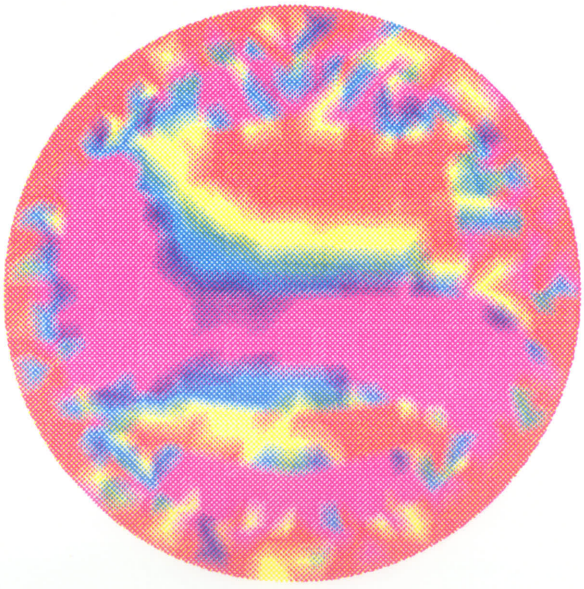

January 4

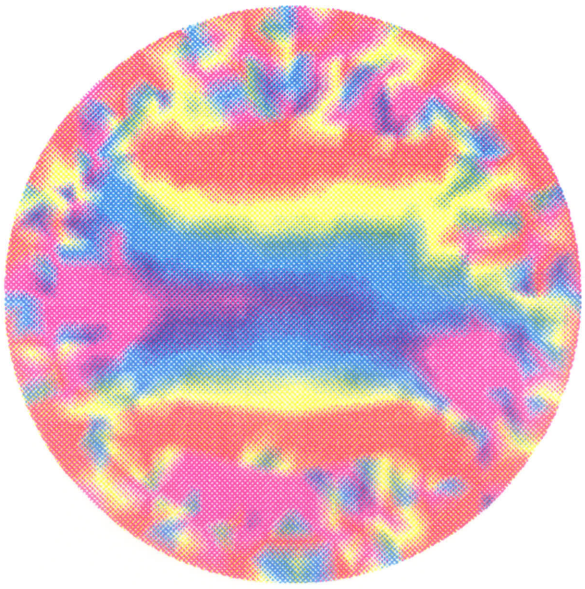

January 14

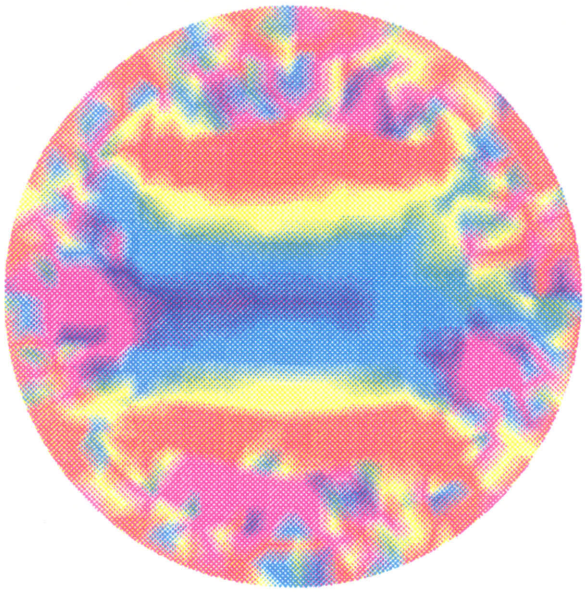

January 16

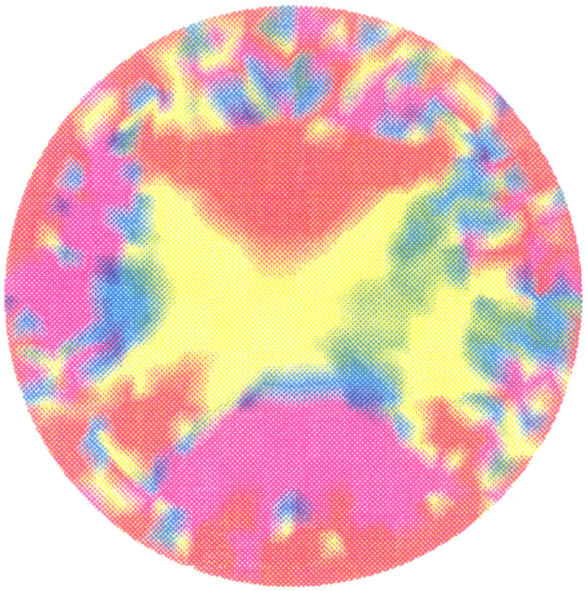

January 18

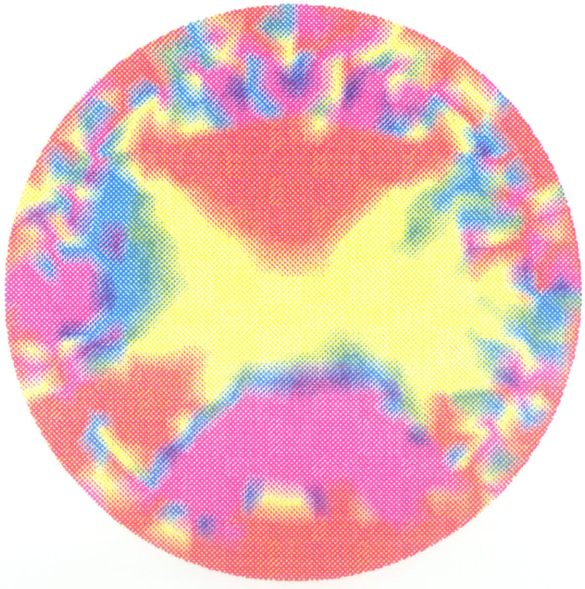

January 20

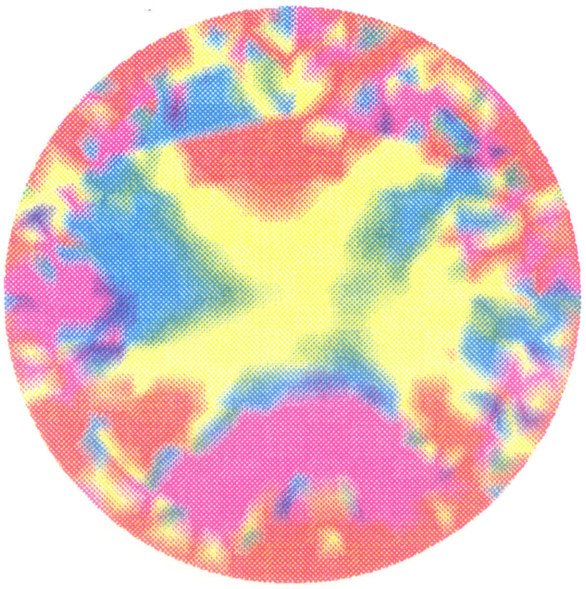

January 24

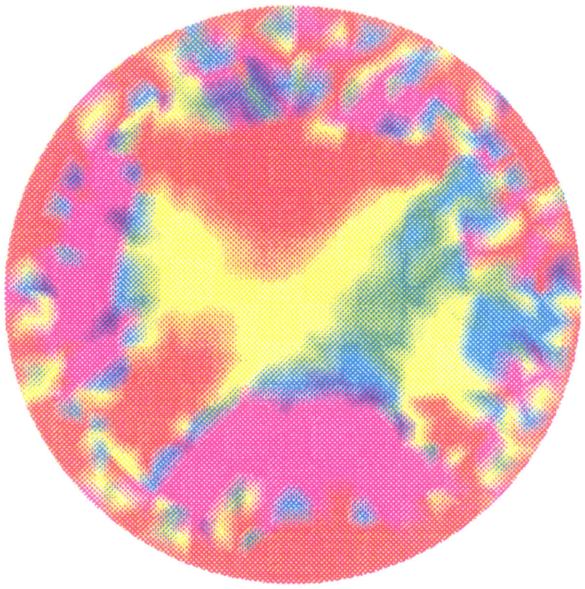

January 26

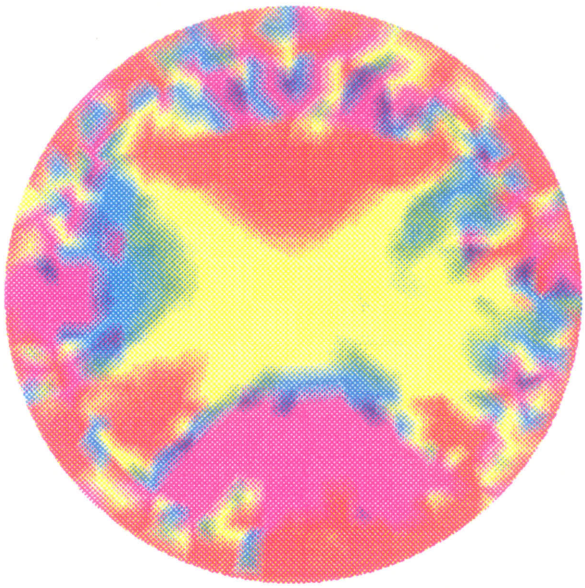

January 28

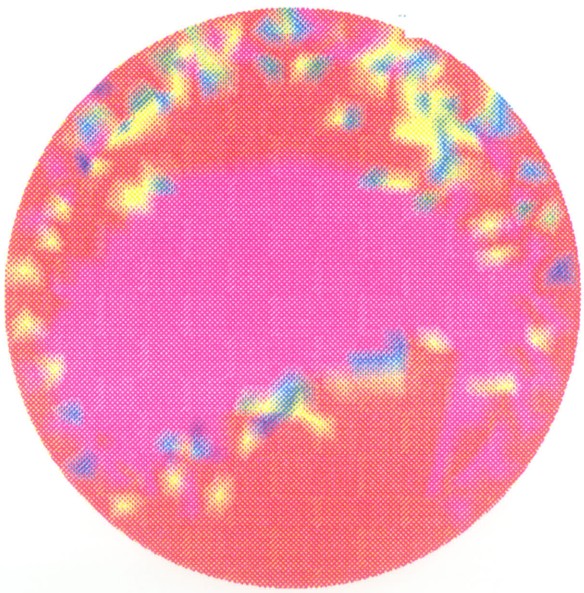

January 30

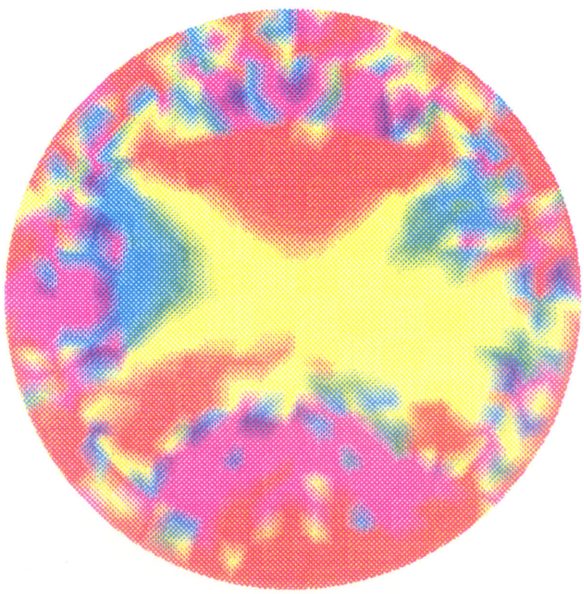

February 1

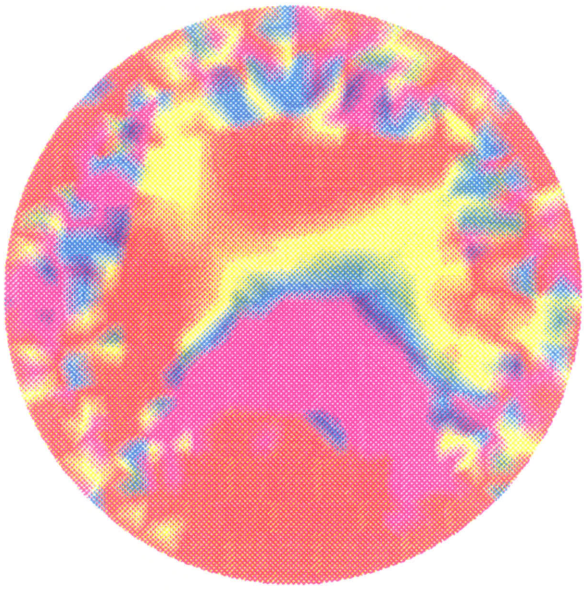

February 8

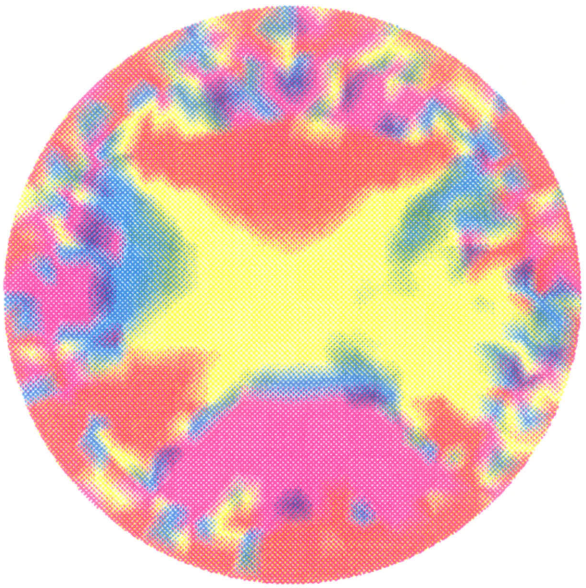

February 10

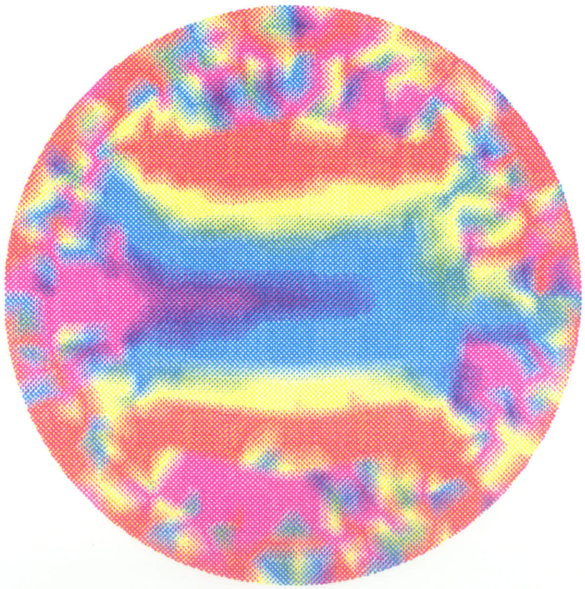

February 12

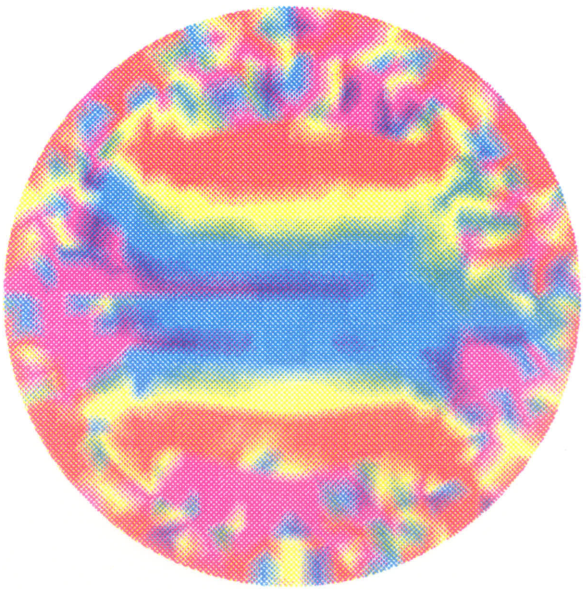

February 14

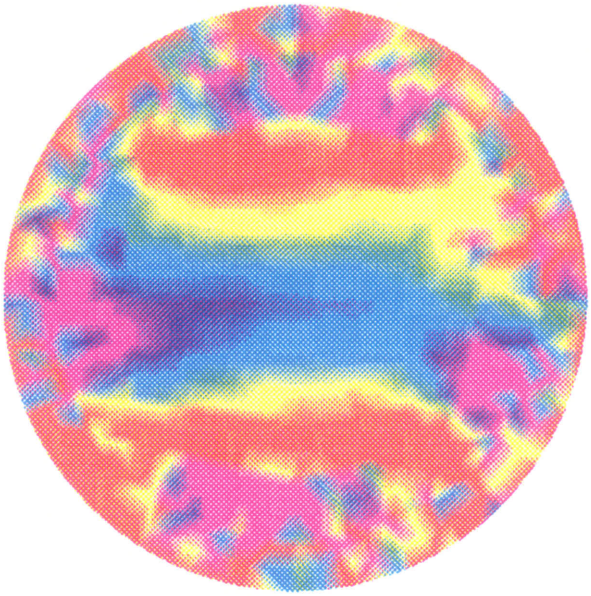

February 16

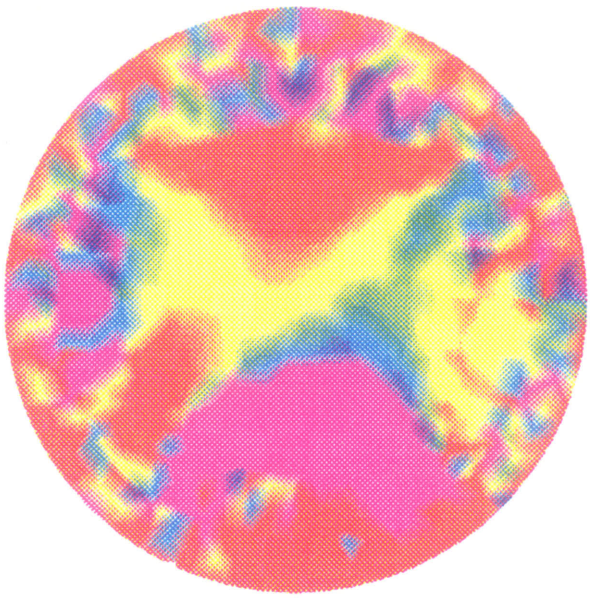

February 18

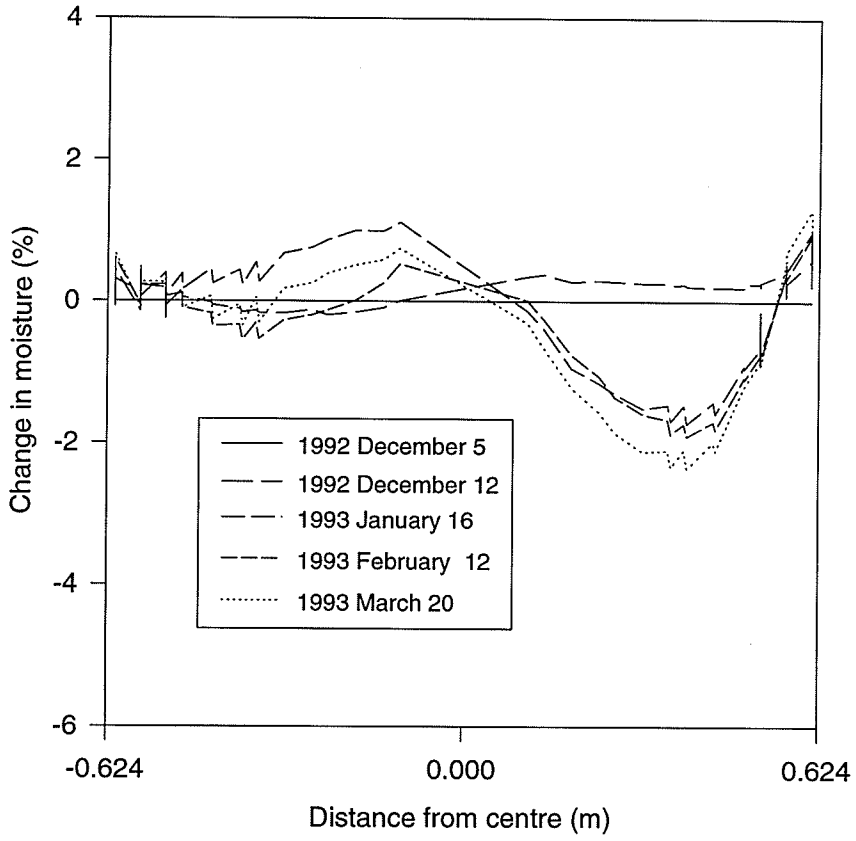

Figure 5.11: Change in moisture content. The moisture content was computed using the calibration curve and the profiles for five days are plotted during a four month period. The reference profile used was 1992-December-5.

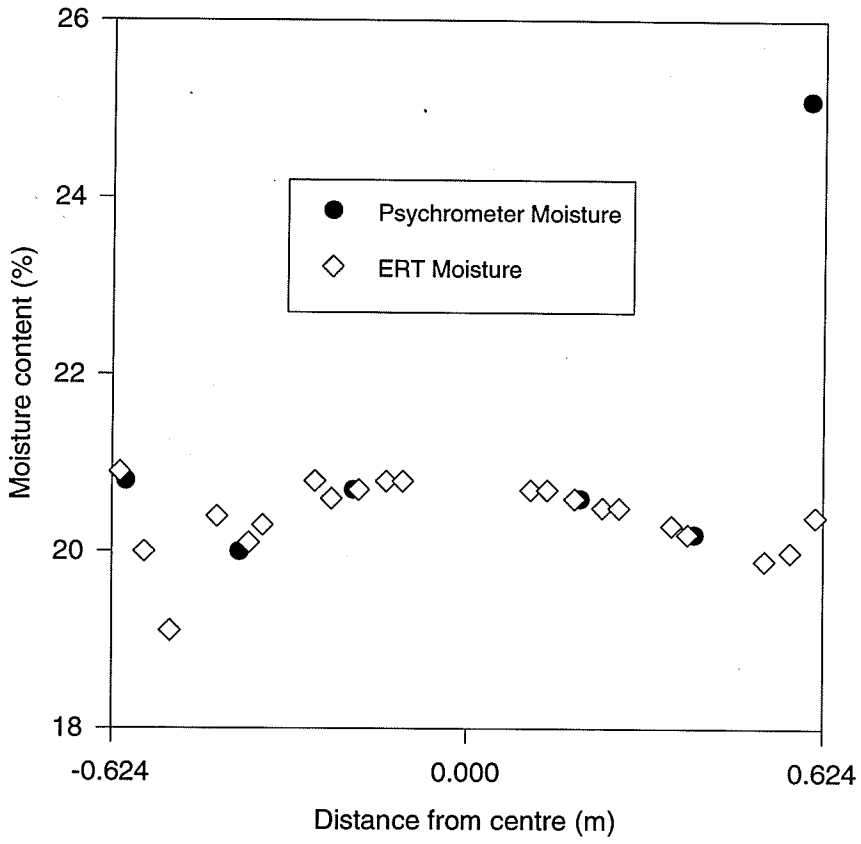

Figure 5.12: Field calibrated data. The conductance data were calibrated using the result of [84]. The psychrometers readings were also plotted.

Chapter 6

Survey of a Low-Level Waste Facility

6.1 Overview

In Chapter 6, the radioactive waste facility remediation problem is considered when an ERT method was demonstrated at an operational waste site. The setting was Atomic Energy of Canada Limited's Chalk River Laboratory Waste Management Area–C in Chalk River, Ontario (see Figure 6.1. The tests began with laboratory measurements in two-dimensions to locate a metal target in sand in a small-scale apparatus. Staged field tests and measurements in a conventional waste disposal facility were performed in three dimensions using surface-only measurements to image trench boundaries and individual targets. In the final step, the ERT method was applied at Waste Management Area–C during two weeks in the month of August 1995, as part of closure activities for the facility.

As will be shown, the ERT method is useful in orientating specific targets and providing detail in regions of interest such as trench boundaries and targets. The ERT method's greatest value to this application is that measurements can be made from surface. The system under study need not be disturbed by instruments in any significant way since the electrodes are not installed in an intrusive manner. In contrast, direct-sensing, invasive methods often damage barriers and this accelerates the release of pollutants and, thus increases the likelyhood of contamination of personnel and equipment. Invasive technologies are still crucial; however, coordinated surveys using ERT methods can support the actual

remediation and waste management activities.

6.1.1 Low-Level Radioactive Waste in Canada

Atomic Energy of Canada Limited is developing technologies for use in the safe storage and disposal of radioactive-waste in Canada [12, 13, 29, 41], with the exception of waste related to uranium mining, milling, and refining. The primary sources of the waste are the nuclear generating units in Ontario, the research and engineering activities of Atomic Energy of Canada Limited, and a relatively small amount from industrial, medical, and research activities within Canada.

Classification of waste is based on the length of time necessary for containment due to the hazardous nature of the material. Three categories are used: low; intermediate; and high level waste. Currently, the total in storage is over 100 000m^3 and this amount is increasing at a rate of 3 000m^3/a [41]. About 80 % of the waste is low-level, 15 % is intermediate-level, and 5 % is highly radioactive.

Low-level waste have hazardous lifetimes of $<$ 150a and are dominated by radioisotopes considered dangerous for $<$ 15a. Chalk River Laboratories is the largest Canadian source for this type of waste. The waste is made up of contaminated paper, mop heads, plastic trash, and discarded supplies and equipment and is buried in sand trenches located above the water table. Other low-level waste, comprised of fission or activation products, is placed in concrete structures. Intermediate-level waste has a hazardous lifetimes of $>$ 150a but $<$ 500a and are dominated by radioisotopes hazardous for $\approx$ 300a. Sources of this waste are ion exchange resins and filters from reactor cooling systems, Co^{60} sources, hot cell waste, redundant equipment, and other waste requiring shielding. High-level waste have hazardous lifetimes $>$ 500a and have their source in irradiated reactor fuel and reactor-core components.

Atomic Energy of Canada Limited is now assessing the performance of disposal concepts in prototype studies to estimate the total effect these systems will have on the environment.

The waste is to be disposed of in a responsible manner that does not burden future generations and it is critical that Atomic Energy of Canada Limited display competence in characterizing these systems to its' regulatory bodies for continuing support for operation and expansion of facilities.

The method of disposal used considers waste type, quantities, and conditioning; geological and environmental conditions; and economic, social, and regulatory conditions. Low level waste disposed by Atomic Energy of Canada Limited in Chalk River uses the improved sand trench (IST) concept in several upland, free-draining, sand dune deposits. The waste is placed in the trenches then packed with a sand/clay mixture. The trench is covered, after filling, with a barrier layer: plastic; gravel; cobbles; etc. The system will be vegetated when full, and contoured to direct precipitation away from the facility.

6.1.2 Background on Waste Management Area–C

Figures 6.2 and 6.14 shows the Waste Management Area–C facility. The facility comprises sand trenches excavated in a fine-to-medium grained sand unit overlying compacted glacial till with a granitic gneiss bedrock. The base of the trenches are from one- to two-metres above the water table. They are a clay/sand soil formulated to retard the migration of radio-nuclides and are permeable enough to allow infiltrating water to escape. The facility covers 4.2 hectares of leveled terrain at an elevation of 163m AMSL and comprises sand trenches evacuated within a fine-to-medium grained sand unit which overlies a compacted glacial till and granitic gneiss bedrock (Figure 6.2).

Waste is buried within unlined trenches approximately 4m $\times$ 3m deep and 90m long excavated using a bulldozer. The waste trenches are backfilled with sand after they are filled with waste and compacted *in situ*. The ground level has been maintained with periodic backfilling to compensate for slumping. In 1982, the method of disposal was changed to a continuous trench that is opened on one side, as needed, while backfilling on the other. Most of the area is capped only with sand; however, in 1983 a 60m $\times$ 120m strip at the south

end of the facility was covered with polyethylene as a sand infiltration barrier to reduce the movement of contaminants. Although the facility was to be used for solid waste, a separate area was created in 1982 comprising three open trenches that receive and disperse chemicals, acids, and solvent in steel, plastic, and glass containers.

The facility is now near its full capacity, and it has been proposed to expand the facilities [62]. The facility does not present any kind of hazard to onsite personnel nor to the general public and the Atomic Energy Control Board (AECB)[1] has given approval for the facility to be increased in capacity to hold a further two-years volume of waste.

6.2 Purpose

The two main objectives of the Waste Management Area–C study were to explore the practical capabilities of the ERT method as a guide for invasive sampling. Further objectives were to

- locate top, sides, and bottom of trenches,
- locate and characterize specific targets within the trenches, and
- select targets for drill-core sampling.

The practical application of the method was also to be investigated to answer

- Whether quick turnaround could be achieved, i.e., could a result be available on completion of field measurements so quality could be assessed before the electrodes were removed? This would allow any activity coordinated with the ERT measurements to proceed without delay, and further ERT measurements could be quickly planned with the benefit of previous results.
- If an effective, full function field unit could be built that would eliminate reliance on outside support. Such a system would deliver the result quickly, before the system is removed from the field.

[1]The AECB is the Canadian nuclear industry regulatory body.

6.3 Method and Results

Tests applying the ERT method were performed starting with a laboratory application in two-dimensions, followed by preliminary field measurements and measurements in a conventional waste management facility, and culminating with a survey at Waste Management Area–C.

6.3.1 Laboratory Study

In the laboratory, a metal target was imaged in two dimensions using a small-scale apparatus comprising a PVC pipe, with wire electrodes, filled with sand. The pipe was 21.5cm in length and 10.3cm in radius capped at both ends with plexiglass. It was fitted with 32, 5.5cm electrodes of 18-gauge copper wire, placed vertically around the inside of the pipe. A brass rod, 2cm in diameter was placed off-centre in the pipe and measurements were made to image the bar. Figure 6.3 depicts the apparatus used in these tests. Figure 5.7 shows the finite element mesh used to recover the image.

Figure 6.4 shows the result from the laboratory test. The metal bar is imaged in its correct position. The processing was done in two-dimensions and so only a vertical average is shown in cross-section.

6.3.2 Preparatory Field Studies

Preparatory field surveys were performed to locate a buried target from surface measurements and to locate trenches in a conventional waste landfill facility. Two surveys were conducted using twenty regularly placed electrodes in a 5×4 grid. The spacing of the electrodes in the first survey was one-metre and one-third metre in the second survey. Voltage readings were made with all electrodes during the course of each excitation. All electrodes were placed on surface. The excitation circuit was selected by connecting the appropriate wires before the computer selectively stepped through the measurement electrodes to take the readings. The excitation source was a portable 60Hz electrical generator and it was

adjusted to 20mA using a variac and ammeter. The current was manually adjusted using a variac. All field surveys were performed in three dimensions from surface-only measurements.

6.3.2.1 Locating a Known Target

To test the ERT method for locating a target in a field setting, a metal barrel 47.5cm in diameter and 70cm in length was buried in sand. Two surveys were conducted, one with the barrel positioned vertically 0.3m below surface and the other with it tilted 15° off horizontal and placed 0.5m below surface. A 5×4 grid of electrodes with 0.3m separation was placed on surface directly above the target. A total of 38 excitations were used during each measurement sequence.

Figure 6.5 shows the results of the surveys along with the regular grid used in the processing. The computed values were centered on each element. This assigns a single value to each element that represents an average over the element. Figure 6.6 and Figure 6.7 are cross-sections through the approximate centre of the targets and shows that the shape and position of the barrel have been recovered in the result. Figure 6.10 shows the interpreted barrel profile for the tilted barrel.

In both cases, where the barrel had different orientations relative to the surface electrode grid, the results were much as expected (see Figures 6.6 and 6.7). However, the interpreted tilted barrel differs more from the ideal than does that of the vertical barrel. An artifact is present in the deepest cross-sections of both results and is characteristic of a region below a highly conductive object. This is a signature that delimits the bottom of the barrel.

The behaviour of the algorithm over the region of the highly conductive barrel is consistent with that predicted by synthetic results; particularly when compared with the performance in the region of the low conducting sand. With synthetic data, the conductivity values for highly conductivity continues to climb: almost exponentially with iteration. Figure 6.11 illustrates this with synthetic data from Fry [37] as compared with data from this

study.

6.3.2.2 Locating Trench Boundaries

A conventional waste landfill facility in Manitoba was the setting for a test of the ERT method for locating trench boundaries. This landfill facility was selected because its history was well known to the author and the layout of the trenches was of a simple and well-defined geometry. A 5×4 grid of electrodes, with 1.0m separation was laid out to span the end of a single buried trench and include a region of undisturbed soil outside the trench. A barrel was dug into the trench to provide a known target. A total of 190 excitations were applied in all possible combinations to include the best excitation patterns.

Figure 6.12 shows the layout of the landfill facility where the ERT method was used to locate trench boundaries and Figure 6.13 shows the result of the survey. The trench edge can be seen as a region of contrasting resistivity. The boundary of this region migrates with deeper images as expected, due to the sloping trench walls, and then it disappears below the known depth of the trench. The buried target is distinguished as a contrasting high in Figure 6.13. A high contrast passes through the centre of the deepest most level and is interpreted to be a region of relatively high moisture.

6.3.3 Waste Management Area–C Study

The Waste Management Area–C survey was performed during two weeks in the month of August 1995, at Chalk River Laboratories as part of closure activities. Figure 6.14 shows the location of the survey grid in relationship to the waste trenches.

To perform the tests, the field tested electronic data acquisition system was disassembled in Manitoba, shipped and reassembled at Chalk River. To avoid biasing the result, information on the facility was not available to the field team until after the survey was complete and most of the processing finished. The location and orientation of the survey grid was determined and electrode locations marked before hand by an independent survey

team. A drilling rig was used to investigate results as they became available.

Two surveys were performed. The first used a 5×10 electrode grid with electrode separation of 3.0m. In this case, one corner of the grid was elevated by sand banks by about 1.5m over two electrode spacing. In the analysis, this was ignored on the assumption that the error due to location of the few electrodes involved would not contribute significantly to the result. The second survey used a 6×6 electrode grid with electrode separation of 1.0m and covered a reduced area within the larger grid.

6.3.3.1 Survey Layout

A 30×30 metre area was marked with a survey grid as shown in Figure 6.15. This region overlays the trenches from the early 1970's—a region of low activity. Figure 6.16 illustrates the physical layout of the trenches. This area was well removed from the polyethylene cover.

In all, two ERT surveys were conducted on the grid. The first ERT survey was done using a 5×10 electrode grid with electrode separation of 3.0m. With in this grid area, a bank of sand elevated one corner of the grid by about 1.5m over a spacing of two electrodes from the corner. This geometric irregularity was ignored during the analysis on the assumption that the error involved would not contribute significantly to the result. The second ERT survey was performed using a 6×6m electrode grid with electrode separation of 1.5m and within the larger grid (see Figure 6.15). Two independent measurement sets were taken using different excitation patterns on the coarser grid. The initial set used fewer excitations to scope the region while the second set corroborated the result and improved on accuracy. Only the final, more-detailed survey is included here.

6.3.3.2 Survey Result

Figures 6.17 to 6.19 shows the result from the Waste Management Area–C facility survey. Linear features present correlate with the locations of the three trenches (Figure 6.18). The shallowest layer, 0-1.5m, shows no significant features which suggests the trench tops are

1.5m below surface. Figure 6.19 shows the result from the finer detailed grid. This result show several regions of high contrast of which two were selected as targets for drilling. Both targets were found to be metal—one target could not be penetrated by the coring machine. From local knowledge and independent survey data, the majority of the waste is known to be packed in plastic bags. The low resistivity apparent in the trenches is in contrast to the expected high resistivity of plastic material and this is interpreted to be due to the moisture trapped by the bags—pooled above and trapped within. Appendix D contains the result from the borehole sampling at the marked locations in Figures 4.11 and 6.14.

Low ion content of the sand could have had a significant effect on the success of the survey. Sufficient driving voltages are necessary for adequate measurement levels in the survey volume and to avoid nonlinear responses observed at low current [81]. The result showed that this is not a problem.

6.4 Applying Peak-Detection Filtering

Peak-detection filtering was applied to a synthetic case representative of a conductive barrel. The synthetic barrel case, was composed of homogeneous upper and lower cross-sections with regions of contrast (see Figure 6.20) placed in the centre of each of three intermediate regions. The result is included in Figure 6.21 with the error function included in Figure 6.22. Figure 6.23 is the result when peak-detection filtering is applied to the real data. The behaviour of the algorithm over the highly conductive barrel region is consistent with that predicted by synthetic results; particularly when compared with the performance in the region of the low conducting sand. With synthetic data, the conductivity values for highly conductive regions continue to climb—almost exponentially with iteration. Figure 6.11 compares data from synthetic data [37] with data taken from this study, to illustrate this point.

Other image processing strategies could further enhance results. A normalizing function could account for the increasing function values with depth to eliminate smearing with

depth. As well, peak-detection filtering could be done to better resolve the bounds of the target.

6.5 Conclusions

The ERT field survey recovered the impedance of a barrel buried in sand from surface measurements. The result deviated from the ideal, more so with depth, which is most likely due to the increasing distance from the electrodes. This degradation in the result could be reduced by electrodes strategically placed below the surface, but this would make the survey more difficult to perform. In a carefully designed survey where conditions are not known, a combination of surface and subsurface electrodes would apply the ERT method to best advantage.

At Waste Management Area–C, the ERT survey located trenches using surface measurements. High conductive targets selected from the detailed survey were identified and selected as targets for drilling (see Figure 6.19).

The ERT method complimented the other characterization activities, such as drilling, and provided valued information (See Figure 6.24. The result of this work shows that ERT methods are valuable tools in characterizing waste facilities.

Problems were experienced with the electronics and only an estimated 5% of the target sample population for each set of measurements was acquired. As a result, fewer surveys were performed and the resolution of those surveys were much reduced. This reduced the overall scope of the study [91]. From this result, there is every indication that all of the original goals are achievable. The current excitation levels and the dimensions of the survey grid needed in this application were achieved. The resolution of this work was approximately 0.5m on the fine grid. With the current data acquisition system, this resolution could be improved to better than 0.1m on a similar grid spacing.

Three goals of additional work are to

1. Locate the water table and moisture plumes to infer moisture distribution and movement,

2. Test the resolution of the method in field trials, and

3. Test an innovative design of vertical electrodes to allow three-sided measurements

With its remote sensing properties, the ERT method offers broad and distributed monitoring in contrast to point readings of more conventional approaches. The method could also be used to monitor moisture movement over time as it detects changes across surfaces and within volumes. This work demonstrated the robustness of the method when a partial ERT set of data provide meaningful results. A practical system, permanently installed, could be expected to degrade with age yet still be useful for continuous and long-term monitoring.

Figure 6.1: Waste Management Area–C operations.

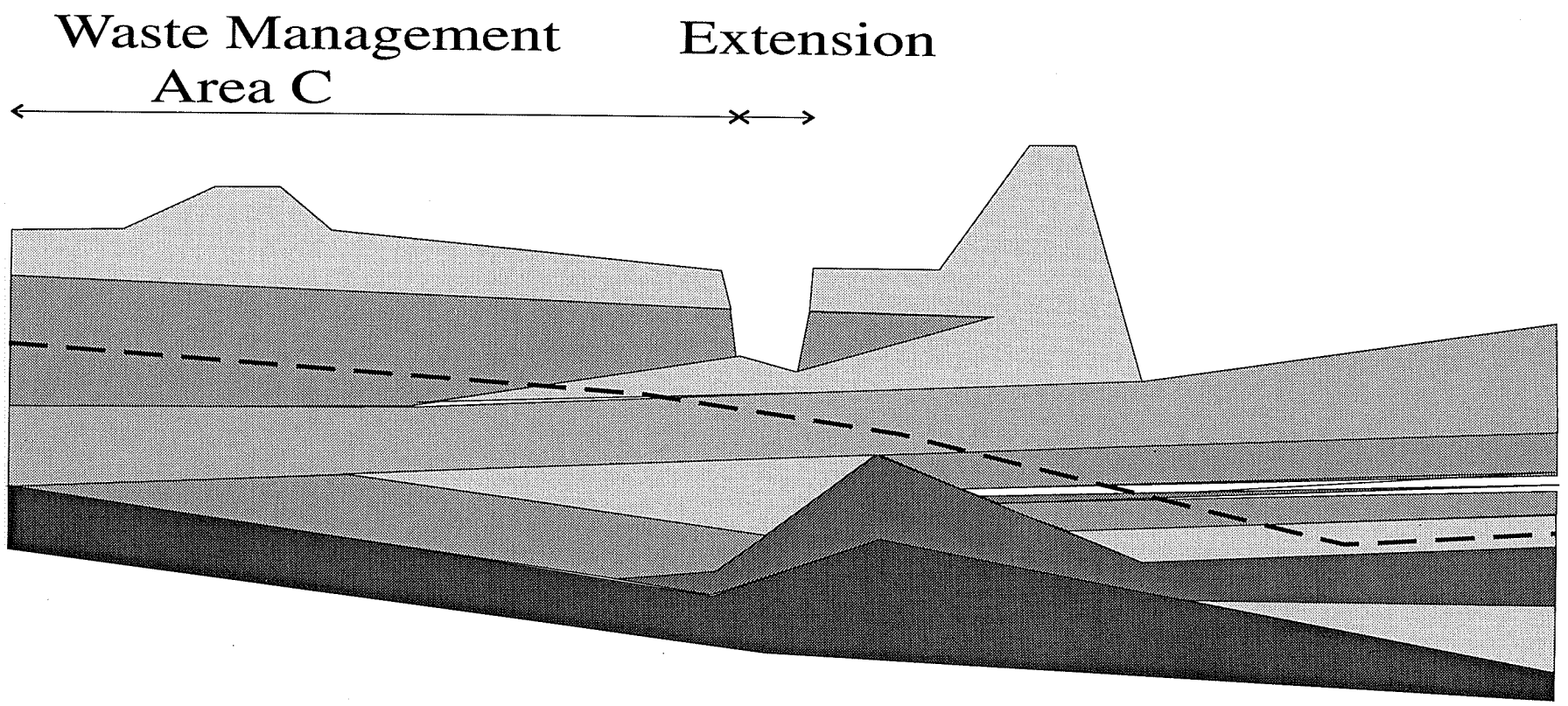

Fine - Medium Sand

Fine Sand

Very Fine Sand

Interstat Silts and Sands

Clayey Silt

Till/Bedrock

Water Table

Figure 6.2: The geology of the Waste Management Area–C facility. This figure, based on [67], is not to scale as it has been exaggerated in the vertical direction.

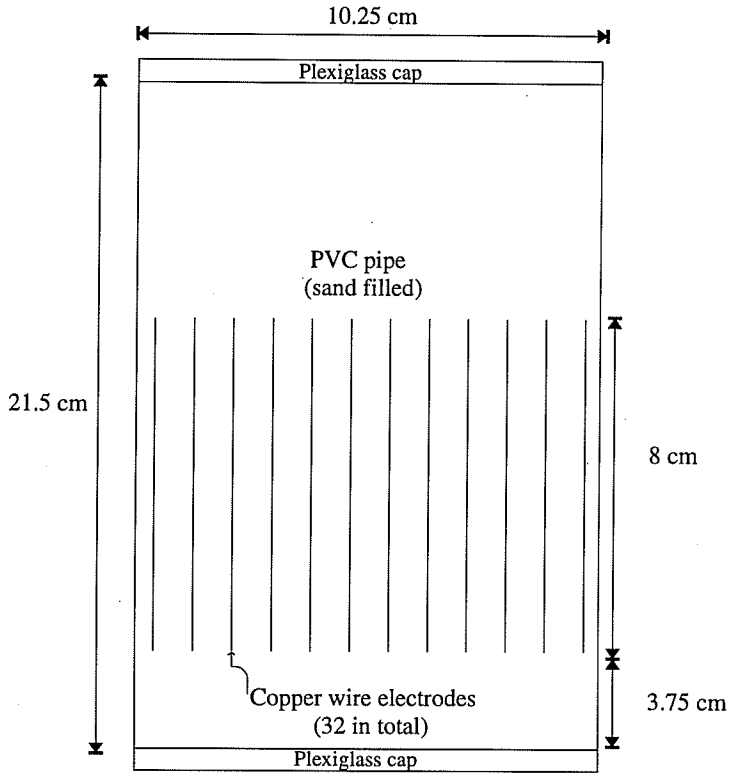

Figure 6.3: Apparatus from laboratory tests.

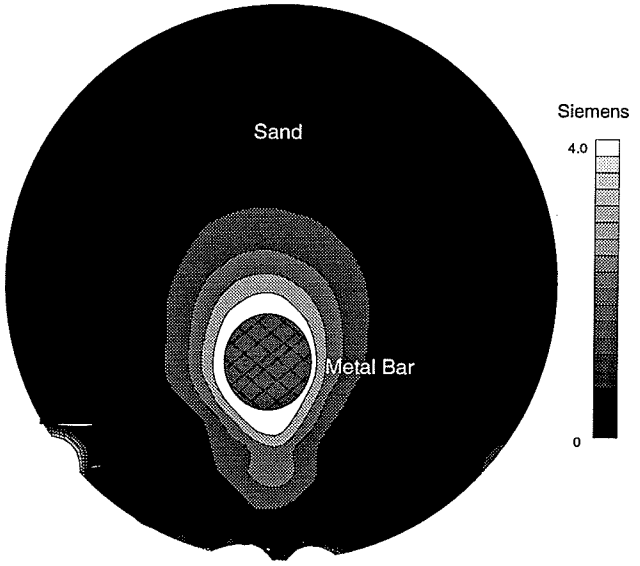

Figure 6.4: Laboratory test with metal. The metal bar was recovered in its correct position.

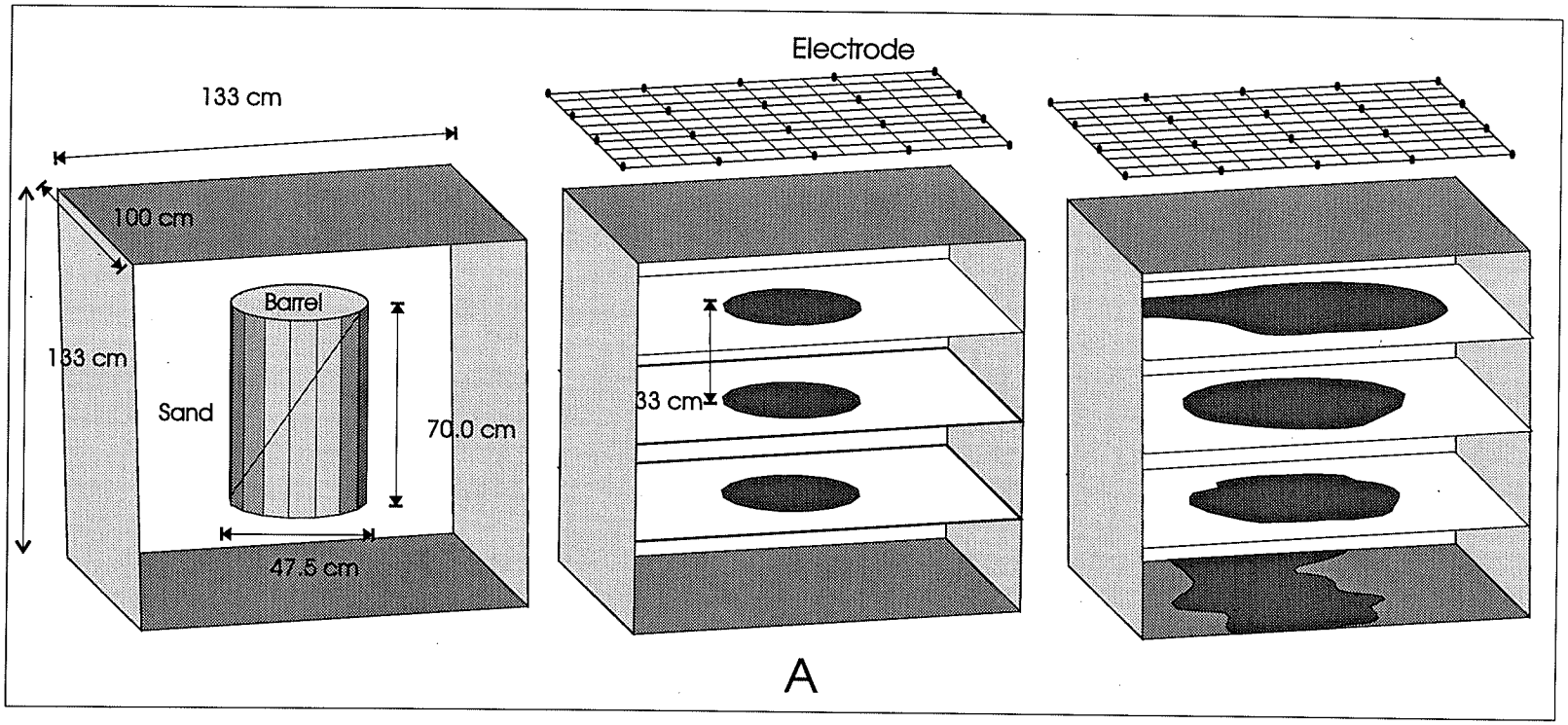
Electrode
133 cm
100 cm
133 cm
Barrel
Sand
70.0 cm
47.5 cm
33 cm
A

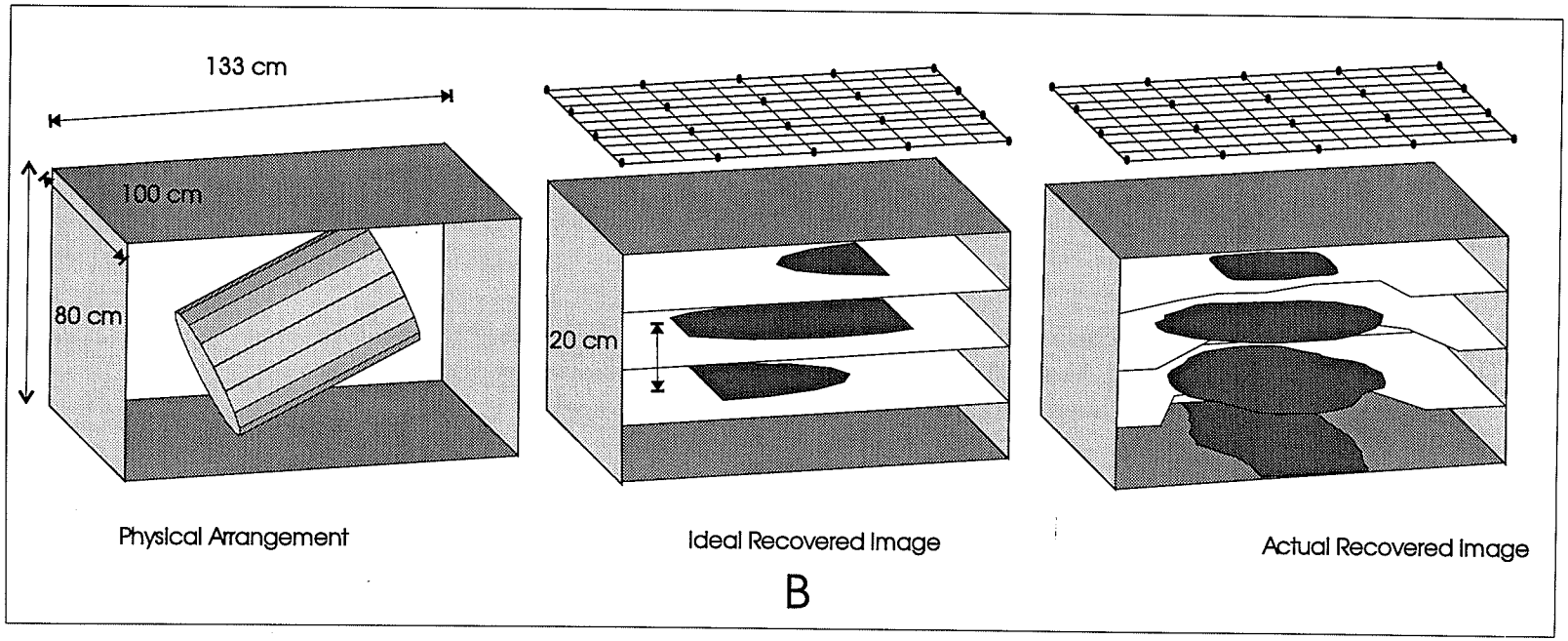
133 cm
100 cm
80 cm
20 cm
Physical Arrangement
Ideal Recovered Image
Actual Recovered Image
B

Figure 6.5: Barrel surveys. The processing grid is superimposed on the image. Figure 6.5A shows the vertical barrel and Figure 6.5B shows the tilted barrel. Shown are the physical arrangements, the ideal recovered image, and the actual image recovered.

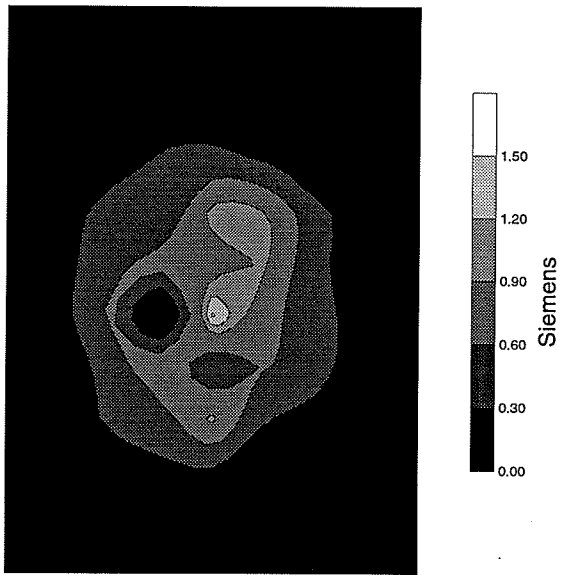

Figure 6.6: Cross-section of vertical barrel. The plane lies horizontal to the surface at the approximate mid-section of the barrel.

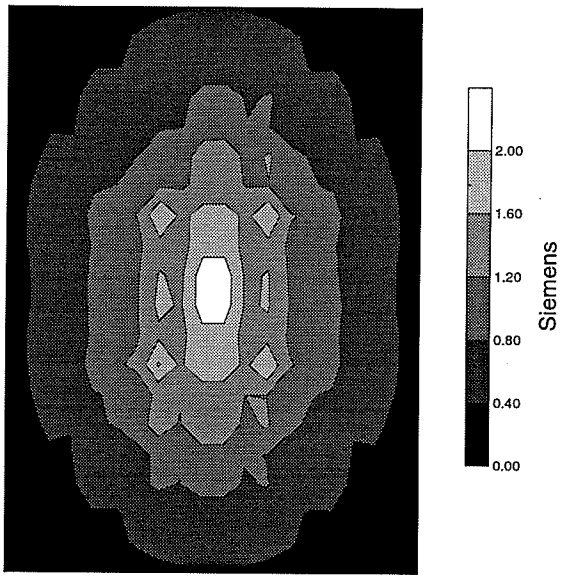

Figure 6.7: Cross-section of tilted barrel. The image plane lies horizontal to the surface at the approximate mid-section of the barrel.

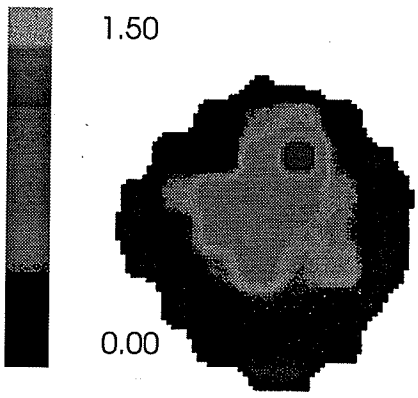

Figure 6.8: Photo image of vertical barrel.

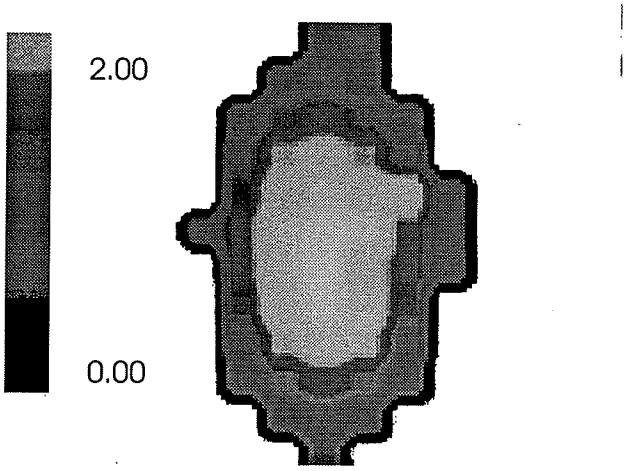

Figure 6.9: Photo image of horizontal barrel.

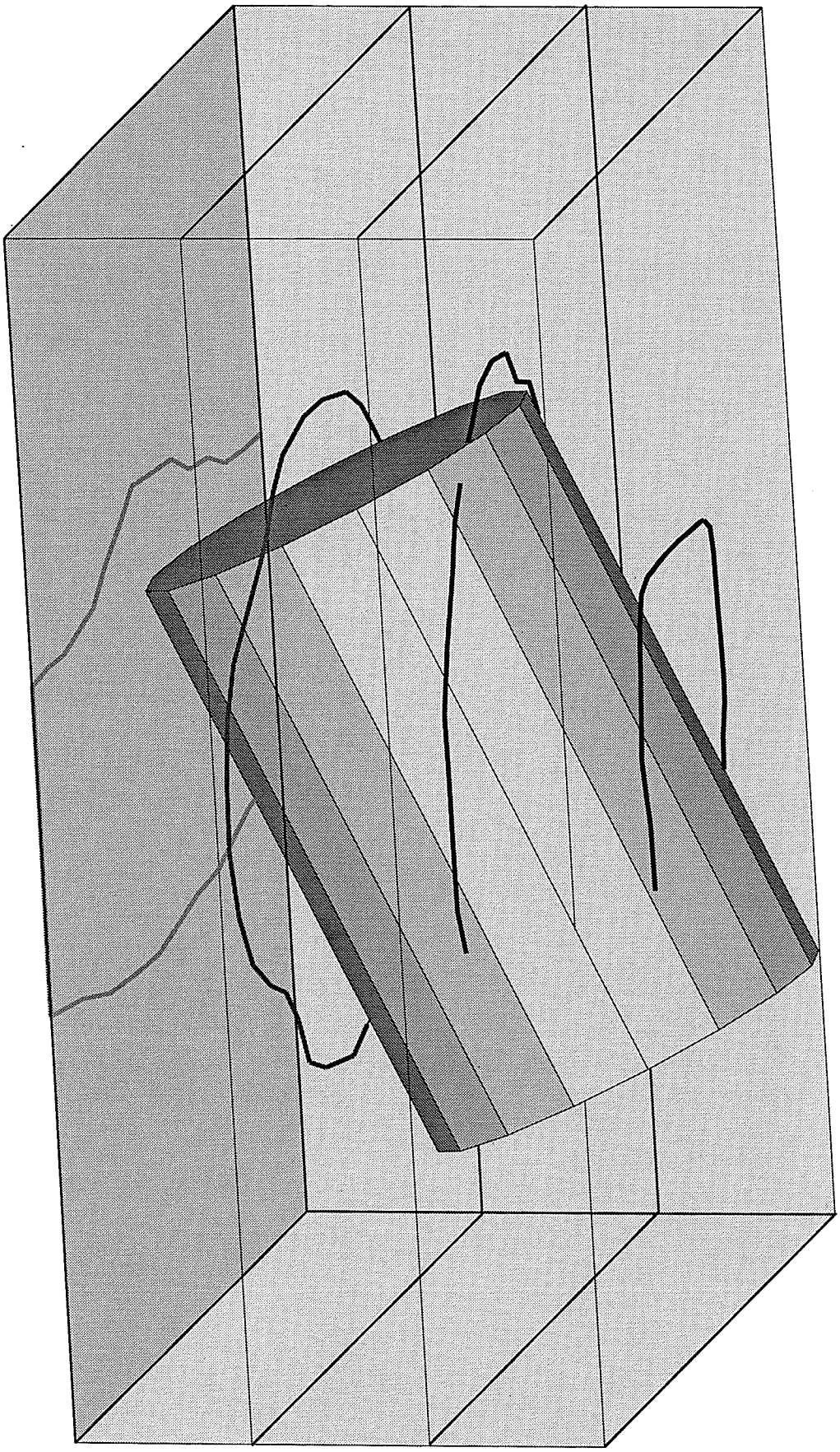

Figure 6.10: Isometric barrel with interpreted outline.

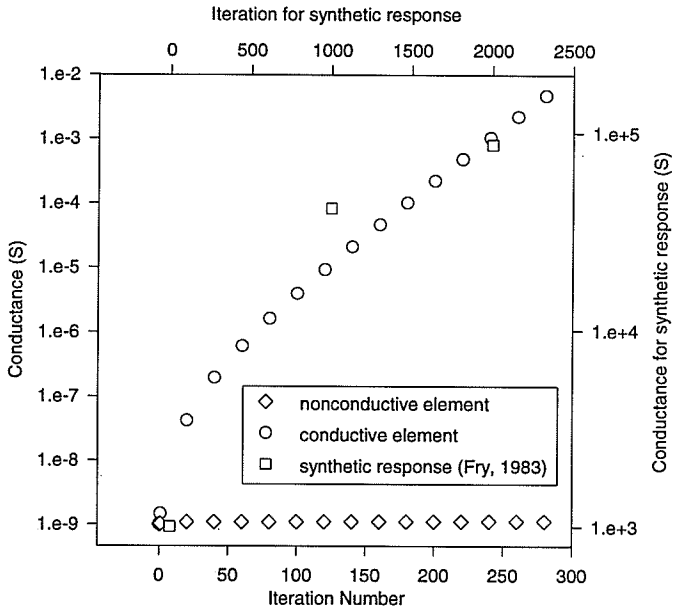

Figure 6.11: Real and synthetic data.

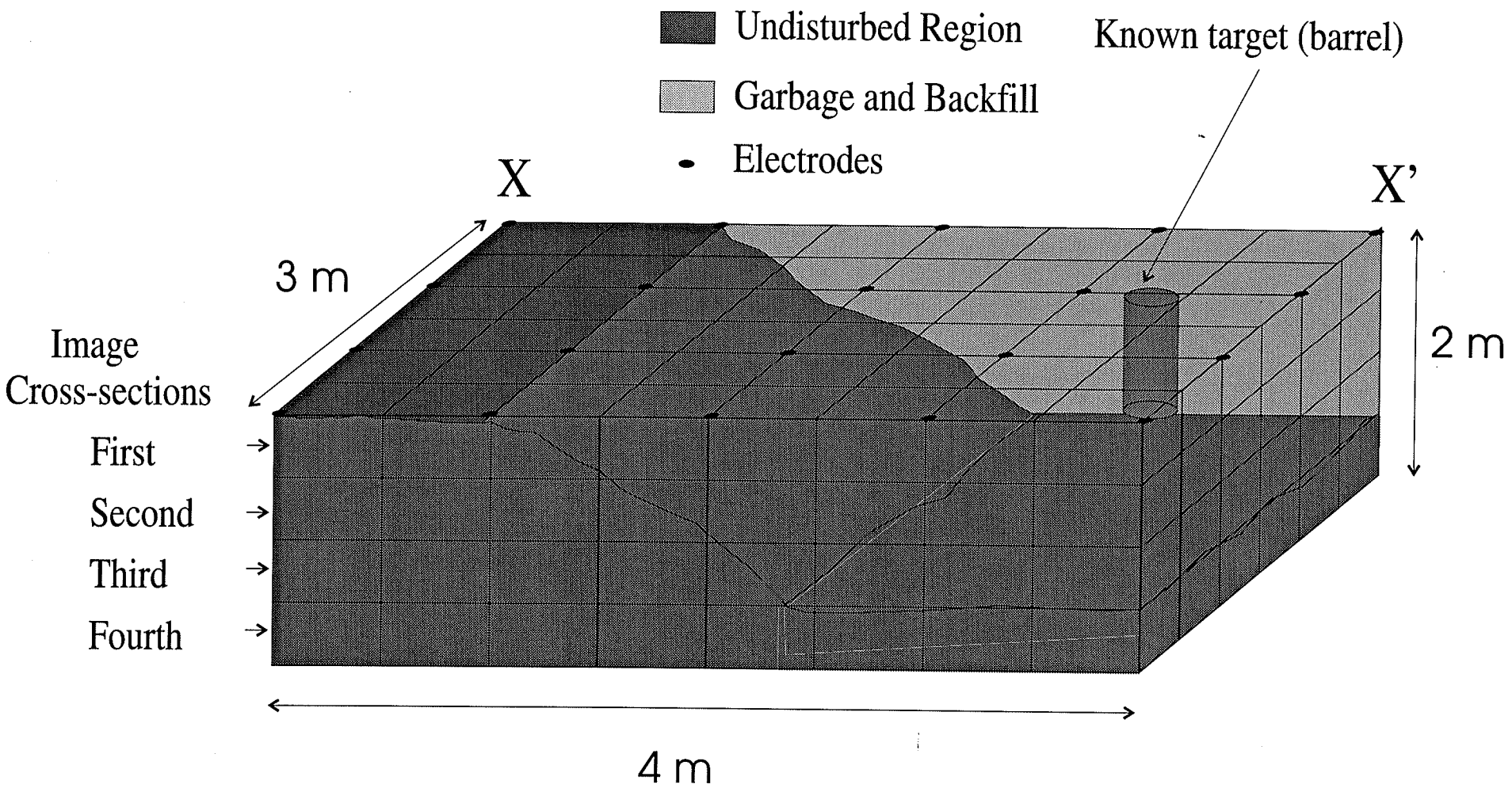
Undisturbed Region
Garbage and Backfill
Electrodes
Known target (barrel)
X
X'
3 m
2 m
Image
Cross-sections
First
Second
Third
Fourth
4 m

Figure 6.12: Layout of conventional waste facility. Markers 'X' and 'X' are shown to orient images in Figure 6.13. The grid spacing is 0.5m.

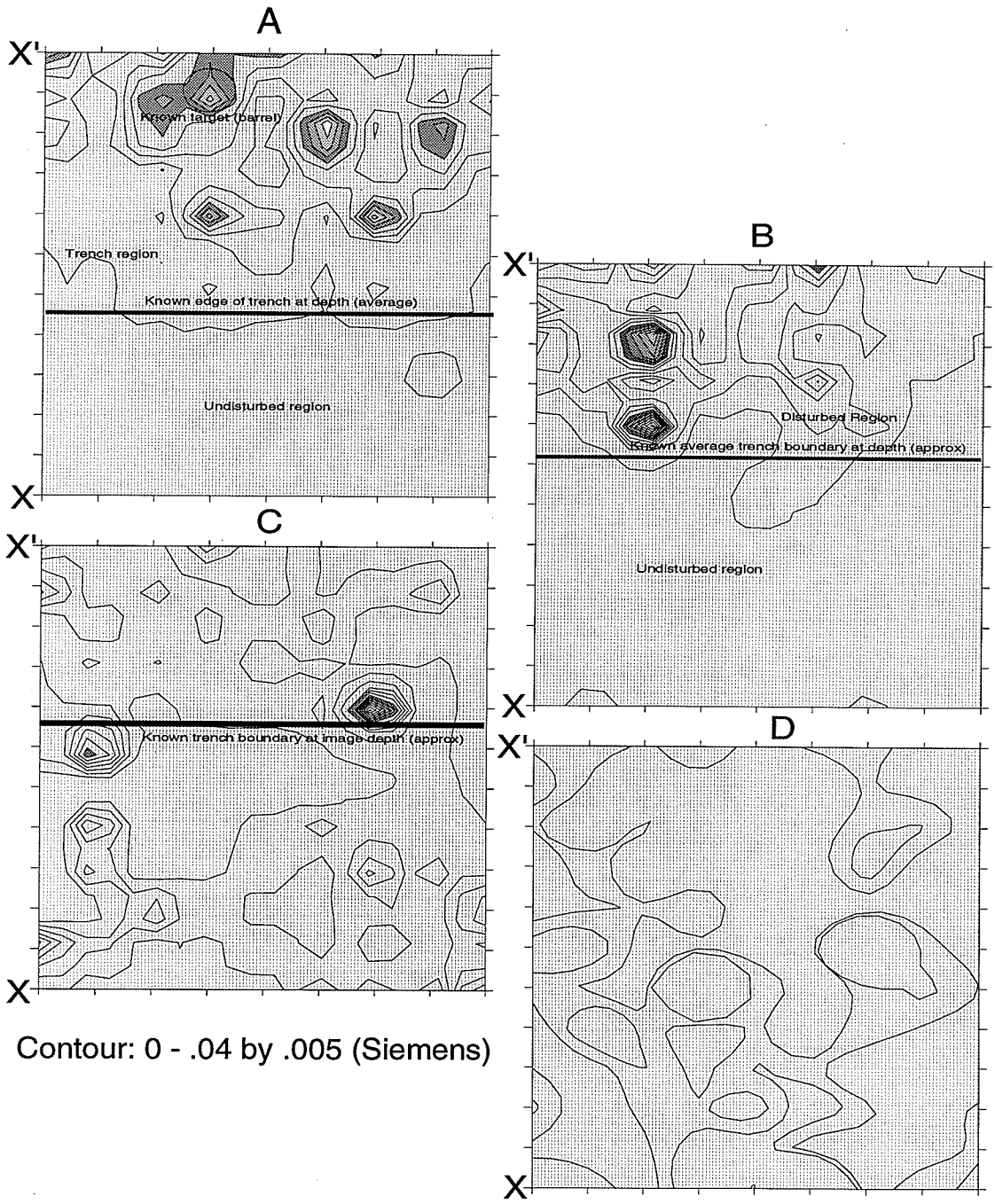

Figure 6.13: Result of conventional waste facility test. Computed conductance is displayed at depths of 0.17m, 0.50m, 0.80m, and 1.16m in Figures 6.13A to 6.13D, respectively. The dimension of this image is shown in Figure 6.12.

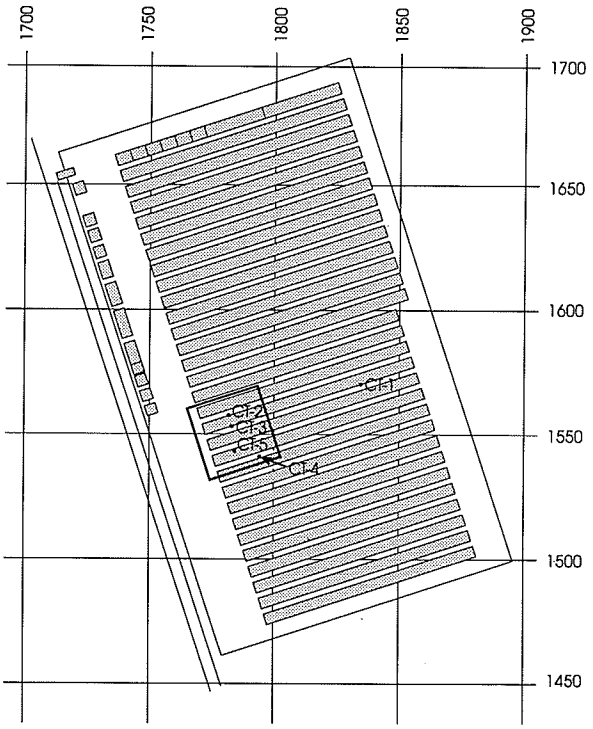

Figure 6.14: The Waste Management Area–C grid layout. The location of the survey grid is overlaid on a map of the waste trenches. The borehole locations are marked. (Appendix D describes the cores corresponding to the locations marked.)

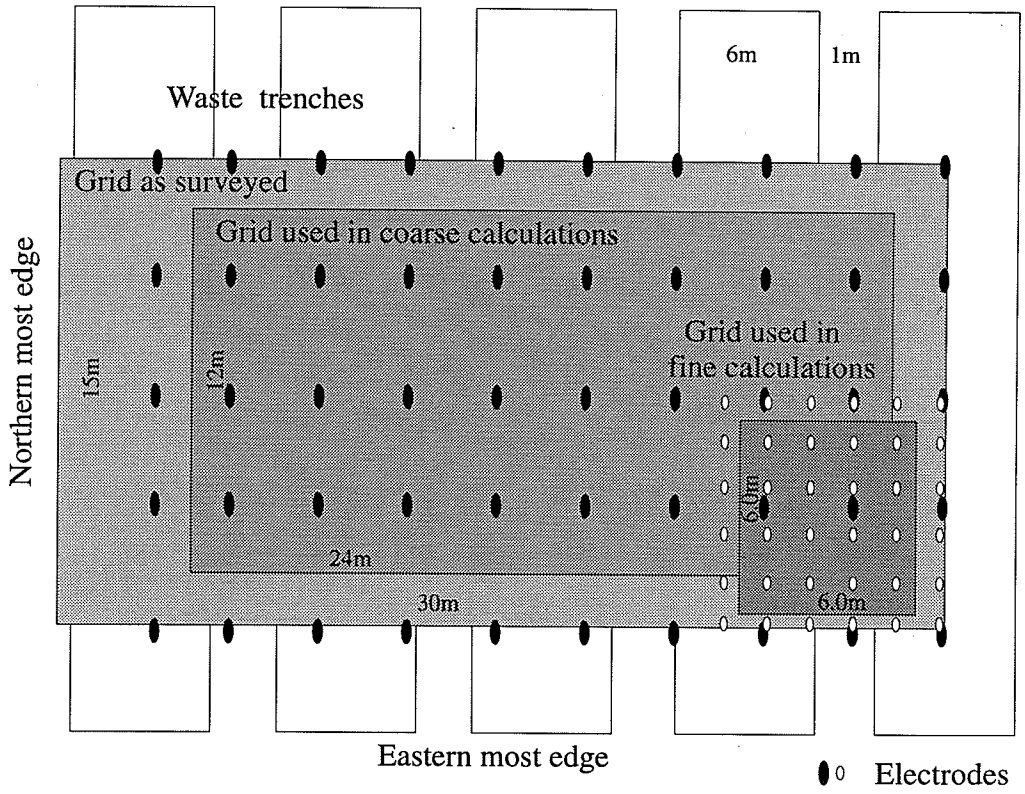

Figure 6.15: Grid for Waste Management Area–C. Shown are the grids used for both the extended and detailed surveys. The grid as surveyed shows where the electrodes were physically placed while the coarse and fine grids show the regions where the conductance was actually calculated. The electrodes of the outermost line on the north edge were not used.

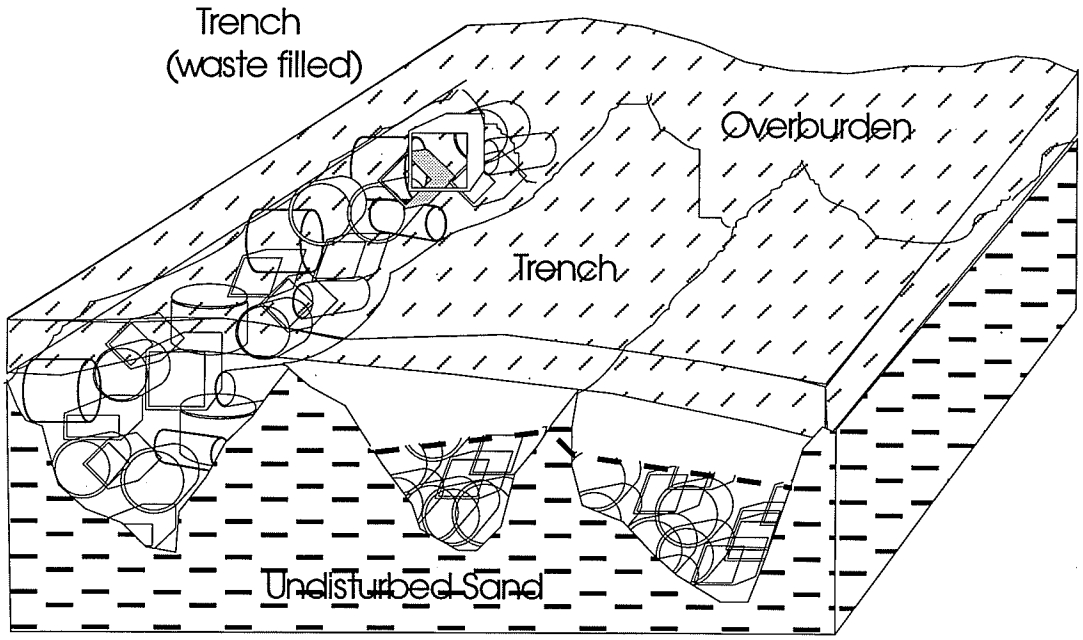

Figure 6.16: Physical layout of trenches.

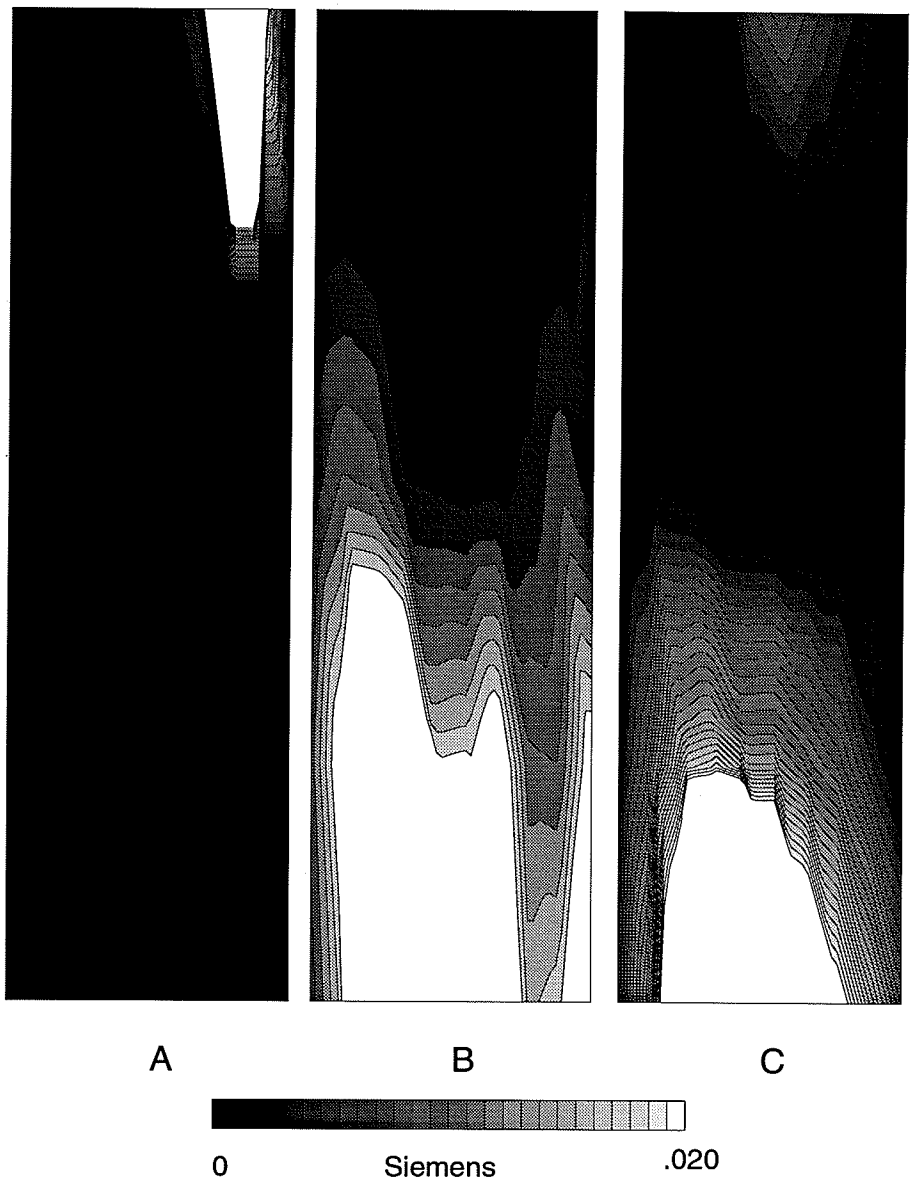

Figure 6.17: Result from Waste Management Area–C. The first, third, and fourth level are displayed here. Figure 6.17A shows the 0.0-1.50m level, located at 0.75m, Figure 6.17B shows the 3.00-4.50m level located at 3.75m, and Figure 6.17C shows the 4.50-6.00m level, located at 5.25m. Scale is shown in Figure 6.15.

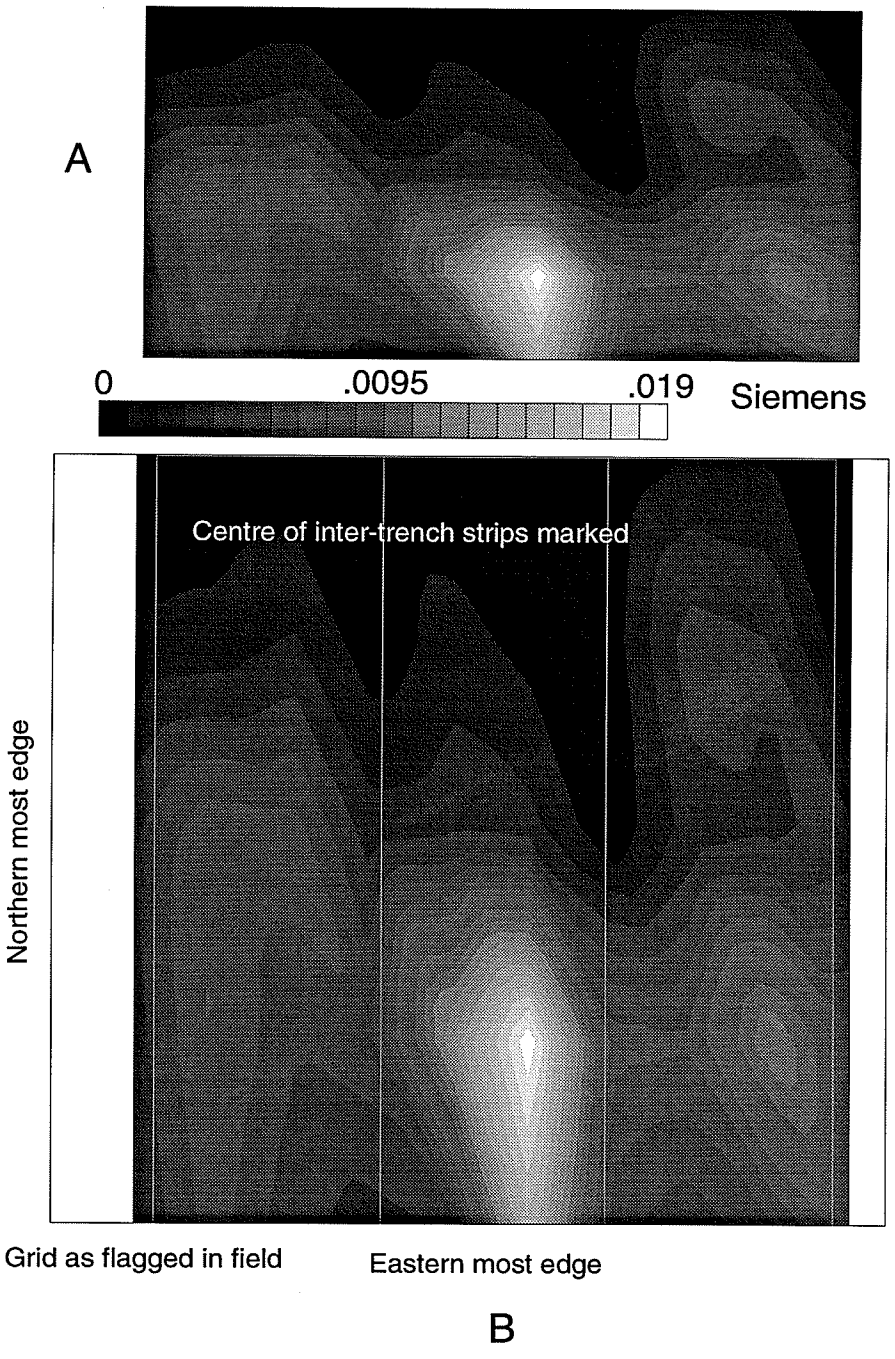

Figure 6.18: Waste Management Area–C trenches. The horizontal cross-section is averaged over 1.5 to 3.0m and positioned at 2.25m. Figure 6.15A shows the result in proportion while in Figure 6.15B, the result has been stretched to emphasize the trenches. Scale is shown in Figure 6.15.

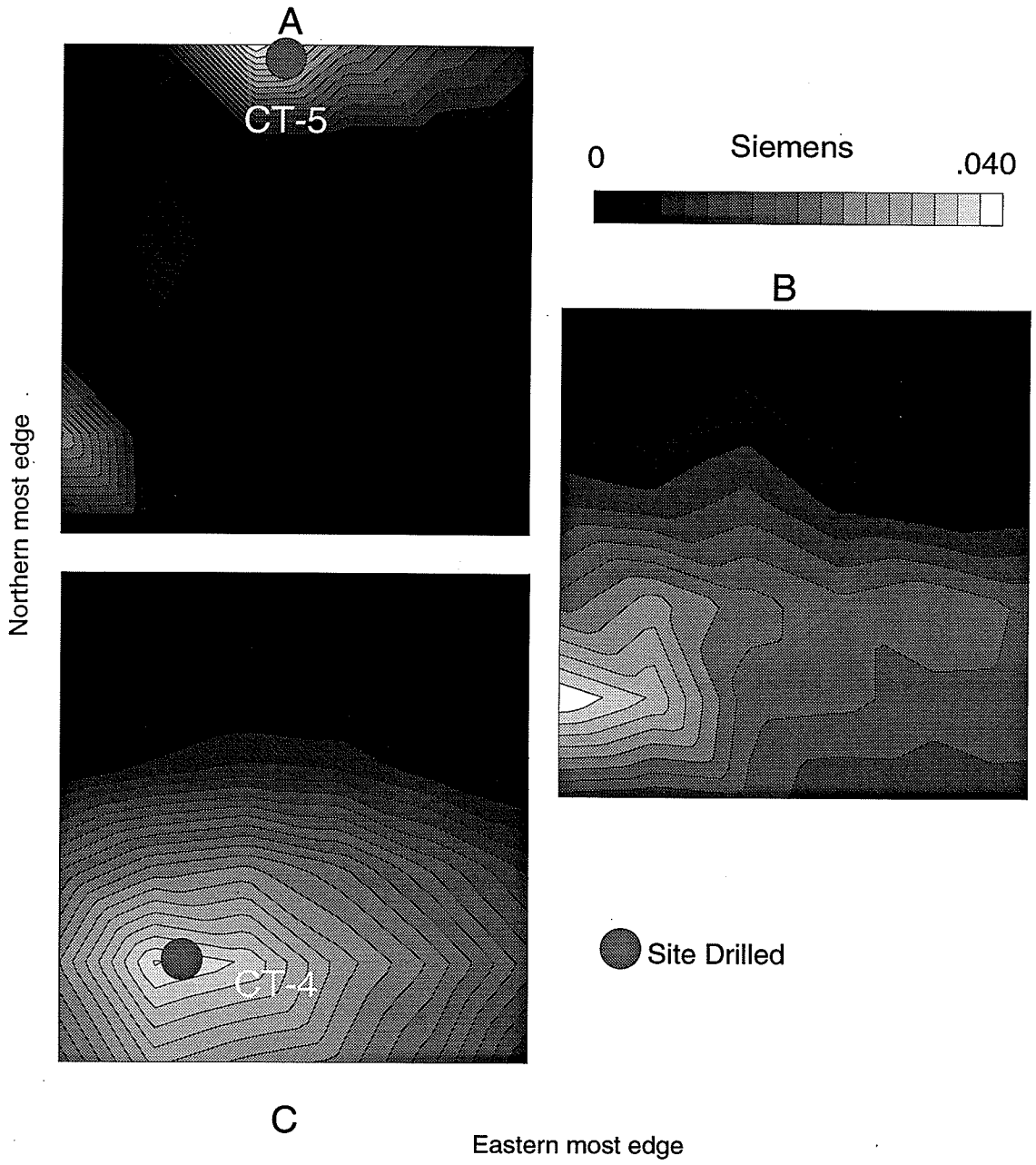

Figure 6.19: Result from detailed survey. Result from a 1.5m electrode spacing. Figure 6.19A shows the 0.00-1.00m level, located at 0.5m, Figure 6.19B shows the 1.00-2.00m level, located at 1.5m, and Figure 6.19C shows the 2.00-3.00m level located at 2.5m. Several distinct targets are apparent and locations marked were selected as drilling targets.

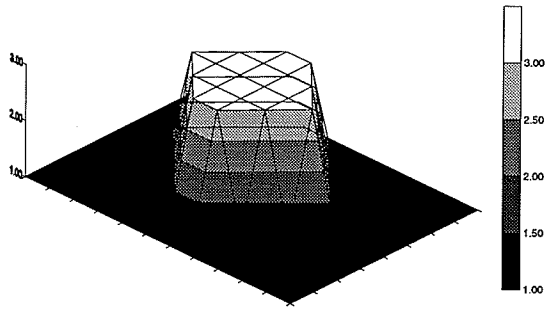

Figure 6.20: The synthetic barrel. The centre two of four cross-sections were as illustrated here. The top and bottom cross-sections were homogeneous at background level.

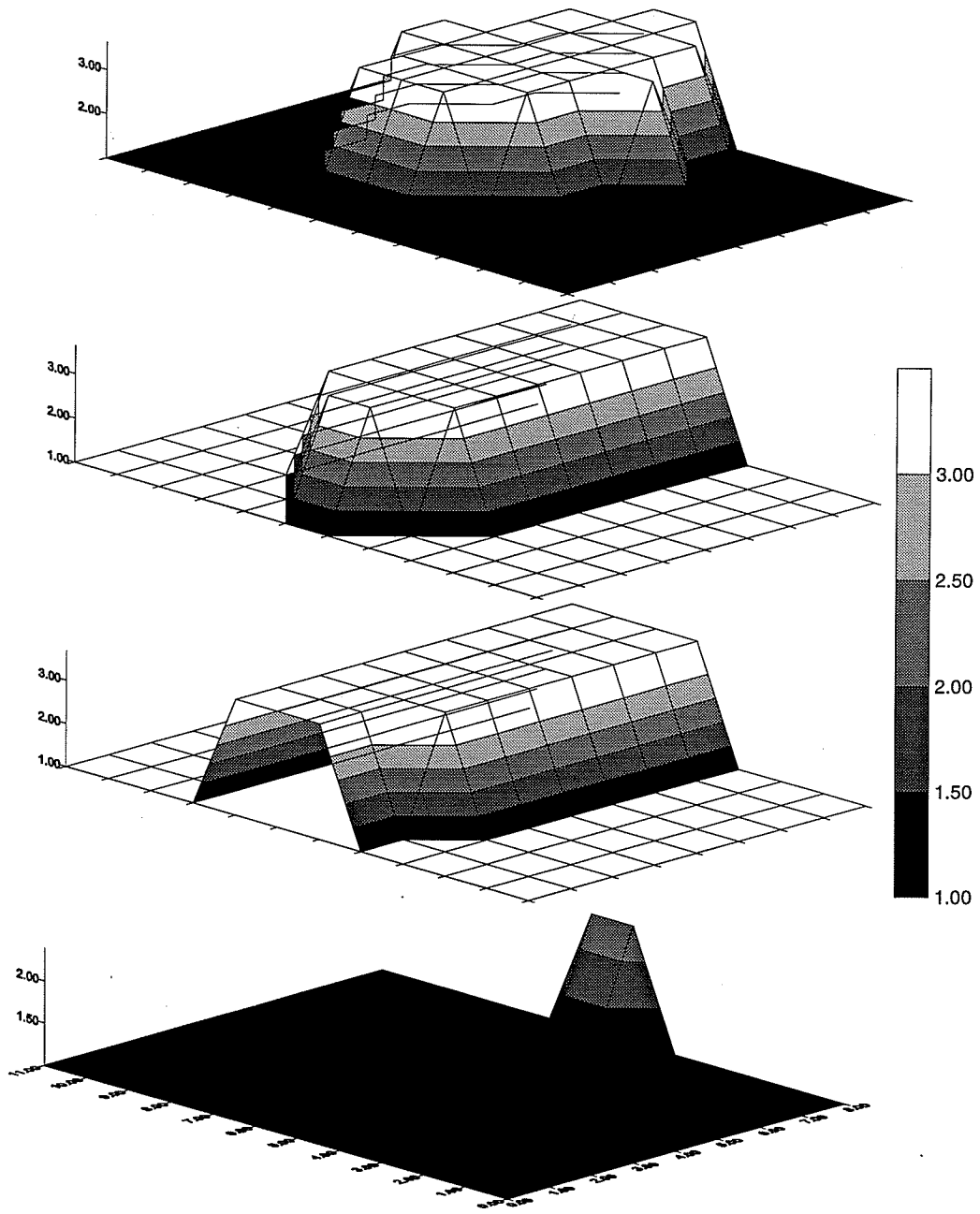

Figure 6.21: Recovering a synthetic barrel. The synthetic model is shown in Figure 6.20. For this result, there were 780 unknowns, 38 excitation pairs, 20 electrodes, and a homogeneous initial conductance of 1 was used.

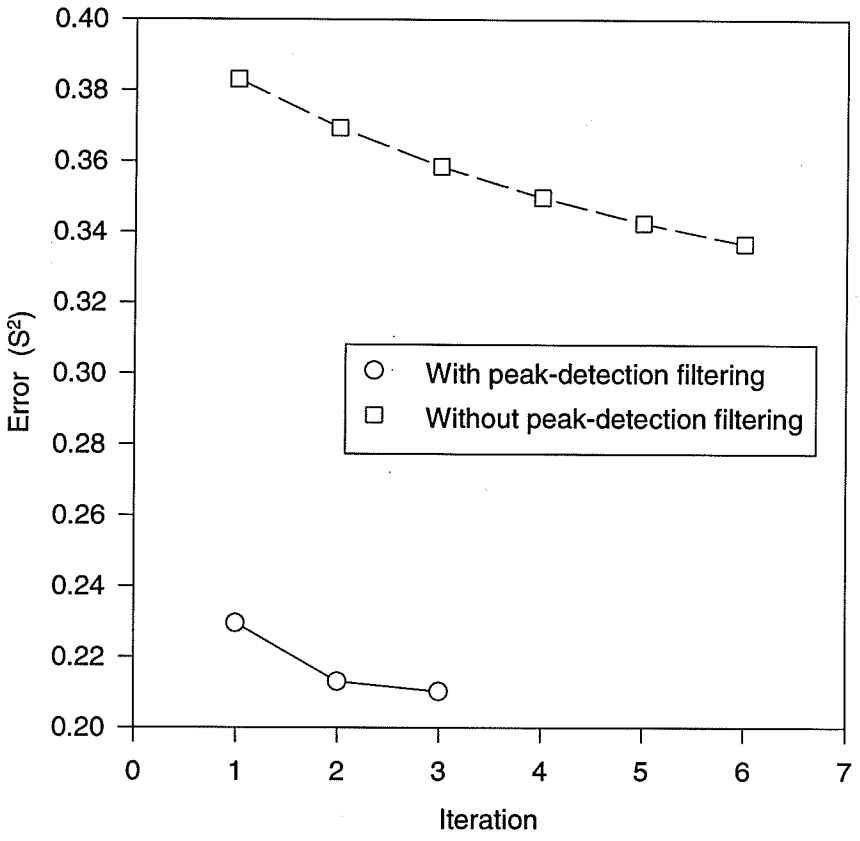

Figure 6.22: Errors in synthetic barrel.

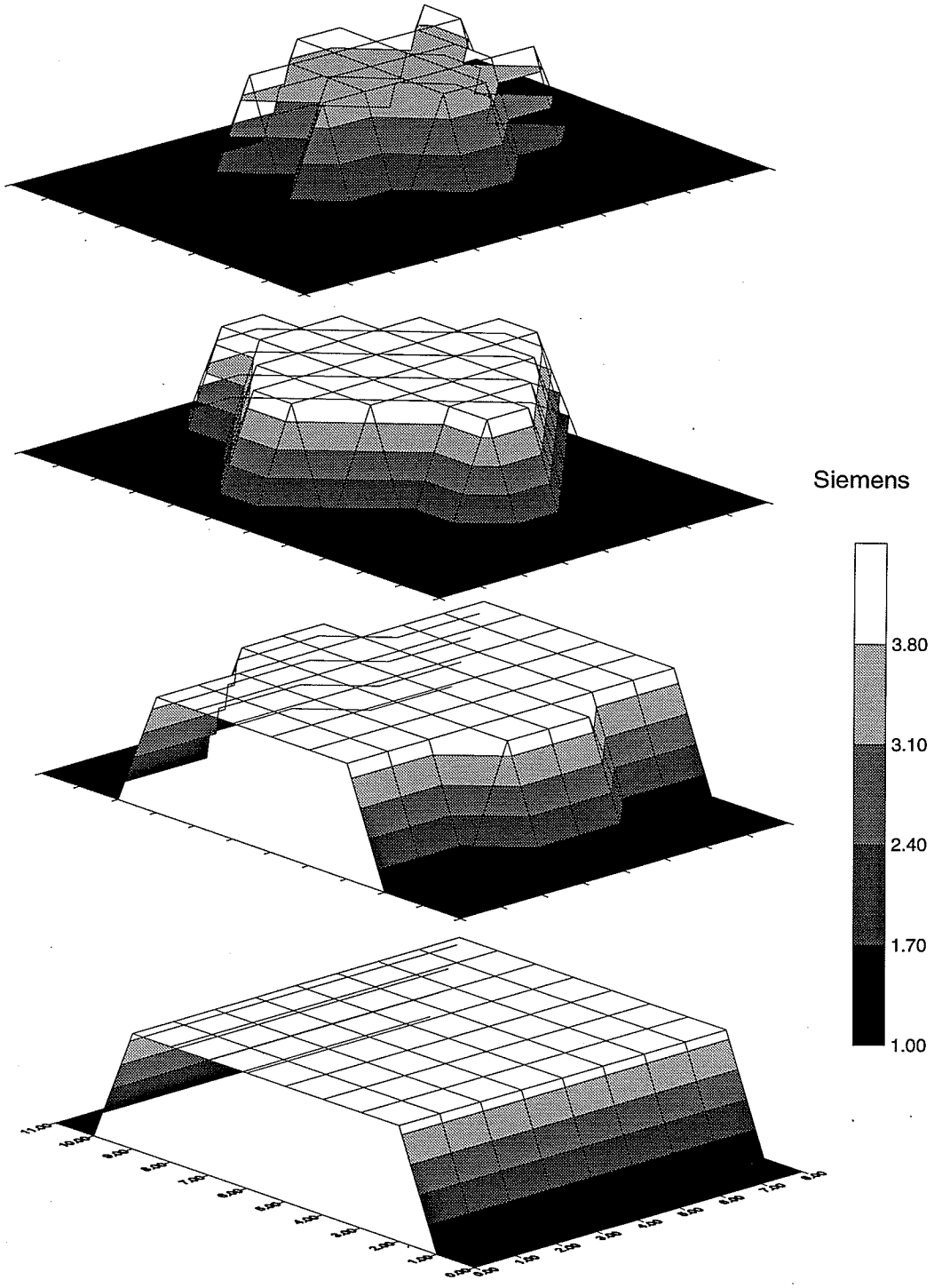

Figure 6.23: Result for barrel and peak-detection filtering. For this result, there were 780 unknowns, 38 excitation pairs, and 20 electrodes.

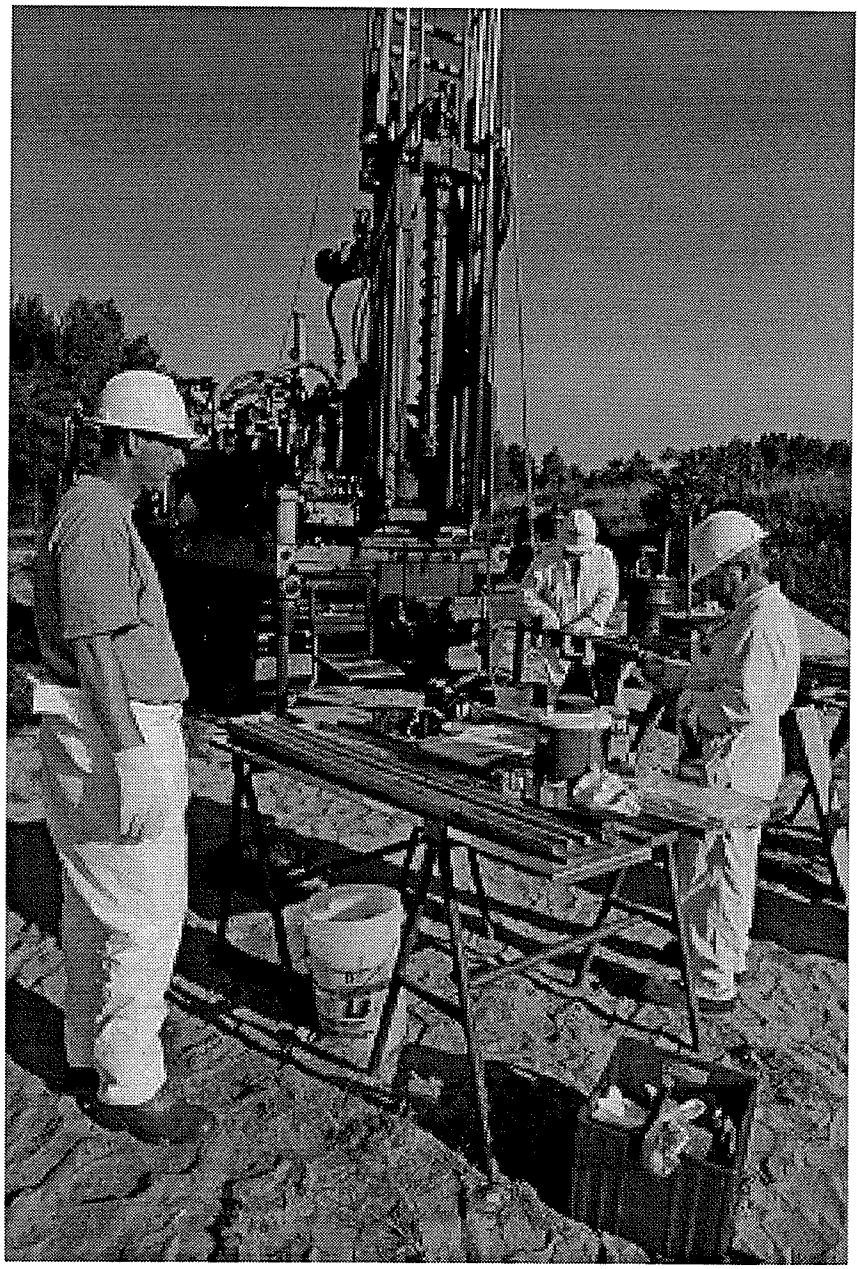

Figure 6.24: Invasive sampling activities. Drilling was performed, coordinated with ERT monitoring.

Chapter 7

Discussion

7.1 Overview

Chapter 7 reviews and discusses the result of this dissertation research while considering the goals summarized in Table 1.1. The research shows the ERT method offers many valuable features to the application of characterization radioactive waste management facilities for remediation. In Section 7.3, other potential applications for the technology are discussed.

7.2 Discussion of Dissertation Research

Chapter 1 provided an overview of the ERT method and reviewed successful demonstrations in environmental applications. The prospects for applying it for remediation of sites contaminated with radioactive waste were presented. The focus of this dissertation was on this application of the ERT method. Chapter 2 continued with background on the algorithm of Wexler, the approach used to process the data in this research.

Chapter 3 discussed previous research designed to speed convergence of the algorithm of Wexler, and points out the limitations of that work. The discussion provided the background and led into the developments of this dissertation research that accelerated the process. The unstable and slow convergence properties of the algorithm are discussed: many iterations were required in recovering the conductance. While peak-detection filtering enhanced contrasts, even as soon as the first iteration, synthetic data showed that objects recovered were not very distinct. Images usually had irregular edges and did not reach exact values.

Chapter 4 outlined a novel multistep method for accelerating iterative processing to convergence and applied it to the algorithm of Wexler. Tests were performed with synthetic data in two and three dimensions, and with filtering. The method improved on the unmodified algorithm by two orders of magnitude when inverting field data.

Chapter 5 developed and applied a robust data-acquisition system in an underground test in a borehole to monitor moisture flow in buffer. The system functioned well over two years. The electronics had self-diagnostic features and the result could be communicated to a controlling computer. It was low cost, easy to use, and conveniently deployed in the field setting.

Chapter 5 went on to apply the ERT method in a two-dimensional study during laboratory and field tests. Moisture levels were monitored in a sand filled apparatus while injecting water. The progress of the water front is clearly discernible in the result. In *in situ* studies at the URL moisture flow was monitored in a borehole filled with buffer, over a period of two years. The result was compared with invasive measurements made using psychrometer moisture sensors. Electrical properties of buffer were modelled to demonstrate the conductance-moisture content relationship and to derive the calibration relationship between the moisture and conductance. The known emplacement moisture level of the material and the calibration developed as part of this study allowed a quantitative analysis for the moisture distributions.

In the research of Chapter 6, the ERT method was deployed in a low-level radioactive waste management area to locate trench boundaries and individual targets. The survey was performed in three dimensions where measurements were taken with sensors placed on the surface. A preliminary test successfully imaged a metal barrel in vertical and tilted orientations. The barrel could be clearly distinguished, although the direction of the tilt was not well discerned. There was a lack of distinctness in the conductance, degrading with increasing depth, and an artifact was apparent below the target. This latter feature, while undesirable, is an affect of the target made more substantial by increasing the distance from

the electrodes.

The result of this dissertation research showed the ERT method to be a valuable tool for environmental remediation. The method complimented the other activities; for example, drilling in the case of the Waste Management Area–C work. In ease of application, it was found to be somewhere between methods with no instrument installation concerns, such as ground-penetrating radar, and invasive methods that require extensive modifications, such as with cross-hole seismic tomography. The ERT method required electrode contact to the ground and this is what made it of intermediate difficulty in terms of instrumenting.

Overall, the ERT method proved very useful in this study. Of particular value are its multi-dimensional and remote sensing features. Quality results are possible without having to modify the subject with instrumentation in an invasive manner. This makes the method safer for deployment at the contaminated sites and in the programs discussed during this dissertation.

7.3 Discussion of Future Research

Three-Dimensional Buffer Studies: The ERT method would be useful during a full-scale, *in situ* multi-component tests to study the interaction between different elements in disposing nuclear fuel waste. This application is more complex than the application of ERT performed at the URL and would require an analysis in three dimensions. This application would need to consider other complicating factors such as the effect of temperature and hydraulic gradients.

Moisture in Rock: Moisture measurements in massive rock and rock fractures are also being considered for ERT methods. This is important to the NFWMP and the study of the performance of the geosphere since fractures are the principle path for groundwater flow. Studies have shown that the resistivity of saturated *in situ* granite varies with the moisture content [98]. This relationship is a direct result of changes to structure caused by stress closure of micro-cracks leading to a decrease in porosity. Since micro-crack moisture

dominates the total volume of water in the rock, an increase in micro-crack volume is associated with an increase in moisture and a decrease in resistivity. Trends can be interpreted based on this relationship [98].

To consider applying the ERT method to monitor moisture in massive rock, existing data were used to image the rock walls of the URL borehole. An conductance distribution in the rock was produced by extending the finite element mesh outwards by 0.104m and then reprocessing the data on this new mesh. Since no calibration of the ERT method in granite was done, it was possible only to correlate conductance contrasts in the rock with regions of apparent moisture in flow determined from the other results.

Figure 7.1 is a contour plot of the conductance distribution throughout the borehole and the rock wall. The conductance of the buffer is high relative to the rock and dominates the result. The natural log of the conductance was plotted to preferentially amplify the lowest conductance values and to bring out the detail of the granite wall. There is a periodic response around the edge of the borehole that appears to be associated with the electrodes. This is interpreted as an artifact of the processing, based on the period of the response and on the results of other studies [88].

There is a contrasting conductance high in the wall in the lower left quadrant of the plot that correlates with a moisture high in the buffer. This also correlates to the position of an open borehole. It appears that this borehole is a channel for moisture flow into the buffer. Until careful laboratory tests have been conducted on samples of granite, the result of Figure 7.1 cannot be interpreted definitively. They do suggest a relationship between the porosity of granite and electrical conductance.

Displaying Data: The display of three-dimensional data is a difficult problem. Computer monitors and paper copies project the result onto a two-dimensional plane and do not fully capture the third dimension. Computers allow interactive, real-time manipulation of the image that can be useful, but this does not translate well to publications. Three-dimensional ERT is a useful application to deal with this issue.

Long-Term Monitoring of Moisture Barriers: The ERT method has the potential to be used to monitor moisture barriers in waste management systems over longer periods of time—even over several decades. Because of its remote sensing properties, it provides broad and distributed coverage in contrast to point readings of more conventional approaches. It can detect changes across surfaces and within volumes that would indicate the movement of moisture as in the event of the failure of a barrier. Because of the robust nature of the data-acquisition hardware, permanent and distributed installations of the ERT method are practical for long periods.

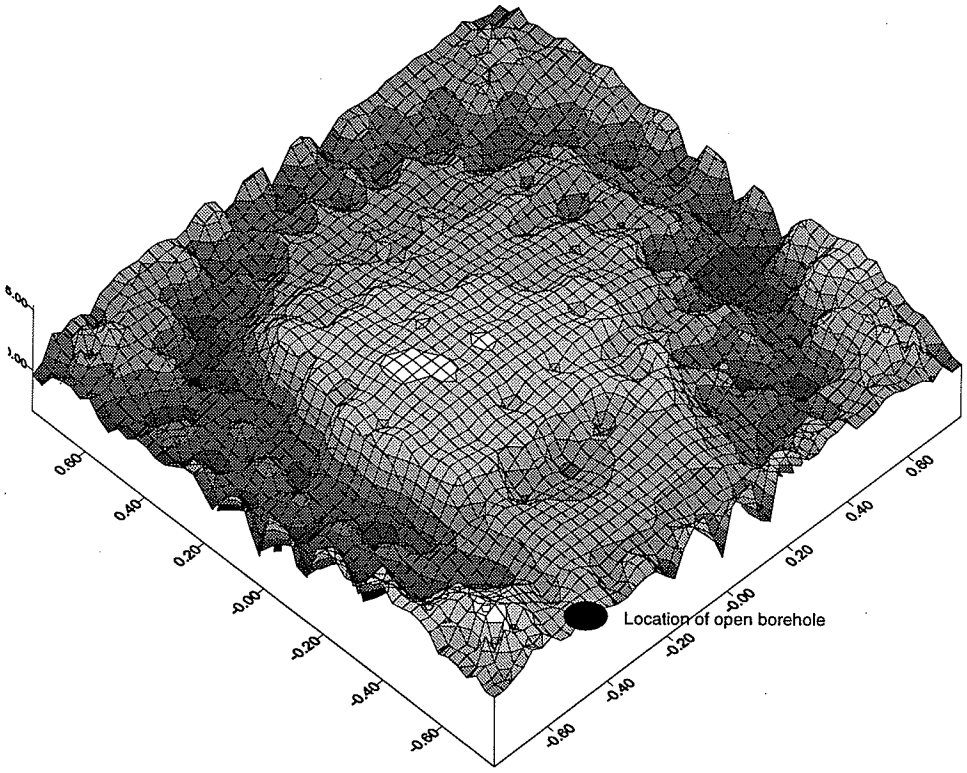

Figure 7.1: Result from the borehole wall. The log of the conductance is plotted. The region within the inner circle is the buffer while the rock lies between the inner and outer circles. Beyond the outer circle, values are extrapolated not considered valid. There were 289 unknowns, 20 excitation pairs, 32 electrodes, and a homogeneous initial resistivity of 10^{-6} was used. The processing was executed for 150 iterations.

References

[1] Environmental impact statement on the concept for disposal of Canada's nuclear fuel waste. AECL Report AECL–10711, COG–93–1, Atomic Energy of Canada Limited, 1994.

[2] Summary of the environmental impact statement on the concept for disposal of Canada's nuclear fuel waste. AECL Report AECL–10721, COG–93–11, Atomic Energy of Canada Limited, 1994.

[3] C.J. Allan, B.R. Gray, and P.D. Stevens-Guille. Canadian high-level radioactive waste management system issues. In *Proceedings of the International High-Level Radioactive Waste Management Conference*, Las Vegas, NV, 1992. American Nuclear Society.

[4] G.E. Archie. The electrical resistivity log as an aid in determining some reservoir characteristics. *Trans. A.I.M.E.*, 146:54–62, 1942.

[5] D.C. Barber, B.H. Brown, and I.L. Freeston. Imaging spatial distributions of resistivity using applied potential tomography. *Electron. Lett.*, 19(22):933–935, 1983.

[6] Chilton B.D. and H.A. Pfuderer. Overview of cleanup and treatment of radioactively contaminated sites. *Nuclear Safety*, 30(4):519–533, 1989.

[7] J.G. Berryman. *Lecture Notes on Electrical Impedance Tomography.* Lawrence Livermore National Laboratories, 1992. Pre-print of lecture notes.

[8] P.R. Bevington. *Data Reduction and Error Analysis for the Physical Sciences.* McGraw-Hill Publishing Company, Toronto, ON, 1969.

[9] W.H. Beyer. *CRC Standard Mathematical Tables.* CRC Press, Boca Raton, FL, 1979.

[10] D.H. Brown, D.C. Barber, W. Wang, L. Lu, A.D. Leathard, R.H. Smallwood, A.R. Hampshire, R. Mackay, and Hatzigalanis. Multi-frequency imaging and modelling of respiratory related impedance changes. *Physiological Measure*, 15(2A):A1–A12, 1994.

[11] J.H. Campbell, N.D. Harris, F. Zhang, B.H. Brown, and A.H. Morice. Clinical applications of electrical impedance tomography in the monitoring of changes in intrathoracic fluid volumes. *Physiological Measure*, 15(2A):A101–A106, 1994.

[12] Canadian Nuclear Society. *Strategy for the disposal of low- and intermediate-level Radwastes in Canada*, Ottawa, ON, 1981.

[13] D.H. Charlesworth. Current development programs for the disposal of low- and intermediate-level radioactive wastes. Technical Report AECL–6545, Atomic Energy of Canada Limited, 1979.

[14] Civil Engineering Department, Colorado State University. *On-site remedial actions at harardous waste disposal sites*, Fort Collins, CO, Feburary 1-3 1984. Sixth Symposium on Uranium Mill Tailings Management.

[15] N.A.C. Cressie. *Statistics for Spatial Data.* John Wiley & Sons, Inc., New York, NY, 1991.

[16] W.D. Daily, W. Li, and T. Buscheck. Hydrological properties of topopah spring tuff: Laboratory measurements. *Journal of Geophysical Research*, 92(B8):7854–7864, 1987.

[17] W.D. Daily and E. Owen. Cross-borehole resistivity tomography. *Geophysics*, 56:1228–1235, 1991.

[18] W.D. Daily, A.L. Ramirez, D. LaBrecque, and W. Barber. Electrical resitivity tomography experiments at the Oregon Graduate Istitute. *Journal of Applied Geophysics*, 33:227–237, 1995.

[19] W.D. Daily, A.L. Ramirez, D. LaBrecque, and J. Nitao. Electrical resitivity tomography of vadose water movement. *Water Resources Research*, 28:1429–1442, 1992.

[20] Y. Das, J.E. McFee, and R.H Chesney. Determination of depth of shallowly buried objects by electromagnetic induction. *IEEE Transactions on Geoscience and Remote Sensing*, GE-23(1):60–66, 1985.

[21] Y. Das, J.E. McFee, J Toews, and G.C. Stuart. Analysis of an electromagnetic induction detector for real-time location of buried objects. *IEEE Transactions on Geoscience and Remote Sensing*, 28(3):278–288, 1990.

[22] P.A. Davis, R. Zach, M.E. Stephens, G.A. Amiro, G.A. Bird, J.A.K. Reid, M.I. Sheppard, S.C. Sheppard, and M. Stephenson. The disposal of Canada's nuclear fuel waste: the biosphere model, BIOTRAC, for post-closure assessment. AECL Report AECL–10720, COG–93–10, Atomic Energy of Canada Limited, 1993.

[23] C.C. Davison, A. Brown, M. Everitt, M. Gascoyne, E.T. Kozak, G.S. Lodha, C.D. Martin, N.M. Soonawalla, D.R. Stevenson, G.A. Thorne, and S.H. Whitaker. The disposal of Canada's nuclear fuel waste: Site screening and evaluation technology. AECLRreport AECL–10713, COG–93–3, Atomic Energy of Canada Limited, 1994.

[24] A. Dey and H.F. Morrison. Resistivity modelling for arbitrary shaped three-dimensional structures. *Geophysics*, 44(4):753–780, 1979.

[25] A.M. Dijkstra, B.H. Brown, N.D. Harris, D.C. Barber, and D.L. Edbrooke. Review: clinical applications of electrical impedance tomography. *Journal of Medical Engineering Technology*, 17(3):89–98, 1993.

[26] K.A. Dines and R.J. Lytle. Analysis of electrical conductivity imaging. *Geophysics*, 47(7):1025–1036, 1981.

[27] D.A. Dixon, S.L. Campbell, and D.S.J. Hnatiw. Preplacement quality control and as-placed properties of the buffer materials used in the URL Isothermal Buffer Experiment. Technical Record TR–612, COG–94–35, Atomic Energy of Canada Limited, 1994.

[28] D.A. Dixon, D.S.J. Hnatiw, and C.L. Kohle. Preparation and quality control of materials used in the reference buffer material. Technical Record TR–575, COG–92–133, Atomic Energy of Canada Limited, 1992.

[29] D.F. Dixon and D.H. Charlesworth. Disposal of low- and intermediate-level radwastes in Canada. *Transactions of the American Nuclear Society*, 34:113–121, 1980.

[30] R.T. Droege and R.L Morin. A practical method to measure the MTF of CT scanner. *Medical Physics*, 9(5):758–760, 1982.

[31] I.S. Duff and J.K. Reid. The multifrontal solution of unsymmetric sets of linear equations. *SIAM Journal of Scientific Statistical Computing*, 5(3), 1984.

[32] B. Eklund and J. Summerhays. Procedures for estimating emissions from the cleanup of superfund sites. *Journal of Air Waste Management Association*, 40(1):17–23, 1990.

[33] R.G. Ellis and D.W. Oldenburg. The pole-pole 3D DC resistivity inverse problem: A conjugate gradient approach. *Journal of Air Waste Management Association*, 40(1):17–23, 1994.

[34] Environmental and Engineering Geophysical Society. *Tracking Fluid Flow in the Saturated zone using cross-borehole resistivity and IP*, Englewood, CO, April 1993. Symposium on the Application of Geophysics to engineering and environmental problems.

[35] D. Fishlock. The dirtiest place on earth. *New Scientist*, 19–February–1994:34–37, 1994.

[36] M. Fogiel. *The Essentials of Numerical Analysis II.* Research and Education Association, New York, NY, 1988.

[37] B. Fry. A Resistive Tomographic Algorithm. Master's thesis, University of Manitoba, Winnipeg, MB, 1983.

[38] F.C. Gerald and P.O. Wheatly. *Applied Numerical Analyses.* Addison-Wesley Publishing Company, Inc., Don Mills, ON, 3^{rd} edition, 1984.

[39] P.W. Gonzalez and P. Wintz. *Digital Image Processing.* Addison-Wesley Publishing Company, Inc., Don Mills, ON, 6^{th} edition, 1983.

[40] J. Graham, B.E. Lingnau, D.S. Yarechewski, and N. Tanaka. Thermo-elastic-plastic modelling of sand bentonite buffer for use in underground disposal of nuclear fuel waste. Progress record, University of Manitoba, Winnipeg, MB, 1993. Contract number WS–30J–79981.

[41] D.D. Hardy and D.F. Dixon. The transition from storage to permanent disposal of low- and intermediate-waste at the Chalk River Nuclear Laboratories. *Waste Management '85*, 1985.

[42] X. He and S. Zhou. A reconstruction algorithm for electrical impedance tomography. *IEEE Annual Conference of Engineering in Medical and Biological Society*, pages 1686–1688, 1992.

[43] E. Hinton and D.R.J Owen. *Finite Element Programming.* Academic Press, New York, NY, 1977.

[44] E. Hinton and D.R.J Owen. *An Introduction to Finite Element Computations.* Pineridge Press Limited, Swansea, UK, 1979.

[45] P. Hood. Frontal solution program for unsymmetric matrices. *International Journal for Numerical Methods in Engineering*, 10(2), 1976.

[46] K.H. Huebner. *The Finite Element Method for Engineers.* John Wiley & Sons, Inc., New York, NY, 1975.

[47] International Conference: Security through Science and Engineering. *Advances in magnetic resonance for the detection of bulk explosives*, Technical University Berlin, September 23-26 1980.

[48] B.M. Irons and N. Shrive. *Finite Element Primer.* John Wiley & Sons, Inc., Toronto, ON, 1983.

[49] A.G. Journal and CH.J. Hiujbregts. *Mining Geostatistics.* Academic Press, New York, NY, 1978.

[50] Y. Kim, J.G. Webster, and W.J. Tompkins. Electrical impedance imaging of the thorax. *Journal of Microwave Power*, 18:245–257, 1983.

[51] R.V. Kohn and M. Vogelius. Relaxation of a variational method for impedance computed tomography. *Comm. Pure and Applied Math*, 40:745–777, 1987.

[52] G.A. Kyriacou, C.S. Koukourlis, and J.N. Sahalos. A reconstruction algorithm of electrical impedance tomography with optimal configuration of the driven electrodes. *IEEE Transactions on Medical Imaging*, 12(3):430–438, 1993.

[53] G.A. Kyriacou, C.S. Koukourlis, J.N. Sahalos, and K. Batas. Reconstruction of impedance images using a modified perturbation method. *Clin. Phys. Physiol. Meas.*, 13(Suppliment A):91–94, 1992.

[54] D. LaBrecque, M. Michela, B. Daily, A. Ramirez, and Owen E. The effect of noise on OCCAM's inversion of resistivity tomography data. *Unpublished*, 1995.

[55] D. LaBrecque, G. Morelli, B. Daily, A. Ramirez, and P. Lundegard. OCCAM's inversion of 3D ERT data. *Geophysics*, 1995.

[56] T.W. Lambe and R.V. Whitman. *Soil Mechanics.* John Wiley & Sons, Inc., Toronto, ON, 1969.

[57] N.T. Lan, P. Chaigne, A. Philippe, and R. Ambrosino. Experimentation d'une methode capacitive pour l'evaluation de l'humidite des sols. *Bulletin de Liaison des Laboratoires des Ponts et Chaussees*, 60:155–165, 1972.

[58] L. Leithold. *The Calculus: With Analytical Geometry. Part I, Functions of One Variable, Plane Analytic Geometry, and Infinite Series.* Harper & Row, New York, NY, 3^{rd} edition, 1976.

[59] W. Lin and W. Daily. Transport properties of topopah spring tuff. Technical Report UCRL-53602, Lawrence Livermore National Laboratory, Livermore, CAL, 1984.

[60] R.L. Mackie and T.E. Madden. Three-dimensional magnetotelluric inversion using conjugate gradients. *Geophysics Journal International*, 115:215–229, 1993.

[61] E.T. McAdams, J.A. McLaughlin, and J.C. Anderson. Multi-electrode systems for electrical impedance tomography. *Physiological Measure*, 15(2A):A101–A106, 1994.

[62] S.J. McAuley and D. Grondin. A safety and hazards analysis of the Chalk River Laboratories waste management areas. Technical Record AECL–MISC–306 (Draft), Atomic Energy of Canada Limited, 1993.

[63] J.E. McFee and Y. Das. The detection of buried explosive objects. *Canadian Journal of Remote Sensing*, 6(2), 1980.

[64] J.E. McFee and Y. Das. Advances in the location and identification of hidden explosive munitions. Unclassified Suffield Report No. 548, Defence Research Establishment Suffield, 1991.

[65] Z. Mu. *Electrical Impedance Computed Tomography—Algorithms and Systems.* PhD thesis, University of Manitoba, Winnipeg, MB, 1994.

[66] Nuclear Associates: Division of Victoreen Inc., 100 Voice Road, Carle Place NY 11514. *Instruction Manual: Computerized Tomography Performance Phantom*, 1^{st} edition, 1980.

[67] K.E. Philipose. Waste management area "c" extension—a submission to the SRC and AECB for construction and approval. AECL Report AECL-MISC-386, Atomic Energy of Canada Limited, 1993.

[68] S.J. Phillips, J.F. Relyea, R.R. Seitz, and J.W. Cammann. Development and assessment of closure technology for liquid-waste disposal sites. In R.H. Gray, editor, *Environmental Monitoring Restoration and Assessment: What have we learned?*, Richland, WA, 1990. United States Department of Energy.

[69] W.H. Press, B.P. Flannery, S.A. Teakolsky, and W.T. Vetterling. *Numerical Recipes in C: The Art of Scientific Computing.* Cambridge University Press, New York, NY, 1988.

[70] A.L. Ramirez, W. Daily, and D. LaBrecque. Electrical resistance tomography used in environmental restoration. In *Meeting on characterization monitoring and sensor technologies*, Dallas, TX, 1992. U.S. Departmant of Energy.

[71] A.L. Ramirez and W.D. Daily. Geotomography of grout penetration in fractured granite. *International Journal on Rock Mechanics*, 27:57–63, 1990.

[72] A.L. Ramirez, W.D. Daily, D. LaBrecque, E. Owen, and D. Chesnut. Monitoring an underground steam injection process using electrical resistance tomography. *Water Resources Research*, 29(1):73–87, 1993.

[73] A. Rose. The sensitivity of the human eye on an absolute scale. *Journal of the Optical Society of America*, 38(2):196–208, 1948.

[74] F. Scheid. *Theory and Problems of Numerical Analysis.* McGraw-Hill, Toronto, ON, 2^{nd} edition, 1989. Schaum's Outline Series.

[75] Jandel Scientific. Tablecurve^{TM}, 1991.

[76] G.R. Simmons. Atomic Energy of Canada Limited's Underground Research Laboratory for Nuclear Waste Management. Technical Report AECL–9283, Atomic Energy of Canada Limited, 1987.

[77] G.S. Strobel. Frontal solvers and the FPS M64-series machines. Paper presented to the ARRAY Conference on Supercomputing, Dallas, TX, 1987.

[78] G.S. Strobel. Options for solving sparse matrices on FPS M64-series super-computers: comparison of benchmark times and resource requirements. Paper presented to the ARRAY Conference on Supercomputing, Portland, OR, 1988.

[79] G.S. Strobel. Impedance-computed tomography for monitoring moisture content in clay-based buffer. Technical Record TR–586, COG–92–391, Atomic Energy of Canada Limited, 1993.

[80] G.S. Strobel. Evaluation and interpretation of impedance-computed moisture content measurements. AECL Report AECL–11190, COG–94–493, Atomic Energy of Canada Limited, 1994.

[81] G.S. Strobel. Measurements of resistive and capacitive properties of a sand/bentonite clay mixture. Technical Report AECL–10668, COG–92–195, Atomic Energy of Canada Limited, 1994.

[82] G.S. Strobel. A method for fitting multiple sets of noncoincidental stochastic data. Technical Record TR–450, COG–94–468, Atomic Energy of Canada Limited, 1994.

[83] G.S. Strobel. A prototype impedance-computed tomographic data acquisition system. Technical Record TR–624, COG–93–462, Atomic Energy of Canada Limited, 1994.

[84] G.S. Strobel. Resistivity-water content relationship of a sand/bentonite clay mixture. Technical Record TR–600, COG–93–90, Atomic Energy of Canada Limited, 1994.

[85] G.S. Strobel. Review of the preliminary YMP-ESF ERT tests. Technical report, Atomic Energy of Canada Limited, 1996. Prepared for the U.S. Department of Energy under contract DE-AC08-95NV11784.

[86] G.S. Strobel. Buffer response to alternating-current excitation. Technical record, Atomic Energy of Canada Limited, in preparation.

[87] G.S. Strobel. An impedance-computed tomographic data acquisition system. Technical record, Atomic Energy of Canada Limited, in preparation.

[88] G.S. Strobel. A study of the performance of two electrical impedance imaging algorithms of type Kohn-Vogelius-Wexler. Technical record, Atomic Energy of Canada Limited, in preparation.

[89] G.S. Strobel. Test results on a alternating-current source for impedance measurements. Technical record, Atomic Energy of Canada Limited, in preparation.

[90] G.S. Strobel, P.J. Chernis, A.T. Bushman, M.H. Spinney, and R.J. Backer. Monitoring and information management system at the Underground Research Laboratory. In *The deep geological disposal of nuclear fuel waste*, Winnipeg, MB, September 1996. Canadian Nuclear Society.

[91] G.S. Strobel and R. Donders. Electrical resistivity tomography for support of WMA–C closure—request for funds for 1995/96 fiscal year. Internal memo, 1995.

[92] G.S. Strobel, R.E. Donders, and S. Welch. Demonstration of electrical resistivity tomography in low-level Waste Management Area–C closure. Technical Record TR–732, Atomic Energy of Canada Limited, 1996.

[93] G.S. Strobel and H.S. Spinney. A personal-computer data acquisition system at the URL. AECL Report AECL–637, COG–94–203, Atomic Energy of Canada Limited, 1994.

[94] G.S. Strobel, A.A.L. Wan, and N.A. Chandler. Comparison of impedance and psychrometer moisture results from the Isothermal Test. Technical record, Atomic Energy of Canada Limited, in preparation.

[95] G.S. Strobel, A. Wexler, and Z. Mu. Remote sensing water content in a clay/sand mixture using impedance-computed tomography. In *Proceedings of the Conference on Antanae Technology*, Winnipeg, MB, 1992.

[96] A. Tamburi, U. Roeper, and A. Wexler. An application of impedance-computed tomography to subsurface imaging of pollution plumes. *American Society for Testing and Materials*, Special Technical Publication STP963:86–100, 1987.

[97] W.M. Telford, L.P. Geldart, R.E. Sheriff, and D.A. Keys. *Applied Geophysics.* Cambridge University Press, Cambridge, UK, 1976.

[98] S. Tomecka-Suchon and F. Rummel. Fracture-induced resistivity changes in granite. *Int. J. Rock Mech. Min. Sci. & Geomech.*, 29(6):583–587, 1992.

[99] A.P. Toste, L.J. Kirby, D.E. Robertson, K.H. Abel, and R.W. Perkins. Characterization of radionuclide behavior in low-level waste sites. *IEEE Transactions on Nuclear Science*, NS-30(1):580–585, 1983.

[100] P.E. Wannamaker, J.A. Stodt, and L. Rijo. Pw2d finite element program for solution of megnetotelluric responses of two-dimensional Earth resistivity structure. Technical Report Rep. ESL-158, Earth Sci. Lab., Univ. of Utah, 1987.

[101] Westinghouse. Demonstration of innovative monitoring technologies at the savannah river integrated demonstration site. Technical report, Westinghouse Savannah River Company, 1993. Prepared for the U.S. Department of Energy under contract DE-AC09-89SR18035.

[102] A. Wexler. Electrical impedance imaging in two and three dimensions. In *Clinical Physics and Physiological Measurement*, volume 9-A, pages 29–33, Lyon, FR, 1988.

[103] A. Wexler and B. Fry. Reconstruction system and methods for impedance imaging, 1982. Patent 1196691 (Canada) and 4539640 (US).

[104] A. Wexler and B. Fry. Method and apparatus for imaging the interior of a structure, 1983. Patent 0085490 (Europe).

[105] A. Wexler, B. Fry, and M.R. Neuman. Impedance-computed tomography algorithm and system. *Applied Optics*, 24:3985–3992, 1985.

[106] E.D. Wright (editor). Semi-annual status report of the Canadian Nuclear Fuel Waste Management Program 1986 October 1 – 1987 March 31. Technical Record TR–425–2, Atomic Energy of Canada Limited, 1987.

[107] T.J. Yorkey. *Comparing reconstruction methods for electrical impedance tomography.* PhD thesis, University of Wisconsin, Madison, WI 53706, 1986.

[108] T.J. Yorkey, J.G. Webster, and W.J. Tompkins. Comparing reconstruction algorithms for electrical impedance tomography. *IEEE Transactions in Biomedical Engineering*, 34:843–852, 1987.

[109] J. Zhang, R.L. Mackie, and T.E. Madden. 3-D resistivity forward modeling and inversion uisng conjugate gradients. *Geophysics*, 60(5):1313–1325, 1995.

Appendix A

Mathematical Foundation

The approach to solving the ERT system used in this dissertation is one variant of the double-constraint method referred to as the algorithm of Wexler [7]. Another variant was developed by Kohn and Vogelius [108] and starts by defining the error functional as

$$\varepsilon(\kappa) \equiv \Sigma \int \kappa(\underline{x})^{-1} \mid \underline{J}_i + \kappa(\underline{x}) \nabla \Psi(i) \mid^2 \partial^3 \underline{x} \tag{A.1}$$

where the sum is taken over all observations. In words, the error is the difference between the forward and inverse solutions to the field equations, J and Ψ respectively. Equation A.1 is ≥ 0 for the solution and after expanding and applying the divergence theorem,

$$\varepsilon(\kappa) = \Sigma \int \kappa(\underline{x})^{-1} \mid \underline{J}_i \mid^2 \partial^3 x + \Sigma \int \kappa(\underline{x}) \mid \nabla \Psi_i \mid^2 \partial^3 x - 2 \int \Psi_i \underline{J}_i \cdot \underline{n} \partial a. \tag{A.2}$$

Thompson's variational principle

$$\int \kappa(\underline{x})^{-1} \mid \underline{J}_i \mid^2 \partial^3 x \geq \rho_i \tag{A.3}$$

and Dirichlet's principle

$$\int \kappa(\underline{x}) \mid \nabla \underline{\Psi} \mid^2 \partial^3 x \geq \rho_i \tag{A.4}$$

where $\rho_i = \int \Psi_i \underline{J}_i \cdot \underline{n} \partial a$, both hold for the solution and provide an upper limit to the third term in Equation A.2.

The error functional is minimum when the first two terms of Equation A.2 are minimum. It must be minimized in each region j of the subject,

$$\partial \varepsilon_j / \partial \kappa_j = -\kappa^{-2} \Sigma \int_j \mid \underline{J}_i \mid^2 \partial^3 x + \Sigma \int_j \mid \nabla \Psi_i \mid^2 \partial^3 x = 0. \tag{A.5}$$

Solving Equation A.5 for κ_j,

$$\kappa_j = (\Sigma \int_j \mid J_i \mid^2 \partial^3 x / \Sigma \int_j \mid \nabla \Psi_i \mid^2 \partial^3 x)^{1/2} \tag{A.6}$$

A.1 The Finite-Element Solution of the Field Equations

In this formulation, the inverse problem fits the voltage measurements while the forward problem, using the excitation current, is constrained to fit the voltage measurements and both are solved using the finite element method (FEM). The development of the FEM approach followed the arguments in [37, 43, 44, 46] and used quadratic elements having nine nodes per element in the two-dimensional development and linear elements having eight nodes per element in the three-dimensional development. In the FEM problem, a fit of order r is defined by the relationship $\Phi = \Sigma N_i \Phi_i = [N]\Phi$ where i runs over all nodes, N_i are scalar multipliers and Φ_i are the shape functions. The fit meets requirements for compatibility: C^r continuity at element boundaries, and completeness: properly behaved C^{r+1} functions as the volume of the element goes to zero.

To illustrate[1], linear elements in two-dimensional are used where

$$\Phi(x, y) \simeq \alpha_1 + \alpha_2 x + \alpha_3 y + \alpha_4 xy = [P]\underline{\alpha}, \tag{A.7}$$

$[P] = [1\ x\ y\ xy]$, and $\underline{\alpha} = \alpha_1\ \alpha_2\ \alpha_3\ \alpha_4$. At each node, the field must satisfy

$$\Phi = [G]\underline{\alpha} \tag{A.8}$$

where

$$[G] =$$

$$\begin{matrix} 1 & x_1 & y_1 & x_1 y_1 \\ 1 & x_2 & y_2 & x_2 y_2 \\ 1 & x_3 & y_3 & x_3 y_3 \\ 1 & x_4 & y_4 & x_4 y_4 \end{matrix}$$

[1]The actual development used quadratic fitting for the two-dimensional case

From Equations A.7 and A.8

$$\Phi = ([P][G] - 1)\Phi = [N]\Phi,$$

where $[N] = ([P][G] - 1) \equiv$ the interpolation functions.

Lagrange polynomials are used in this development: $L_k(x) = \Pi^n_{m=0,m\neq k}(x - x_n)/(x_k - x_m)$. For a nine-node element, the Lagrange polynomial is of second order and Φ is $\Phi(x) \simeq \phi(x) = \Sigma^7_{i=0}\phi_i L_i(x) = [L]\phi$. The coefficients for ϕ_i are $L_i(x) = (\Pi_{m\neq i}(x - x_m))/(\Pi_{m\neq i}(x_i - x_m))$. In a local-coordinate system, (x, h), the two-dimensional Lagrange interpolation functions are:

$$\phi(\varepsilon, \eta) = N_1(\varepsilon, \eta)\phi_1 + N_2(\varepsilon, \eta)\phi_2 + N_3(\varepsilon, \eta)\phi_3 + N_4(\varepsilon, \eta)\phi_4 + ...$$

where $N_i(\varepsilon, \eta) = L_i(\varepsilon)L_i(\eta)$.

The FEM functional (I) is determined considering that Laplace's equation, $L\phi = f$ with differential operator $L \equiv \partial^2()/\partial x^2 + \partial^2()/\partial y^2$, holds on the full domain and is known on the boundary where $\phi = f$ (the classical Dirichlet problem). For the classical Dirichlet problem, the variational problem

$$\int_D \delta\phi[L(\phi) - f]\partial D = 0 \tag{A.9}$$

can be written in terms of a newly defined operator $(L*)$,

$$\delta \int_D [L*(\phi) - f\phi]\partial D = 0$$

The functional is

$$\int_D [L*(\phi) - \phi f]\partial D = 0 \tag{A.10}$$

constrained such that $\delta I(\phi) = 0$.

Applying the identity, $\nabla^2 = \nabla \cdot \nabla$, and using the chain rule gives

$$\nabla \cdot (\delta\phi\nabla\phi) = \nabla(\delta\phi) \cdot \nabla\phi + \delta\phi \cdot \nabla^2\phi. \tag{A.11}$$

Equation A.9 is substituted back into Equation A.10 to give

$$\int_D \nabla \cdot (\delta\phi \nabla\phi)\partial D - \int_D \nabla(\delta\phi) \cdot \nabla\phi \partial D = 0.$$

Green's theorem is applied to the first term, with the result that

$$\int_\Sigma \underline{n} \cdot \delta\phi \nabla\phi \delta\sigma - \int_D \nabla(\delta\phi) \cdot \nabla\phi \partial D = 0,$$

where $\delta\sigma$ indicates the integral is performed over the surface. Since the Dirichlet boundary conditions are imposed on the boundary

$$\int_D \nabla(\delta\phi) \cdot \nabla\phi \delta D = 0$$

and

$$\nabla(\delta\phi \cdot \nabla\phi) = 1/2(\nabla\phi \cdot \nabla\phi),$$

hence

$$1/2\delta \int_\Sigma \nabla\phi \cdot \nabla\phi \partial\sigma = 0. \tag{A.12}$$

Substituting Equation A.12 back into Equation A.10 gives the functional for the FEM problem

$$\int_\Sigma \nabla\phi \cdot \kappa \cdot \nabla\phi \partial\sigma - 2 \int f\phi \partial\sigma = 0. \tag{A.13}$$

In the FEM method, the stiffness matrix is assembled from the functional and the shape functions by making the ϕ discrete over the elements, as per the Rayleigh-Ritz approach. The field ϕ is approximated with a set of functions ϕ_i and coefficients α_i

$$\phi \simeq \phi_p = \Sigma_{i=0}^{p} \alpha_i \phi_i(x) = \underline{\phi}^T \alpha = \underline{\alpha}^T \underline{\phi} \tag{A.14}$$

with $lim_{p\to\infty}\phi - \Sigma_{i=0}^{p} \alpha_i \phi_i(x) = 0$. The statement for the discrete stationary condition for the FEM functional, thus determining the α_i's, is

$$\partial I/\partial\alpha_i = 0 \text{ for } i = 1, ..., p. \tag{A.15}$$

Substituting Equation A.15 into Equation A.13 and using the result of Equation A.14, the discrete functional becomes

$$I = [\int_{\Sigma} \nabla\alpha_i \cdot \kappa \cdot \nabla\alpha_i^T \partial\sigma - 2 \int f\alpha_i \partial\sigma\phi \tag{A.16}$$

which, in the minimum with respect to ϕ, is

$$\partial I/\partial\phi = \int_{\Sigma} \nabla\alpha_i \cdot \kappa \cdot \nabla\alpha_i^T \partial\sigma - 2 \int f\alpha_i \partial\sigma = 0. \tag{A.17}$$

To make $I(\phi)$ stationary with respect to the nodal values,

$$\delta I(\phi) = \Sigma(\delta I/\delta\phi_i)\delta\phi_i = 0.$$

This sum is taken over all degrees of freedom for the system, i.e., at each node where a value is to be determined. Since the ϕ_i's are independent for each degree of freedom, $\delta I/\delta\phi_i = 0$ for all degrees of freedom, and hence, $\delta I = \Sigma\delta I^{(e)} = 0$ over all elements. Thus,

$$\delta I^{(e)})/\delta\phi_i = \delta I_i^{(e)}/\delta\phi_j = 0 \tag{A.18}$$

for all nodes associated with element i.

Considering Equation A.17 in the form $[S]\underline{\phi} = \underline{b}$ and using Equation A.18,

$$S_{ij} = \int_{\Sigma} \nabla\alpha_i \cdot \kappa \cdot \nabla\alpha_j \partial\sigma$$

and

$$b_i = 2 \int f\alpha_i \partial\sigma. \tag{A.19}$$

Using the relationship

$$\kappa = \alpha \cdot \kappa = \alpha^T \cdot \kappa$$

Equation A.19 becomes

$$Sij = \kappa \int_{\Sigma} \nabla\alpha_i \cdot \alpha \cdot \nabla\alpha_j \partial\sigma$$

$$= \kappa \int_{\Sigma} \nabla\alpha_{il}(\alpha_{klm}\nabla\alpha_{mj})\partial\sigma$$

and

$$\underline{b}_i = \int_{\Sigma} \alpha_i \alpha_j f_j \partial\sigma. \tag{A.20}$$

If the matrix is assembled in element local coordinates (ζ, η), it must be transformed into the global coordinate system (x, y) using the Jacobian

$$\underline{J} = \begin{matrix} \partial x/\partial\zeta & \partial y/\partial\zeta \\ \partial x/\partial\eta & \partial y/\partial\eta \end{matrix}$$

The inverse of the Jacobian is derived from

$$\partial\phi/\partial x = \partial\phi/\partial\epsilon \cdot \partial\epsilon/\partial x + \partial\phi/\partial\eta \cdot \partial\eta/\partial x$$

and

$$\partial\phi/\partial y = \partial\phi/\partial\epsilon \cdot \partial\epsilon/\partial y + \partial\phi/\partial\eta \cdot \partial\eta/\partial y$$

to give

$$[J]^{-1} = \begin{matrix} \partial\zeta/\partial x & \partial\eta/\partial x \\ \partial\zeta/\partial y & \partial\eta/\partial y \end{matrix}$$

Both the the field and the impedance values are computed at the node points. Both are needed, for assembling the stiffness matrix and to update the impedance in the iterative process. The system of equations generated, is solved using a matrix-solving routine to give the field values at the nodes. The stiffness matrix has certain properties that can be utilized to improve the efficiency of the solver. It is symmetrical since $s_{ij} = s_{ji}$ and banded having width dependent on the order and the geometry of the finite element mesh.

The resolution of the image determines the fineness of the mesh used. The finite-element method is highly flexible in that as much detail can be generated. The cost is additional computing effort but this can be efficiently handled with appropriate solvers [77, 78]. Realistically, detail is limited by the number of measurements since this determines the number of unknowns that can be solved. As in any approximation, an infinite number of values can be determined from the shape functions. However, confidence of detail decreases if there is no corresponding increase in the number of measurements. More electrodes and/or more excitations are needed.

A.2 Numerical Integration using Gaussian Quadrature

To assemble the system of equations of Equation A.1 and Equation A.20, it is necessary to perform numerical integration. Although there are many ways to do this, [9] gaussian quadrature was implemented in this dissertation [74]. On the interval [a,b], the gaussian quadrature takes the form

$$\int_a^b w(\zeta)f(\zeta)\partial\zeta \approx \Sigma_{i=1}^{m} W_i f(\zeta_i) \tag{A.21}$$

where $\zeta \in [a,b]$. The W_i is the wieghting factor for the i^{th} point and m is the number of points used in the sum. The derivation starts by requiring an exact fit when $f(\zeta)$ is one of the power functions: $\{1, x, x^2, ..., x^{2n-1}\}$. This imposes $2n$ conditions for determining the $2n$ numbers ζ_i and W_i, where

$$W_i = \int_b^a w(\zeta)L_i(\zeta)\partial\zeta.$$

The L_i are the Lagrange polynomials [74] and the ζ_i are the roots of the orthogonal polynomials satisfying $\int_b^a w(\zeta)p_n(\zeta)p_m(\zeta)\partial\zeta = 0 m \neq n$. With the interval normalized to $[-1,+1]$, the ζ are symmetrically about zero, zero is in the set for m odd, and symmetrical points are wieghted the same. Equation A.21 can be generalized into n dimensions using the formula

$$\int_a^b \int_c^d ...w_i(\underline{\zeta})...f(\underline{\zeta})\partial\underline{\zeta} = \Sigma_{i,j,...} W_i W_j ... f(\zeta_i, \zeta_j ...).$$

Table A.1 shows the values for the wieghts and the position of the ζ's for $i = 1, 3$.

Table A.1: Wieghts and Intervals for Gauss Quadrature. The position on the interval $[-1, +1]$ where the values are computed are shown along with wieghts, for $m = 1, 3$.

Number of Points	Position on $[-1, +1]$	Wieghts
1	0	2
2	$-1/\sqrt{3}$	1
	$+1/\sqrt{3}$	1
3	0	8/9
	$-\sqrt{3/5}$	5/9
	$+\sqrt{3/5}$	5/9

Appendix B

Fitting Noncoincidental Stochastic Data

The problem encountered when trying to relate the ERT conductance measurements to psychrometer moisture measurements was that the values were for different positions. As a result, there was no way to directly relate the measurements of conductance to the moisture as resulted from the psychrometer readings. To deduce this relationship, the calibration curve derived in Chapter 5 was used in the novel manner developed in this appendix.

As a general approach, it allows an uncalibrated set of measurements to be calibrated to noncoincidental data. It does this by interpolating one data set using kriging [15, 49] onto the discretized domain of the calibrated set using the generalized calibration function. The least-squares difference between the kriged values of the first data set and the values of the second data set are computed and then differentiated in terms of the parameters of the calibration curve. A set of independent equations results that hold simultaneously: one equation for each parameter. For the best fit in the least-squares sense, these relationships are set to zero; thus, the resultant system of equations can be solved for the calibration parameters.

B.1 The General Approach

Consider two sets of experimental measurements, $\{A_1\}$ and $\{\mathcal{V}_2\}$, of two stochastic distributions taken on a common system and at different points in a domain of all measurements.

The domain for the set of observations $\{A_1\}$ is $\mathcal{D}_1$, and for the set of observations $\{\mathcal{V}_2\}$ is $\mathcal{D}_2$, defined on:

$$\mathcal{D}_1 \epsilon [s_1^1, ..., s_i^1, ...s_n^1], \quad 1 \leq i \leq n \tag{B.1}$$

and

$$\mathcal{D}_2 \epsilon [s_1^2, ..., s_j^2, ...s_m^2], \quad 1 \leq j \leq m \tag{B.2}$$

Consider that there exists some calibration relationship between the readings $\{A_1\}$ and values $\{\mathcal{V}_1\}$ such that $\{A_1\}$ generate $\{\mathcal{V}_1\}$ when calibrated in a best-fit, least squares manner, to be derived, using $\{\mathcal{V}_2\}$. The general relationship defines the calibration curve in the following manner:

$$\{\mathcal{V}_1\} \equiv \{\aleph(\{A_1\}, \{\alpha_k\}_{1 \leq k \leq p})\}, \tag{B.3}$$

where $\aleph$ is the calibration curve and $\{\alpha_k\}$ are parameters of the calibration curve. The values in $\{A_1\}$ are interpolated to include values on the discrete domain $\mathcal{D}_2$ using the general method of kriging [15] and are determined to be:

$$\{\mathcal{V}_1(\mathcal{D}_2)\} = \{\Sigma_{i=1}^n w_{ij} \aleph(\{A_1\}, \{\alpha_k\})\} \tag{B.4}$$

where each point is

$$\mathcal{V}_1(s_j^2) = \Sigma_{i=1}^n w_{ij} \aleph(\{A_1\}, \{\alpha_k\}_{(k=1,p)})$$

and where w_{ij} is a wieghting function suitably selected for the kriging calculations [15]. The wieghting function is normalized, so the data is not biased, by the condition [49]

$$\Sigma_{i=1}^n w_{ij} = 1 \tag{B.5}$$

The square of the residual (σ_j^2) at data point j, not normalized, is

$$\sigma_j^2 \equiv [\mathcal{V}_1(s_j) - \mathcal{V}_2(s_j)]^2 \tag{B.6}$$

and hence the sum of the squares (σ^2) is

$$\sigma^2 \equiv \Sigma_{j=1}^m [\mathcal{V}_1(s_j) - \mathcal{V}_2(s_j)]^2 \tag{B.7}$$

$$= \Sigma_{j=1}^{m}[\Sigma_{i=1}^{n} w_{ij}\aleph_j(\{A_1(s_j)\},\{\alpha_k\}) - \mathcal{V}_2(s_j)]^2 \quad \text{(from B.4)} \tag{B.8}$$

This can be minimized with respect to the parameter α_k by differentiating as follows:

$$\partial(\sigma^2)/\partial\alpha_k = \Sigma_{j=1}^{m} 2[\Sigma_{i=1}^{n} w_{ij}\aleph(\{A_1(s_j)\},\{\alpha_k\}) - \mathcal{V}_2(s_j^2)][\Sigma_{i=1}^{n} w_{ij}\partial\aleph(\{A_1\},\{\alpha_k\})/\partial\alpha_k] \tag{B.9}$$

Equation B.9 can be expanded to p equations once the form of $\aleph$ has been determined. Where $\aleph$ is linear in the α_k's, they can be assembled and directly solved simultaneously by matrix inversion to determine the values of $\{\alpha_k\}$. (Any nonlinear function can be linearized using, for example, a Taylor expansion [8, 58].) The method also gives an estimation of the quality of the match as a least-squares measurement from Equation B.8.

B.2 The Electrical Resistivity Tomography Application

Tables B.1 and B.2 contain two sets of measurements from the URL. However, the physical positions of the measurements are different for the two data sets. Table B.1 contains admittance values (A_i) which have been shown to vary with the moisture content in a exponential fashion [81, 84], while the measurements in Table B.2 contain moisture measurements (M_i^{ps}) determined using calibrated instruments [94]. The admittance measurements need to be calibrated from the moisture readings to compare the measurements.

The standard gaussian distribution is selected as the wieghting function w_{ij} where:

$$w_{ij} = (1/\mu_j)exp[-(r_i - r_j)^2/k] \tag{B.10}$$

The value of k was selected to be 0.0005 m making the half-maximum of the wieghting function to occur at a radius of 0.019 m from the function's center. The wieghting function is further normalized to conform to Equation B.5 forcing the value of μ_j to be:

$$\mu_j = \Sigma_{i=1}^{n} exp[-(r_i - r_j)^2/k] \tag{B.11}$$

The calibration curve has the form [84]

$$M_i = \alpha + \beta \log A_i \tag{B.12}$$

where M_i is the moisture content, α and β are calibration constants, and A_i is the admittance.

From B.9, the minimized residuals are:

$$\partial(\sigma^2)/\partial\alpha = 2\Sigma_{j=1}^{m}[\Sigma_{i=1}^{n} exp-[(r_i - r_j)^2/.0005](\alpha + \beta \log A_i) - M_j^{ps}] \tag{B.13}$$

and

$$\partial(\sigma^2)/\partial\beta = 2\Sigma_{j=1}^{m}[\Sigma_{i=1}^{n}(1/\mu_j) exp-[(r_i - r_j)^2/.0005](\alpha + \beta \log A_i) - M_j^{ps}]$$

$$[\Sigma_{i=1}^{n} exp-[(r_i - r_j)^2/.0005] \log A_i] \tag{B.14}$$

Setting equations B.13 and B.14 to zero, and from B.11:

$$m\alpha +$$

$$\beta\Sigma_{j=1}^{m}[\Sigma_{i=1}^{n}(1/\mu_j) exp-[(r_i - r_j)^2/.0005] \log A_i]$$

$$= \Sigma_{j=1}^{m} M_j^{ps}$$

and

$$\alpha\Sigma_{j=1}^{m}[\Sigma_{i=1}^{n}(1/\mu_j) exp-[(r_i - r_j)^2/.0005] \log A_i] +$$

$$\beta\Sigma_{j=1}^{m}[\Sigma_{i=1}^{n}(1/\mu_j) exp-[(r_i - r_j)^2/.0005] \log^2 A_i]$$

$$= \Sigma_{j=1}^{m} M_j^{ps} \Sigma_{i=1}^{n} exp-[(r_i - r_j)^2/.0005] \log A_i$$

which can be rewritten into the form:

$$\mathbf{\Lambda}\underline{\beta} = \underline{\mathbf{y}} \tag{B.15}$$

where

$$\mathbf{\Lambda} = \begin{matrix} a_{11} & a_{12} \\ a_{21} & a_{22} \end{matrix}$$

$$\underline{\mathbf{y}} = \{y_1, y_2\}$$

$$\underline{\beta} = \{\alpha, \beta\}$$

$$a_{11} = m$$

$$a_{12} = \Sigma_{j=1}^{m}[\Sigma_{i=1}^{n}(1/\mu_j)exp{-}[(r_i - r_j)^2/.0005]logA_i]$$

$$a_{21} = \Sigma_{j=1}^{m}[\Sigma_{i=1}^{n}(1/\mu_j)exp{-}[(r_i - r_j)^2/.0005]logA_i]$$

$$= a_{12}$$

$$a_{22} = \Sigma_{j=1}^{m}[\Sigma_{i=1}^{n} w_{ij} \log A_i]^2$$

$$y_1 = \Sigma_{j=1}^{m} M_j^{ps}$$

and

$$y_2 = \Sigma_{j=1}^{m} M_j^{ps}[\Sigma_{i=1}^{n} exp{-}[(r_i - r_j)^2/.0005] \log A_i]$$

Equation B.15 was solved for the parameters α and β to determine the calibration curve for moisture measurements using admittance readings.

B.3 Results and Discussion

Figure 5.12 plots the data fitted using the method decsribed. Figure B.1 plots the kridged values using the calibration curve. The processing was done using the admittance data as the support because of the relatively high density of elements in that set. The moisture data for the position 0.6 m was not used in the fit because the distribution was highly anomalous and not adequately sampled for admittance [94]. The values determined (fitted for admittance $\times 10^4$) were:

$$a_{11} = 5.000$$

$$a_{12} = -44.399$$

$$a_{22} = 402.405$$

$$y_1 = 102.100$$

$$y_2 = -903.932$$

$$\alpha = 23.362$$

$$\beta = 0.3314$$

The results include a statistical estimation of the error of the calibration curve for M using the vector sum of the errors of the measurements of the known moisture contents [8]:

$$\delta M = (\partial M/\partial(A)) \times \delta A$$

$$= \Sigma(\beta/A_i) \times (\delta A_i) \tag{B.16}$$

Where the moisture is known from a direct measurement, the difference between the computed and measured results are used as the indication of the error. A sum is taken over all results from the known moisture values and divided by the number of points in the computation to give a general measure of the quality of the fit (σ^2). The value determined was 0.558.

This is true for the interpolated moisture content as is shown in Table B.3 and in the value of σ. Individual computations could be improved further by minimizing the standard deviation by varying the wieghting function using the the parameter k.

The method effectively combines interpolation to common values using kriging, with a linear-regression to fit the results. This two-step processes is reduced to the single step of assembling and solving a set of linear equations when the calibration function is linear in the calibration parameters. It results in a good fit of separate data sets based on the low value of the sum of the differences squared.

Table B.1: Data set of admittance measurements

Position (m)	Admittance (10^{-4} S)
-0.6110	8.844
-0.5667	1.318
-0.5667	0.080
-0.5223	0.006
-0.4401	1.152
-0.3844	0.158
-0.3598	1.061
-0.2676	6.795
-0.2392	1.913
-0.1903	4.479
-0.1415	7.345
-0.1131	7.382
0.1131	4.875
0.1415	4.150
0.1903	2.572
0.2392	1.758
0.2676	1.671
0.3598	0.776
0.3884	0.479
0.5223	0.137
0.5667	0.260
0.6110	1.448

Table B.2: Data set of moisture measurements

Position (m)	Moisture (%)
-0.6	21.4
-0.4	20.1
-0.2	20.8
0.2	20.0
0.4	19.8
0.6	25.1

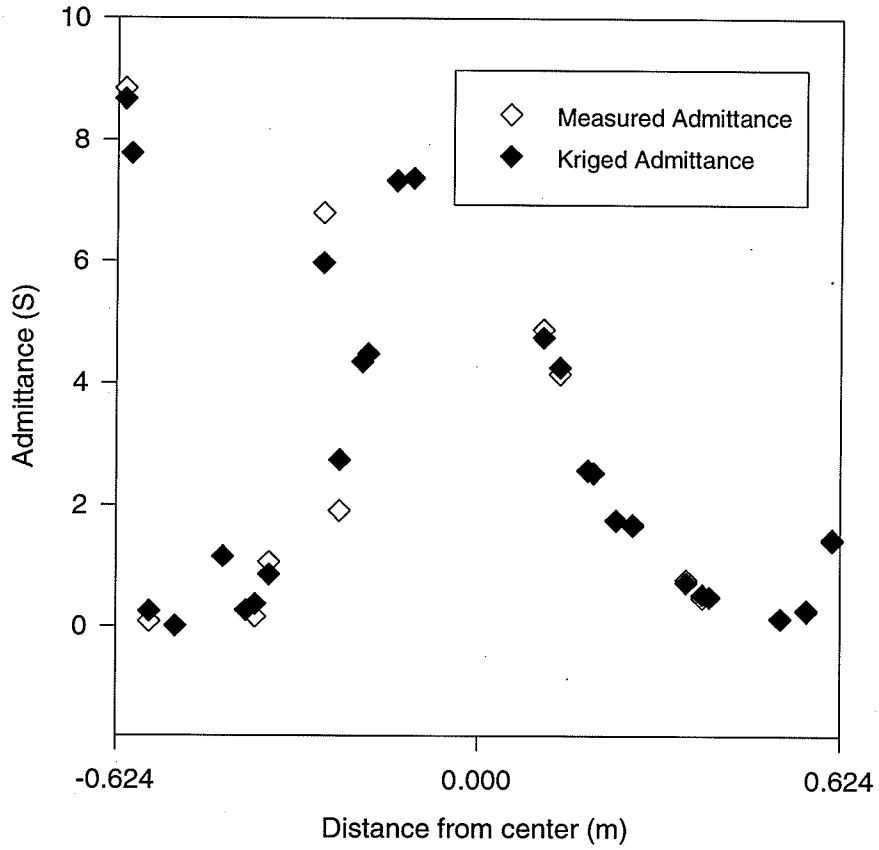

Figure B.1: Plot of calibrated data with interpolated points. This is data with kriged values of admittance where moisture was measured.

Table B.3: Results from the calibrated fit along the calibration profile. The estimate of error is computed from the difference between the admittance and interpolated admittance where the admittance was measured: according to Equation B.16. Where moisture readings are available, the variance is the difference between the moisture and the interpolated moisture.

Position (m)	Admittance Measured (10^{-4} S)	Admittance Computed (10^{-4} S)	Moisture Measured (%)	Moisture Computed (%)	Estimate of Error
-0.611	8.844	8.674	——	21.026	0.000
-0.600	——	7.777	21.400	21.000	0.160
-0.567	0.080	0.245	——	19.844	0.050
-0.522	0.006	0.007	——	18.685	0.004
-0.440	1.152	1.150	——	20.356	0.000
-0.400	——	0.267	20.100	19.802	0.089
-0.384	0.158	0.367	——	19.978	0.036
-0.360	1.061	0.854	——	20.258	0.006
-0.268	6.795	5.984	——	20.903	0.002
-0.239	1.913	2.736	——	20.644	0.010
-0.200	——	4.347	20.800	20.727	0.005
-0.190	4.479	4.482	——	20.807	0.000
-0.142	7.345	7.331	——	20.970	0.000
-0.113	7.382	7.376	——	20.972	0.000
0.113	4.875	4.755	——	20.826	0.000
0.142	4.150	4.258	——	20.790	0.000
0.190	2.572	2.579	——	20.624	0.000
0.200	——	2.531	20.000	20.548	0.300
0.239	1.758	1.749	——	20.496	0.000
0.268	1.671	1.685	——	20.484	0.000
0.360	0.776	0.728	——	20.205	0.000
0.388	0.479	0.527	——	20.098	0.000
0.400	——	0.494	19.800	20.000	0.004
0.522	0.137	0.139	——	19.656	0.000
0.567	0.260	0.280	——	19.888	0.000
0.611	1.448	1.425	——	20.426	0.000

Appendix C

Excitation Patterns

The excitation patterns used for synthetic and experimental cases are shown in Table C.1. Each is identified by figure labels and shows the degrees of freedom, number of electrodes, number of excitation pairs, the initial image and the grid used. The circular grid is the mesh shown in Figure 5.7. In this case, the elements are numbered in a counter-clockwise manner as is each node for each element: the centre node is the nineth. For the regular, square, two-dimensional grid, the nodes are numbered left-to-right and back-to-front. For the three-dimensional mesh, when the electrodes are evenly distribute on the surface, the electrode numbering scheme does not correspond to the nodes, but to the electrode array. The three-dimensional meshes were all regular grids label as in the two-dimensional grid from top-to-bottom for the third dimension. The degrees of freedom for these cases is the number of unknowns when solving for the field equations. This will correspond directly to the number of degrees of freedom in the model for the two-dimensional case. For the three-dimensional case, it will correspond to the tabulated degrees of freedom - ($p \times m + (n - 1) \times p + (m - 1) \times (n - 1)$) where the grid is $m \times n$ nodes, by p nodes high.

Table C.1: Excitations used for Figures.

Figure	Grid	Degrees of freedom	Number of excitations	Number of electrodes
Figures 2.2,3.5, 4.1,4.21,4.1	11×11	121	37	20
Excitations 01 121,03 119,05 117,07 115,09 113,11 111,33 89,55 67,77 45, 99 23,01 33,03 55,05 77, 07 99,09 121,11 119,33 117,55 115,77 113,99 111,121 89,119 67, 117 45,115 23,113 01, 09 33,99 119,113 89,23 03,07 55,77 117,115 67,45 05,05 77,55 115, 117 45,67 07				
Electrodes 1,3,5,7,9,11,33,55,77,99,23,45,67,89,111,113,115,117,119,121				
Figures 3.3,3.4, 4.2,4.4,4.6,4.8, 4.11,4.13	17×17	289	18	16
Excitations 01 289,05 285,09 281,13 277,17 273,85 205,153 137,221 69, 05 217,09 281,13 285, 17 289,69 85,137 153,205 221,273 289,01 17,01 273				
Electrodes 1,5,9,13,17,85,153,221,289,285,281,217,273,205,137,69				
Figure 4.17	$9 \times 12 \times 5$	540	38	20
Excitations 1 130,4 127,7 124,10 121,31 100,34 97,37 94,40 91,31 61,34 64, 37 67,40 70,64 94, 67 97,70 100,37 40,67 70,97 100,61 91,34 37,64 67,94 97, 31 34,61 64,91 94,1 10, 31 40,61 70,91 100,121 130,1 121,4 124, 7 127,10 130,31 91,34 94,37 97,40 100				
Electrodes 1,4,7,10,31,34,37,40,61,64,67,70,91,94,97,100,121,124,127,130				
Figures 4.18,4.15	9×9×5	405	25	148
Excitations 71 184,137 120,81 176,145 112,89 168,153 104,97 160,161 96,105 152, 105 152,169 88, 113 144,177 80,122 135,186 71,123 134,187 70,124 133,188 67,125 132, 189 68,126 131, 190 67,127 130,191 66				
Electrodes 1,2,3,4,5,6,7,8,9,10,11,12,13,14,15,16,17,18,19,20,21,22,23,24,25,26,27,28, 29,30,31,32, 33,34,35,36,37,38,39,40,41,42,43,44,45,46,47,48,49,50,51,52,53,54,55,56,57, 58,59,60, 61,62,63,64,65,73,81,89,97,105,113,121,129,137,145,153,161,169,177,185,193, 201,209, 217,225,233,241,249,72,80,88,96,104,112,120,128,136,144,152,160,168,176,184,192, 200, 208,216,224,232,240,248,256,66,67,68,69,70,71,130,131,132,133,134,135,194,195,196, 197,198,199,122,123,124,125,126,127,186,187,188,189,190,191,250,251,252,253,254,255				

Table C.2: Excitations used for Figures (Continued from previous page).

Figure	Grid	Degrees of freedom	Number of excitations	Number of electrodes
Figures 4.9,4.10	51×51	2601	35	200
Excitations				
{1 2559,5 2554,...,49 2553},{208 2497,416 2289,...,2246 155}, 3 2552,7 2556,11 2560, 15 2564,19 2568,23 2572,27 2576,31 2580,35 2584,39 2588				
Electrodes				
1,2,3,4,5,6,7,8,9,10,11,12,13,14,15,16,17,18,19,20,21,22,23,24,25,26,27,28, 29,30,31,32,33,34, 35,36,37,38,39,40,41,42,43,44,45,46,47,48,49,50,51,{52,104,...,2550}, {103,155,...,2601},{2551,2552,...,2600}				
Figures 5.5,5.10, 6.4,7.1	Figure 5.7	289	25	32
Excitations				
01 29,33 05,09 45,49 13,17 53,57 21,25 61,09 37,41 13,01 05,09 13, 17 21,25 29, 33 37,41 45,49 33,57 61,01 13,17 29,33 45,49 61,09 21,25 37,41 53, 57 05				
Electrodes				
1,3,5,7,9,11,13,15,17,19,21,23,25,27,29,31,33,35,37,39,41,43,45,47,49,51, 53,55,57,59,61,63				
Figures 6.5,6.13, 6.20,6.21,6.23,4.20	4 × 5 × 4	780	39	20
Excitations				
01 20,02 19,03 18,04 17,05 16,06 15,07 14,08 13,05 09,06 10,07 11, 08 12,10 14,11 15, 12 16,07 08,11 12,15 16,09 13,06 07,10 11,14 15,01 27,05 06,09 10, 13 14,01 04, 05 08,09 12,13 16,17 20,01 17,02 18,03 19,04 20,05 13,06 14,07 15, 08 16				
Electrodes				
1,2,3,4,5,6,7,8,9,10,11,12,13,14,15,16,17,18,19,20				
Figures 6.17,6.18	20 × 10 × 4	800	49	50
Excitations				
1 3,11 13,21 23,31 33,41 43,4 6,14 16,24 26,34 36,44 46,7 9,17 19, 27 29,37 39,47 49,42 44, 32 34,22 24,12 14,2 4,5 7,15 17,25 27,35 37,45 47, 48 50,38 40,28 30,18 28,1 31,11 41,2 32, 12 42,3 33,13 43,4 34,14 44,5 35,15 45,6 36,16 46,7 37, 17 47,8 48,18 48,9 39,19 49,10 40,20 50				
Electrodes				
1,2,3,4,5,6,7,8,9,10,11,12,13,14,15,16,17,18,19,20,21,22,23,24,25,26,27,28, 29,30,31,32,33, 34,35,36,37,38,39,40,41,42,43,44,45,46,47,48,49,50				
Figure 6.19	18 × 18 × 3	972	32	36
Excitations				
1 5,2 6,7 11,8 12,13 17,14 18,19 23,20 24,25 29,26 30,31 35, 32 36,1 25,7 31, 2 26,8 32,3 27,9 33,4 28,10 34,5 29,11 35,6 30,12 36,8 22,15 29, 11 21,16 26, 3 13,4 18,19 33,34 24				
Electrodes				
1,2,3,4,5,6,7,8,9,10,11,12,13,14,15,16,17,18,19,20,21,22,23,24,25,26,27,28, 29,30,31,32,33,34,35,36				

Appendix D

Borehole Logs

The coring logs for the boreholes shown in Figure 6.14 are included in Appendix D. These are taken from [92].

BOREHOLE CT-1

Location: WMA'C' Trench 20 centreline
Borehole Type: CME-75, Continuous Core
Surface Elevation: 164.75
Top of Pipe: 165.58

UTM Grid Coord E: 121+61.37W 313.835.1
UTM Grid Coord N: 426.24S 5,101,567.7
Date: 1995/08/14
Logged By: SW

N-Counts	Core Recovery	Contact Depth (m)	Description	Graphic Log	Sample Number, Type and Interval (m)	Monitors Seals/Backfill	Field Counts (cpm)	Remarks
7			SAND FILL (10YR 6/2) Clean, loose, moderately sorted, massive, light brownish grey fine sand fill. Pit run cobbles up to 4 cm diameter. Augers grinding on cobbles at 1 m.		1 SS 0-0.37		120	
					2 SS 0.76-1.13		120	
8		1.52			3 SS 1.52-1.71		120	
7			WASTE Waste composed of a cap from a scintillation vial, plastic, chunks of translucent rubbery material, styrofoam balls, fibery material in green dye and flakes of metal. The matrix is composed of sand fill.		4 SS 2.29-2.44		1000	A 10 slot PVC screen was placed below the watertable from 8.29 to 9.81 m. A 0.6 m bentonite seal was placed in the borehole from 5.79 to 6.40 m. Clean sand fill and silica sand were placed around the well screen and extend up to and above the bentonite seal. Fill was added to the borehole as the augers were pulled up to the base of the trench, to prevent waste from migrating downward below the trench.
6		3.17			5 SS 3.05-3.17		2200	
8			SAND FILL (10YR 6/2) Clean, loose, moderately sorted, massive to very weakly laminated, light brownish grey fine sand fill. Lenses of iron staining 4.63 to 4.66 m.		6 SS 3.81-4.21		150	
6					7 SS 4.57-5.00		150	
		5.00						
15			VERY FINE SAND (10YR 6/4) Silty, compact, poorly sorted, massive, light yellowish brown very fine sand.		8 SS 5.33-5.61		250	
		5.61			9 SS 5.61-5.94		150	
24			FINE SAND (10YR 6/2 to 10YR 6/1) Clean, compact to very dense, well sorted, well laminated, fine sand. Unit is speckled with mica and garnets.		10 SS 6.10-6.61		150	
27					11 SS 6.86-7.47		150	
17					12 SS 7.62-8.14		150	
60					13 SS 8.38-8.81		150	
					14 CC 9.14-9.91		150	
					15 CC 9.91-10.67			

BOREHOLE CT-1

Location: WMA'C' Trench 20 centreline
Borehole Type: CME-75, Continuous Core
Surface Elevation: 164.75
Top of Pipe: 165.58

UTM Grid Coord E: 121+61.37W
UTM Grid Coord N: 426.24S
Date: 1995/08/14
Logged By: SW

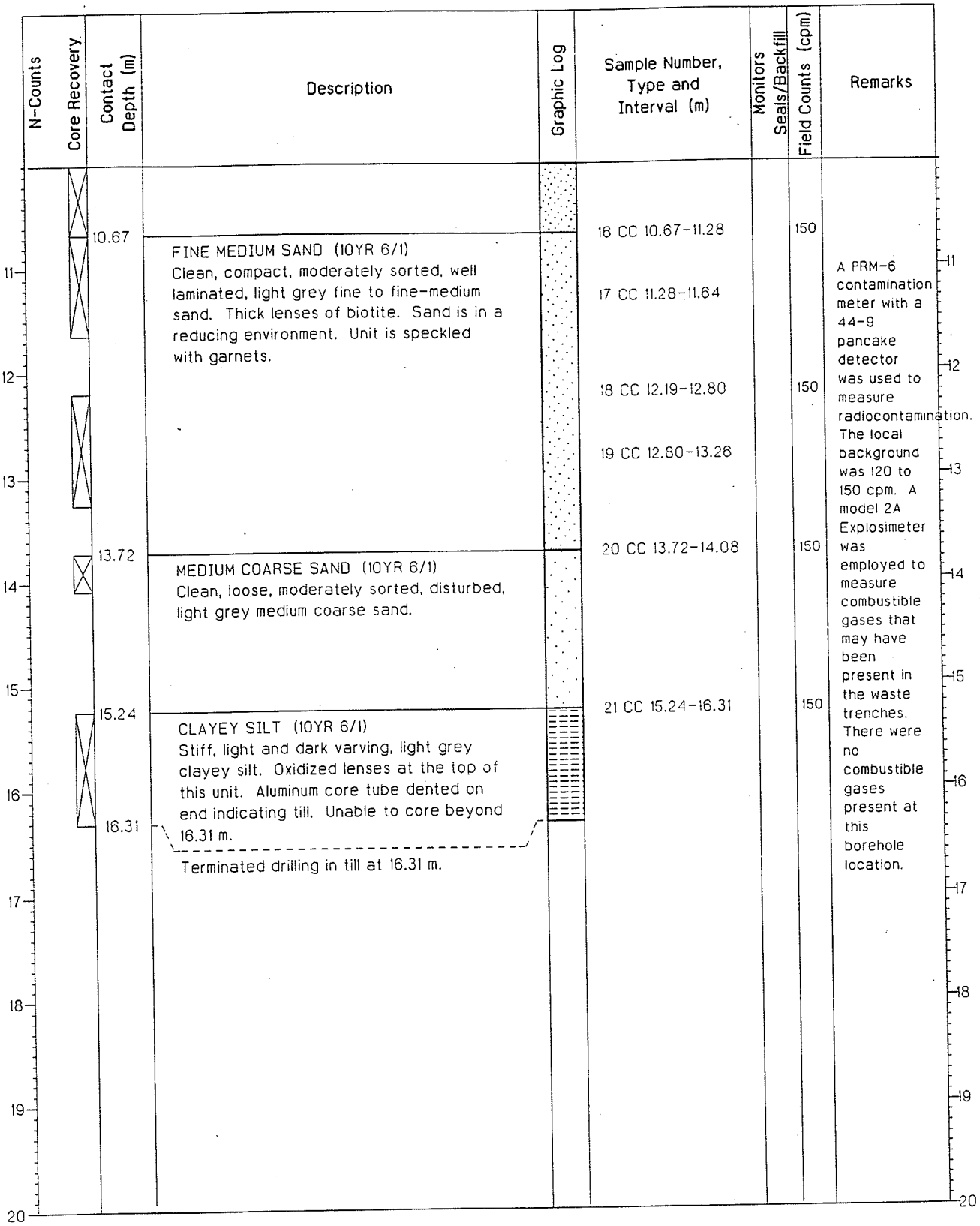

BOREHOLE CT-2

Location: WMA'C' Trench 19 centreline
Borehole Type: CME-75, Continuous Core
Surface Elevation: 164.27
Top of Pipe: 165.24

UTM Grid Coord E: 123+38.81W 513,781.7
UTM Grid Coord N: 398.74S 5,101,557.6
Date: 1995/08/18
Logged By: SW

N-Counts	Core Recovery	Contact Depth (m)	Description	Graphic Log	Sample Number, Type and Interval (m)	Monitors Seals/Backfill	Field Counts (cpm)	Remarks
5			SAND FILL (10YR 6/2 to 10YR 6/4) Clean, loose, moderately sorted, massive, light brownish grey to light yellowish brown fine sand fill. Pit run cobbles up to 3 cm diameter.		1 SS 0-0.12		150	A 10 slot PVC screen was placed below the watertable from 8.02 to 9.54 m. A 0.6 m bentonite seal was placed in the borehole from 6.10 to 6.71 m. Clean sand fill was placed around the well screen and extend up to and above the bentonite seal. Fill was added to the borehole as the augers were pulled up to the base of the trench, to prevent waste from migrating downward below the trench.
6					2 SS 0.76-1.07		300	
10		1.65	WASTE Waste composed of asphalt, plastic, wood, mop head, rubber gloves and wire. The matrix is composed of sand fill.		3 SS 1.52-1.65 4 SS 1.65-1.95		250	
25					5 SS 2.29-2.56		200	
7		3.11	SAND FILL (10YR 6/2) Clean, loose, moderately sorted, massive to very weakly laminated, light brownish grey fine sand fill. Lenses of iron staining at top of unit.		6 SS 3.05-3.11		150	
7					7 SS 3.11-3.41		150	
8					8 SS 3.81-4.24			
7					9 SS 4.57-5.00		150	
17		5.33			10 SS 5.33-5.49		150	
		5.49	VERY FINE SAND (10YR 6/4) Silty, moist, compact, poorly sorted, massive, light yellowish brown very fine sand.		11 SS 5.49-5.85			
25			FINE SAND (10YR 6/2 to 10YR 6/1) Clean, compact, well sorted, well laminated, fine sand. Unit is speckled with mica and garnets. Silt laminae approx. 5 mm thick at 5.67, 6.37 and 7.89 m. Lenses of iron stain at 6.28 and 7.68 m.		12 SS 6.10-6.55		150	
20					13 SS 6.86-7.35		150	
15			FINE SAND continued		14 SS 7.62-8.08		300	A PRM-6 contamination meter with a 44-9 pancake detector was used to measure radiocontamination. The local background was 150 cpm. A model 2A Explosimeter was employed to measure combustible gases that
28		8.38	VERY FINE SAND (10YR 6/4) Clean, loose to compact, moderately sorted, weakly laminated, light yellowish brown very fine sand. Unit is speckled with mica and garnets.		15 SS 8.38-8.84		250	
10					16 SS 9.14-9.63		150	
		9.63	Terminated drilling in sand at 9.63 m.					

BOREHOLE CT-3

Location: WMA'C' Trench 19 centreline
Borehole Type: CME-75, Continuous Core
Surface Elevation: 164.21
Top of Pipe: 165.31

UTM Grid Coord E: 123+39.51W 313.783.3
UTM Grid Coord N: 414.44S 5 10: 53.1
Date: 1995/08/16
Logged By: SW

N-Counts	Core Recovery	Contact Depth (m)	Description	Graphic Log	Sample Number, Type and Interval (m)	Monitors Seals/Backfill	Field Counts (cpm)	Remarks
4			SAND FILL (10YR 6/2 to 10YR 6/4) Clean, loose, moderately sorted, massive, light yellowish brown fine sand fill. Pit run cobbles up to 4 cm diameter. A stainless steel bolt was found in the core. It measured 11000 cpm. The soil however, was background in terms of radiocontamination.		1 SS 0-0.27		150	A 10 slot PVC screen was placed below the watertable from 7.99 to 9.51 m. A 0.6 m bentonite seal was placed in the borehole from 7.01 to 7.62 m. Clean sand fill was placed around the well screen and extend up to and above the bentonite seal. Fill was added to the borehole as the augers were pulled up to the base of the trench, to prevent waste from migrating downward below the trench.
11					2 SS 0.76-0.88		1000	
6					3 SS 1.52-1.80		150	
11		2.29	WASTE Waste composed of plastic, wood, paper and rubber gloves. The waste is wet. The matrix is composed of sand fill. There appeared to be dust coming out of the augers after driving the split spoon on the sixth sample.		4 SS 2.29-2.47		150	
64+					5 SS 3.05-3.17		150	
8		3.90	SAND FILL No sample was recovered from 4.57 to 5.18 m. However, the split spoon penetrated easily so it is inferred that this region is sand fill.		6 SS 3.81-3.90		250	
7								
20		5.33	FINE SAND (10YR 6/2) Clean, compact, well sorted, weakly to well laminated with depth light brownish grey fine sand. Unit is speckled with mica and garnets. Silt laminae approx. 5 mm thick at 5.49, 5.61, 6.21, 7.01, 7.07 to 7.13, 7.68 and 7.88 m. Lenses of iron staining at the top of this unit and just below the water table. FINE SAND continued		7 SS 5.33-5.70		150	
26					8 SS 6.10-6.43		150	
21					9 SS 6.86-7.25		150	
16					10 SS 7.62-8.02		150	A PRM-6 contamination meter with a 44-9 pancake detector was used to measure radiocontamination. The local background was 150 cpm. A model 2A Explosimeter was employed to measure combustible gases that
17		8.38	VERY FINE SAND (10YR 6/4) Clean, compact, moderately sorted, massive to weakly laminated, light yellowish brown very fine sand. Unit is speckled with mica and garnets.		11 SS 8.38-8.69		150	
15					12 SS 9.14-9.51		200	
		9.51	Terminated drilling in sand at 9.51 m.					

BOREHOLE CT-4

Location: WMA'C' Trench 21
Borehole Type: CME-75, Continuous Core
Surface Elevation: 164.33
Top of Pipe: 165.06

UTM Grid Coord E: 123+19.66W 313,794.5
UTM Grid Coord N: 464.54S 5,101,541.1
Date: 1995/08/22
Logged By: SW

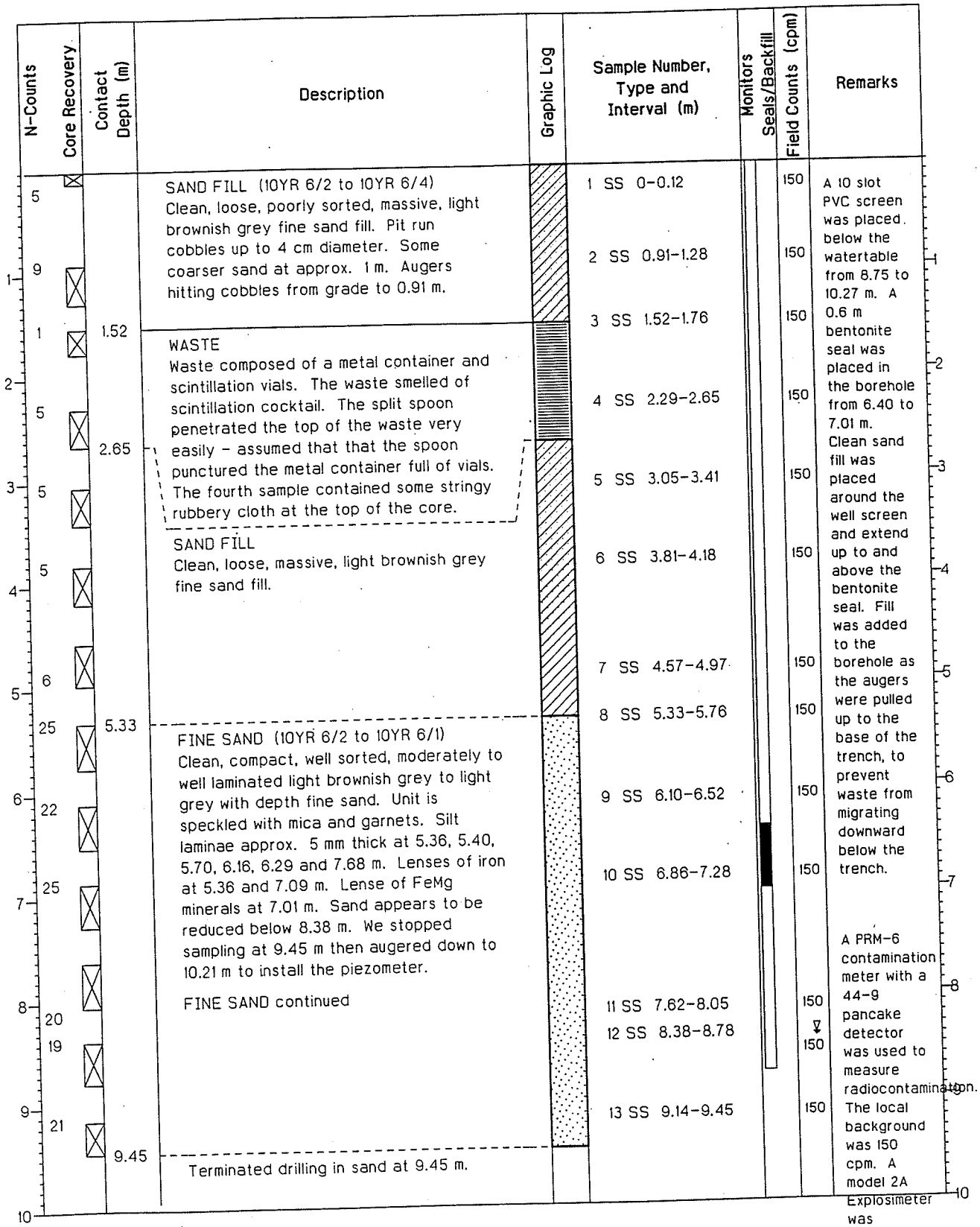

BOREHOLE CT-5

Location: WMA 'C' Trench 21
Borehole Type: CME-75, Continuous Core
Surface Elevation: 164.22
Top of Pipe: 165.5

UTM Grid Coord E: 123+47.66W 313784.7
UTM Grid Coord N: 447.74S 5101542.7
Date: 1995/08/23
Logged By: SW